Alma Mater Studiorum · Università di Bologna

Scuola di Scienze
Corso di Laurea Magistrale in Fisica del Sistema Terra

On the wind driven circulation of the Mediterranean Sea

Relatore:
Prof.ssa Nadia Pinardi

Presentata da:
Jacopo Alessandri

Correlatore:
Dott. Francesco Trotta
Dott.ssa Simona Masina

Sessione I
Anno Accademico 2016/2017

Homme libre, toujours tu chériras la mer!
La mer est ton miroir; tu contemples ton âme
Dans le déroulement infini de sa lame,
Et ton esprit n'est pas un gouffre moins amer.

Baudelaire

Abstract

The Mediterranean Sea is a semi-enclosed, anti-estuarine basin between north-Africa, Europe and the Middle-East. The Mediterranean circulation appears to be the result of three principal forcing factors: the inflow/outflow at Gibraltar strait, the wind stress applied on the ocean surface and the buoyancy fluxes. In this thesis, the efforts are mainly focused on studying the role of the wind in the ocean circulation. The introduction includes a first section where classical wind-driven circulation solutions are presented, then there is a brief introduction to ocean numerical modelling and a section on the Mediterranean circulation and variability.
Generally the large scale basin circulation is characterized by cyclonic gyres in the northern regions, and by an anticyclonic gyres and eddy-dominated flow fields in its southern parts, with the exception of the Tyrrhenian and the northern Ionian Sea (Pinardi et al., 2015). The seasonal variability is strongly related to the amplitude of the seasonal cycle in the atmospheric forcing. The surface atmospheric flow field is characterised by regional wind regimes that are strongly dependent upon the interaction of Westerlies with the local orography during winter, and the land-sea temperature contrast during Summer. The interannual variability of the ocean circulation plays an important role, because it can be related to long-term, large-scale atmospheric circulation changes.
Over the Europe and the Mediterranean, these changes were produced by decadal scale changes related to the *North Atlantic Oscillation* (NAO). Two different circulation patterns can be recognized in the periods ranging from 1987 to 1996 (period A) and from 1997 to 2006 (period B). The largest changes between the two periods occur in the EMED where a current reversal takes place in the northern ionian sea and large differences in gyre location and current amplitude are visible in the Cretan Passage and the Levantine basin. In the Ionian sea the Atlantic Ionian Stream (AIS) shows a large northward meander in period A, giving rise to an overall anticyclonic circulation in the northern part of the basin. On the other hand during period B, the circulation in the northern Ionian is cyclonic and the AIS cut across the basin, remaining at the latitude of 36° N after the Malta escarpment. This decadal change is called the *Northern Ionian Reversal* phenomenon (NIR), and represents the most important contribution to the decadal variability of the Mediterranean circulation for the reanalysis period described in Pinardi et al. (2015). The NIR phenomenon is also documented by observational studies with surface drifters (Poulain et al., 2012) and satellite altimetry (Borzelli et al., 2009). Several numerical modelling studies have documented a reversal from cyclonic to anticyclonic around the 1987 (Korres et al., 2000; Demirov and Pinardi, 2002), and connected it to changes in wind stress curl sign. The central part of this thesis is dedicated to the analysis of the role of the wind stress for the ocean circulation. The objective is to evaluate how and in which proportion the wind stress can influence currents and gyres, and the associate variability, with a special treatment for the NIR phenomenon that seems to be strictly related with changes in the atmospheric forcing.
The study is carried out using numerical model simulations. The model used is the *Nucleus for European Modelling of the Ocean* (NEMO), a state-of-the-art primitive equation model implemented in the Structured and Unstructured grid Relocatable

ocean platform for Forecasting (SURF; Trotta et al., 2015). Perpetual year (PY) experiments at horizontal resolution of $\frac{1}{8}^\circ$ are carried out using a monthly climatological dataset as forcing input. For the wind stress, the resolution of the input data seems to be a very important parameter as the coarse resolution forcing does not resolve the land-sea contrast adequately. The $\frac{1}{8}^\circ$ ECMWF analysis wind field for the period 2010-2015 is chosen as a surface boundary condition for PY experiments. The monthly climatology of the wind stress is built and used as the forcing field for the control experiment. It reproduces well all the sub-basin gyres and currents (Alboran gyre, Rhodes Gyre, Atlantic Ionian Stream...) and shows an overall cyclonic circulation in the northern Ionian sea. An *Empirical Orthogonal Function* (EOF) analysis is achieved on the wind stress monthly climatology and an idealized wind is built using some EOF components and is used as surface forcing. Sensitivity experiments are performed on the physics of the model and on the wind forcing, evaluating the relation between the wind stress and the Mediterranean upper circulation. The last chapter is dedicated to a diagnostic study of the NIR phenomenon carried out using an useful index, hereafter called the NIR index. The NIR index uses the difference of the SSH at two points, at $18^\circ E$ of longitude and 38° and 35° N of latitude to evaluate the prevailing circulation in the northern Ionian Sea. Positive values of the index are connected to anticyclonic circulation, while negative values are related to cyclonic circulation. SSH field from Reanalysis, model output and SLA Satellite observations are analysed and compared. Studies agree in setting the time of the surface reversal to 1997 and this is confirmed by the change of the NIR index sign, both in reanalysis and observations.

Abstract
Italian version

Il Mar Mediterraneo è un bacino semichiuso, anti-estuarino compreso tra l'Africa, l'Europa e il Medio Oriente. La circolazione del Mediterraneo è il risultato di tre principali fattori forzanti: l'afflusso e il deflusso di acqua allo stretto di Gibilterra, lo stress del vento applicato sulla superficie del mare e i flussi di galleggiamento. In questa tesi gli sforzi si concentrano sullo studio del ruolo del vento nella circolazione del Mediterraneo. L'introduzione include una breve sezione dove le soluzioni classiche della circolazione guidata dal vento sono presentate, quindi si passa ad una breve introduzione ai modelli numerici di oceano e ad una sezione sulla circolazione del Mediterraneo e la sua variabilità. Generalmente la circolazione di larga scala è caratterizzata da giri ciclonici nelle regioni settentrionali, e da giri anticiclonici e flussi dominati da vortici nelle regioni meridionali, con l'eccezione del Mar Tirreno a dello Ionio settentrionale (Pinardi et al., 2015). La variabilità stagionale è fortemente legata all'ampiezza stagionale del forzante atmosferico. I flussi atmosferici superficiali sono caratterizzati da regimi di vento regionali che, in Inverno hanno una forte dipendenza dall'interazione tra i Westerlies e l'orografia locale mentre in Estate dipendono dal contrasto di temperatura tra mare e terra solida. La variabilità interannuale della circolazione ha un ruolo importante, perché può essere collegata a variazioni di lungo termine e su larga scala della circolazione atmosferica.
Sopra l'Europa e il Mediterraneo, queste variazioni sono prodotte da cambiamenti decadali collegati alla *Oscillazione Nord Atlantica* (NAO). Due differenti pattern di circolazione possono distinguersi nei periodi dal 1987 al 1996 (periodo A) e dal 1997 al 2006 (periodo B). I maggiori cambiamenti tra i due periodi avvengono nel Mediterraneo orientale (EMED), dove un' inversione di corrente ha luogo nello Ionio settentrionale e grosse differenze nella posizione dei giri e nell' intensità della corrente si possono osservare nel passaggio di Creta e nel bacino del Levante. Nel Mar Ionio, l' Atlantic Ionian Stream (AIS) mostra ampi meandri che si estendono verso nord durante il periodo A, dando vita ad una circolazione complessivamente anticiclonica nella parte settentrionale del bacino. Durante il periodo B, la circolazione nello Ionio settentrionale é ciclonica e l'AIS attraversa il bacino, rimanendo ad una latitudine di 36° N dopo la scarpata di Malta. Questa variazione decadale è chiamata *Northern Ionian Reversal* (NIR; Pinardi et al., 2015), e rappresenta il più importante contributo alla variabilità decadale della circolazione per il periodo della rianalisi. Il fenomeno del NIR è documentato anche da studi osservativi con drifters superficiali (Poulain et al., 2012) e altimetria satellitare (Borzelli et al., 2009). Diversi studi con modelli numerici hanno documentato un' inversione della circolazione da ciclonica ad anticiclonica attorno al 1987 (Korres et al., 2000; Demirov e Pinardi, 2002), e lo hanno connesso a variazioni nel segno della vorticità dello stress del vento. La parte centrale della tesi è dedicata all'analisi del ruolo dello stress del vento nella circolazione del Mediterraneo. L'obiettivo è di valutare come e in che proporzioni lo stress del vento possa influenzare le correnti e i giri, e la variabilità associata a questi, con una maggiore attenzione per il fenomeno del NIR che sembra essere strettamente collegato a variazioni nel forzante atmosferico. Lo studio è effettuato usando un modello di simulazione numerica. Il modello usato è il *Nucleus for European Modelling of the Ocean* (NEMO), un modello che integra

le equazioni primitive per l'oceano, implementato nello *Structured and Unstructured grid Relocatable ocean platform for Forecasting* (SURF; Trotta et al., 2015). Si procede con esperimenti a forzante perpetuo (PY) alla risoluzione orizzontale di $\frac{1}{8}^\circ$ usando forzanti climatologici mensili. Per quanto riguarda lo stress del vento, la risoluzione dei dati in ingresso sembra essere un parametro molto importante dato che i forzanti a bassa risoluzione non risolvono adeguatamente i contrasti tra terra solida e mare. Come forzante superficiale per i PY sono scelte le analisi del campo di vento dell' ECMWF con risoluzione di $\frac{1}{8}^\circ$ per il periodo 2010-2015. Dai campi di vento si costruisce una climatologia mensile dello stress del vento, che viene quindi usato come forzante nell'esperimento di controllo. L'esperimento riproduce correttamente i giri e le correnti che caratterizzano la circolazione alla grande scala del Mediterraneo (giro di Alboran, giro di Rodi, AIS...) e mostra una circolazione complessivamente ciclonica nello Ionio settentrionale. La climatologia mensile dello stress del vento è analizzata utilizzando le *Empirical Orthogonal Function* (EOF), dalle quali uno stress idealizzato ricostruito utilizzando alcune delle componenti delle EOF e utilizzato come forzante superficiale. La fisica del modello è analizzata attraverso esperimenti di sensitività, e ulteriori simulazioni sono finalizzate alla valutazione della relazione tra lo stress del vento e la circolazione superficiale del Mediterraneo. L'ultimo capitolo è dedicato ad uno studio diagnostico del NIR, effettuato utilizzando un indice (NIR index). Il NIR index usa la differenza di SSH in due punti, a $18^\circ\, E$ di longitudine e 38° e 35° N di latitudine per valutare la circolazione prevalente nello Ionio settentrionale. Valori positivi di questo indice sono connessi ad una circolazione anticiclonica, mentre valori negativi indicano una circolazione di tipo ciclonico. Si analizzano e si confrontano gli indici calcolati dalla SLA delle osservazioni satellitari e dai campi di SSH delle rianalisi e dei risultati del modello. Gli studi concordano in porre il periodo dell'inversione al 1997, anno confermato anche dal cambio di segno del NIR index sia nelle rianalisi che nelle osservazioni.

Contents

Chapter 1

Introduction

1.1 The ocean wind driven circulation

It is well known from observations that the pattern of the oceanic circulation reflects very well the pattern of the winds, *i.e.*, general westward flow in equatorial regions under the influence of the Trade winds and predominantly eastward flow in mid-latitudes, the region of the westerly winds. Although differential heating of the sea surface can produce motion by buoyant forces, even the wind stress only can produce a net (vertically integrated) horizontal transport.

1.1.1 The homogeneous model

In this section some insight of the wind driven circulation are discussed using a simple model of the ocean circulation which attribute the motion of the ocean entirely to the action of the wind, in particular to the stress exerted by the wind on the sea surface. The models used to describe the ocean wind driven circulation are homogeneous in density and then neglect any dynamical effect due to the ocean stratification. For simplicity the complex topography of the ocean floor and the complexity of the shape of the perimeter of the basins are completely ignored. Homogeneous model can successfully catch the essential physics of the oceanic circulation. They can't describe adequately the vertical structure of the ocean, but are successful in reproducing the major features of the large scale horizontal circulation, such the westward intensification. The essential aspects of the model are depicted in figure 1.1. There are three fluid layers: a thin surface Ekman layer, the interior layer of depth D and a thin bottom frictional Ekman layer over a sloping bottom.

The Ekman transport due to the wind stress in the Ekman surface layer is given by:

$$M_E = \frac{\tau}{\rho f} \times \mathbf{k} \tag{1.1}$$

where τ is the wind stress, ρ the water density, and f the Coriolis parameter defined as:

$$f = 2\Omega \sin\theta \tag{1.2}$$

where θ is the latitude and $\Omega = 7.27 \times 10^{-5}\, s^{-1}$ is the earth's angular velocity. If L is the horizontal scale of the motion and U a typical horizontal velocity scale, The

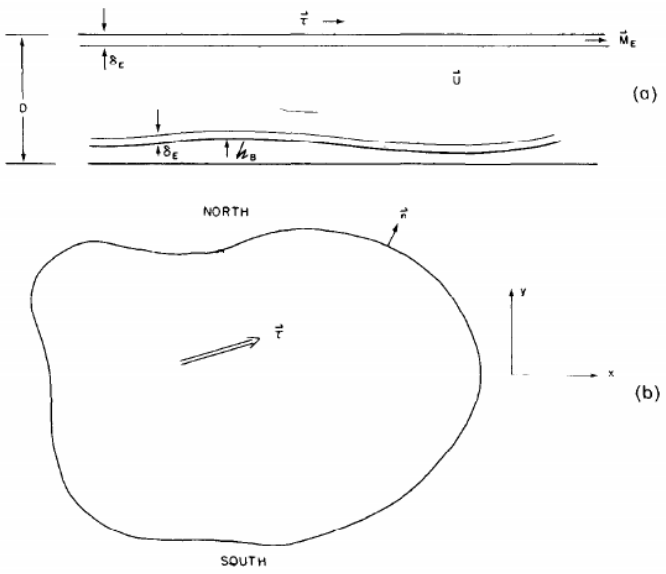

Figure 1.1: Homogeneous model characteristics:(a) τ is the applied wind stress, D is the ocean depth, δ_E is the surface layer and represent also a thin layer over the variable bottom h_B, and M_E is the mass flux of the surface layer. (b) A plan view of the model domain.

Rossby number is defined as:

$$\epsilon = \frac{U}{fL} \tag{1.3}$$

For low value of the Rossby number, the earth's rotation become relevant on the fluid motion and the momentum balance of the interior flow is given by the geostrophic approximation, and the vertical component of the absolute vorticity is:

$$\frac{d}{dt}(\zeta + f) = f\frac{\partial w}{\partial z} + A_H \nabla^2 \zeta \tag{1.4}$$

This state that the vorticity changes as a consequence of vortex-tube stretching of the planetary vorticity filaments and to a weak effect of horizontal diffusion of vorticity. In this equation the variation of the Coriolis parameter with latitude has a fundamental role. It is possible to account for this variation introducing the gradient of the planetary vorticity (the so called β-plane approximation)

$$\beta_0 = \frac{df}{dy} = \frac{2\Omega \cos\theta_0}{r_0} \tag{1.5}$$

This is the only contribute retained for the sphericity of the earth. In the bottom Ekman layer the vertical velocity entering the interior flow is given by the Ekman pumping plus the vertical velocity produced by the topographic lifting of the flow:

$$w(x, y, h_B) = \mathbf{u} \cdot \nabla h_B + \frac{\delta_E}{2}\zeta \tag{1.6}$$

In the upper Ekman layer the vertical velocity is given by the divergence of the mass flux:

$$w(x, y, D) = \nabla \cdot \mathbf{M_E} = \nabla \cdot \left(\frac{\tau \times k}{\rho f}\right) = \mathbf{k} \cdot \nabla \times \frac{\boldsymbol{\tau}}{\rho f} \tag{1.7}$$

Using (1.6) and (1.7) and the fact that the interior is homogeneous and geostrophic, u, v and therefore ζ must be independent from z and (1.4) may be vertically integrated leading to:

$$D\left[\frac{1-h_B}{D}\right]\left\{\frac{d\zeta}{dt}+v\beta_0-A_H\nabla^2\zeta\right\}=f\left\{\mathbf{k}\cdot\nabla\times\frac{\boldsymbol{\tau}}{f\rho}-\frac{\delta_E}{2}\zeta-\mathbf{u}\cdot\nabla h_B\right\} \tag{1.8}$$

where $\frac{df}{dt}=v\beta_0$ has been used.

The non dimensional vorticity equation

The equation (1.8) describing the simple homogeneous model is however a difficult differential equation and can be further simplified. The first step consist in nondimensionalizing the variables. Considering L, U, L/U and τ_0 as characteristic scales for horizontal length, horizontal velocity, time and wind stress. Dimensionless parameters are denoted by primes:

$$\begin{aligned}(x,y)&=L(x',y'), &\zeta&=\frac{U}{L}\zeta',\\(u,v)&=U(u',v'), &\tau&=\tau_0\tau'\end{aligned} \tag{1.9}$$

In the β-plane approximation the Coriolis parameter is defined as:

$$f=f_0+\beta_0 y=f_0\left(1+\frac{\beta_0 L}{f_0}y'\right) \tag{1.10}$$

After some calculations and observing that $\frac{\beta_0 L}{f_0}$ is small in β-plane approximation, the vorticity equation can be written in a simplified and non-dimensional form:

$$\frac{d\zeta}{dt}+\beta v=\frac{\tau_0 L}{\rho D U^2}\nabla\times\boldsymbol{\tau}-r\zeta-\mathbf{u}\cdot\nabla\eta_B+\frac{\nabla^2\zeta}{Re} \tag{1.11}$$

Where umprimed variables are now dimensionless and four non-dimensional number are defined as,

$$\begin{aligned}Re&=\frac{UL}{A_H}, &\beta&=\frac{\beta_0 L^2}{U},\\r&=\frac{\delta_E}{2D_E\epsilon}, &\eta_B&=\frac{h_B/D}{\epsilon},\end{aligned} \tag{1.12}$$

were introduced, and the fact that $h_B/D\ll 1$ has been used. In the ocean Re is large, and r is $\mathcal{O}(1)$ or less. The ocean bottom is considered flat or with very smooth variations so the η_B term can be neglected. Nevertheless β is $\mathcal{O}(10^2)$ for mid-ocean flows. In the mid-ocean, as the vorticity is added by the wind stress, the fluid increase its absolute vorticity by languidly move to higher latitude. This suggest that the appropriate scaling for U should be such as to balance the wind stress curl and the β-term, *i.e.*,

$$\frac{\tau_0 L}{\rho D U^2}=\beta=\frac{\beta_0 L^2}{U} \tag{1.13}$$

and then

$$U=\frac{\tau_0}{\rho D\beta_0 L} \tag{1.14}$$

Since the velocity is geostrophic, u, v and ζ may be written in terms of a geostrophic stream function ψ:

$$u = -\frac{d\psi}{dy}, \qquad v = \frac{d\psi}{dx}, \qquad \zeta = \nabla^2\psi \tag{1.15}$$

For a flat ocean bottom and with the choice of (1.14) for U and (1.15) for u, v and ζ, equation (1.11) may be written in its final form:

$$\boxed{\frac{\partial}{\partial t}\nabla^2\psi + \frac{1}{\beta}\mathbf{J}(\psi, \nabla^2\psi) + \frac{\partial\psi}{\partial x} = \nabla \times \boldsymbol{\tau} - \frac{r}{\beta}\nabla^2\psi + \frac{\nabla^4\psi}{\beta Re}} \tag{1.16}$$

where the second term on the left side is the Jacobian of the Stream function with the relative vorticity term, and represent the advection of relative vorticity by the motion field, *i.e.* the non-linear term, and is defined as:

$$u\frac{\partial\zeta}{\partial x} + v\frac{\partial\zeta}{\partial y} = -\frac{\partial\psi}{\partial y}\frac{\partial\nabla^2\psi}{\partial x} + \frac{\partial\psi}{\partial x}\frac{\partial\nabla^2\psi}{\partial y} \equiv \mathbf{J}(\psi, \nabla^2\psi) \tag{1.17}$$

The boundary conditions

The equation (1.16) requires the specification of boundary conditions on the stream function. On the boundary C of the basin the normal velocity must be specified, and if the basin has rigid boundary and is closed, the normal velocity must vanish on the boundary. Thus, on the boundary:

$$\mathbf{u} \cdot \hat{n} = 0 \quad \text{on } C \tag{1.18}$$

with $\hat{n}$ the unit vector normal to the boundary. Since $\mathbf{u} = \hat{k} \cdot \nabla\psi$, the condition (1.18) is equivalent to the condition that ψ be constant on the boundary, and is possible to choose the constant to be zero if there is a single boundary girdling the basin. (1.18) can be simplified to:

$$\psi = 0 \quad \text{on } C \tag{1.19}$$

The presence of viscous diffusion of vorticity implies the need for an additional dynamic boundary condition on the walls of the basin. The *no-slip* condition demands:

$$\mathbf{u} \cdot \hat{t} \quad \text{on } C \tag{1.20}$$

with $\hat{t}$ unit vector tangent to the boundary. In terms of the stream function this become:

$$\hat{n} \cdot \nabla\psi = 0 \quad \text{on } C \tag{1.21}$$

The boundary layer problem

Based on scale analysis, From equation (1.16) is possible to extract dimensionless variables that are useful to describe the relative importance of each term of the equation:

$$\begin{aligned} \beta^{-1} &= \frac{U}{\beta_0 L^2} = \left(\frac{\delta_I}{L}\right)^2, \\ (\beta Re)^{-1} &= \frac{A_H}{\beta_0 L^3} = \left(\frac{\delta_M}{L}\right)^3, \\ \frac{r}{\beta} &= \frac{\delta_E f/2D\beta_0}{L} = \left(\frac{\delta_s}{L}\right) \end{aligned} \tag{1.22}$$

The three parameters of the steady circulation problem β^{-1}, $(\beta Re)^{-1}$ and $\frac{r}{\beta}$ measure the importance of non-linearity, lateral diffusion and bottom friction respectively. Each of them can also be written as the ratio between a boundary layer scale (δ_I, δ_M, δ_S) and the scale of the interior flow motion L. The assumptions that none, one, or more of these boundary layer scales are dominant compared with the others and with the interior length scale, give rise to the well known linear and non-linear theories of the wind-driven circulation. If the parameter described are all small compared with L the dominant balance is the *Sverdrup relation*, *i.e.*,

$$\frac{\partial \psi}{\partial x} = \nabla \times \boldsymbol{\tau} \tag{1.23}$$

(1.23) describes correctly the behaviour of the interior flow but is not complete. For an idealized wind stress pattern with westerly wind at mid latitudes and easterly trade winds in lower latitudes, the Sverdrup transport is southward everywhere and the mass balance is not satisfied. A region where dynamics differs from the Sverdrup dynamics is needed. This region is find out to be the western boundary where the mass balance must be satisfied. In order to find some analytical results of the vorticity equation some simplifications are required. In the linear theory of Munk (1950) the physics of lateral friction is retained leading to a western boundary layer of thickness δ_M with a strong boundary current. An historic picture of the Munk's results are shown in figure 1.2. If bottom friction is considered the dominant

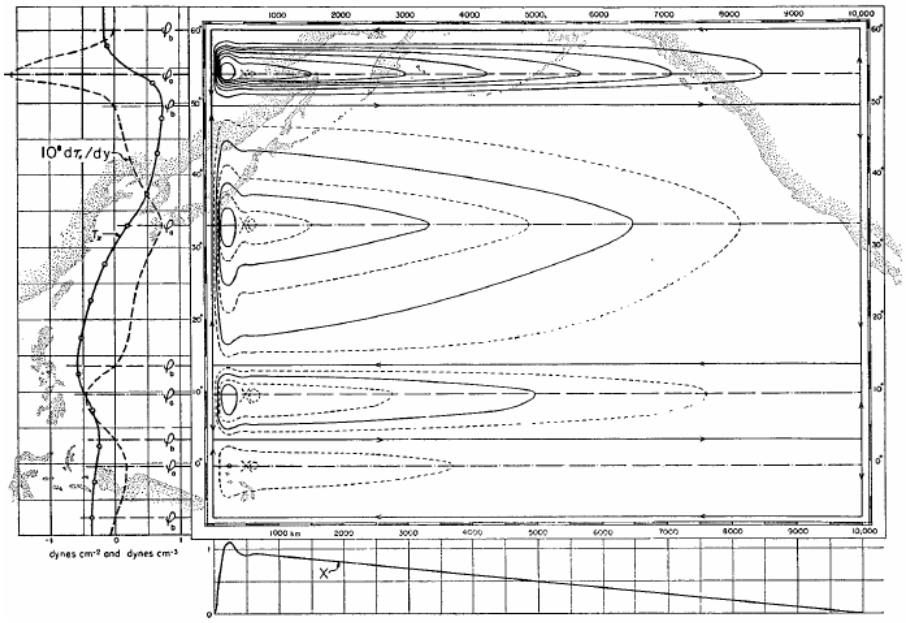

Figure 1.2: The mean annual zonal wind stress and his curl is shown on the left. The central part shows the mass transport streamlines of the Munk's solution.

term, then δ_S is the Stommel's boundary layer thickness (Stommel, 1948). Inertial theories (Charney, 1955; Carrier and Robinson, 1962) retain the non-linear term neglecting the The bottom friction and the lateral diffusion, leading to the formation of an inertial boundary layer δ_I. The discussion will not enter in further details of the results of these theories, but it is to point out that the planetary vorticity gradient, *i.e.* the β-term, is the fundamental parameter needed to reproduce the western boundary intensification of the current, that is one of the most important

feature of the large-scale wind-driven circulation. In the next section the focus will be in numerical modelling of the ocean. Numerical experiments are fundamental to investigate in a fairly easy way the role of the non-linear terms in modifying the ocean circulation and are now a standard way to have some insights in many physical processes that occur in the ocean.

1.2 The numerical ocean modelling

The early studies, such as those briefly discussed above were focused on solving the linearized form of the barotropic vorticity equation of the ocean and neglected the non-linear terms that are difficult to handle analytically. Linear theories require the gradient of the relative vorticity to be small compared to the gradient of the planetary vorticity, *i.e.*, $\frac{U}{\beta_0 L^2} \ll 1$, while observations show that in the western boundary the relative vorticity gradient is of the same order as β_0, so the non-linear effects are important. Moreover others models such those of Charney (1956) and Morgan (1956) retain the non-linear terms but neglected frictional forces, that however must be included in the total circulation problem to achieve a steady solution. These analytical models are indeed useful to have deep insight of the physics of the ocean circulation and of the scales at which each term of the equation act, but can not treat the complete equation as a whole due to high mathematical difficulty in handle partial non-linear differential equations. Numerical experiments are then found to be a good compromise to obtain explicit solutions of the ocean circulation problem. Nevertheless numerical simulations have their own limitations, and the interpretation of the results can not always be straightforward as analytical solutions. The first-ever application of numerical techniques to large scale ocean circulation were carried out by Artem Sarkisyan (1955). Subsequently, efforts by Sarkisyan and his colleagues focused on diagnostic studies of regional extent, such as for the North Atlantic. The technological improvement, and the relative enhancement of computational power of the '60s, together with the experience from atmospheric models lead to the development of a numerical model by Kirk Bryan (1963) at GFDL (Geophysical Fluid Dynamics Laboratory). Bryan applied the finite-differences techniques of numerical weather predictions to solve the barotropic vorticity equation in a rectangular oceanic domain retaining the lateral diffusive term. An interesting result is discussed in Veronis (1966) where the effect of a strong non linear flow is considered. In his work Veronis solve numerically the vertical integrated vorticity equation, but with only the bottom friction as dissipation mechanism, and could therefore apply only the no normal flow boundary condition. The results of his computation are shown in fig. 1.3, and show solutions for increasing values of δ_I/δ_S. At low values of the ratio δ_I/δ_S the solution is indistinguishable from the linear Stommel solution (panel a). As δ_I/δ_S is increased the effects of nonlinearity become more apparent and a slight north-south asymmetry arise due to advection of vorticity. A strong jet along the northern wall appear for δ_I/δ_S of order 2 (panel d) and a strong boundary jet appear on the eastern boundary for $\delta_I/\delta_S = 4$. The panel f show the solution for $\delta_I/\delta_S = 8$. In this case the east-west asymmetry is completely lost. An increase of nonlinearity lead to an increase in the transport of the circulation. In this last case the maximum transport of the anticyclonic cell is of the order of ten times larger than predicted by the Sverdrup theory which then is no more valid in such a

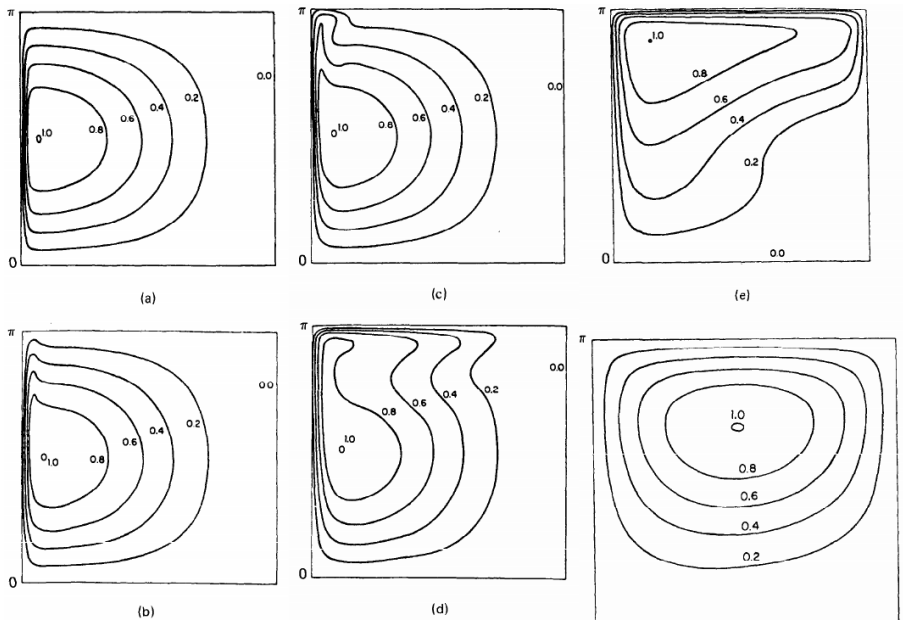

Figure 1.3: Solution of the wind driven circulation problem of Veronis work (1966), with only bottom friction balances the wind input of vorticity. Each panel correspond to an increasing value of the ratio δ_I/δ_S.

limit. The circulation pattern of panel f is very similar to the resonant free inertial mode proposed by Fofonoff as a solution for a free purely inertial model due to the absence of lateral friction and to the fact that $\delta_I \gg \delta_S$.

Ocean model development

The usage of computer computational power applied in solving the dicretized equations allow to retain the non-linear terms that were neglected by previous studies and whose have an important effect in the boundary currents. The purpose of Bryan was to Develop a model capable of simulating the world ocean and in the second half of the 1960s, Bryan helped by Michael Cox (Bryan and Cox 1968a, 1968b; Bryan, 1969) developed a multilevel primitive equations, again formulated using finite differences with second-order spatial accuracy and a leap-frog scheme for time integration. The results of one of the first world ocean circulation numerical experiments for an homogenous model carried out by Bryan and Cox (Bryan and Cox, 1972), are shown in terms of the transport streamlines in a two-day mean after 90 days of integration (fig. 1.4). An efficient numerical integration was achieved with the assumption of a "*rigid lid*" ocean surface. The rigid lid eliminate fast external mode gravity waves found in the real ocean, thus allowing for longer time steps to make the model for practical use for climate studies. They chose the Arakawa B-grid for staggering of tracer and velocity variables, allowing for more accurate numerical calculations of geostrophically balanced motion using the coarse resolution allowed by computers of the day. This model became known as the Bryan-Cox model and was the first *Ocean Global Circulation Model* (OGCM). In 1984 Michael Cox decided to make the Bryan-Cox code freely available to the public. Oceanographers from all around the world started to use and modify the code and the Modular Ocean Model (MOM) arose. Starting from MOM model, a variety of other ocean models were developed, like the Parallel Ocean Program (POP) developed at Los

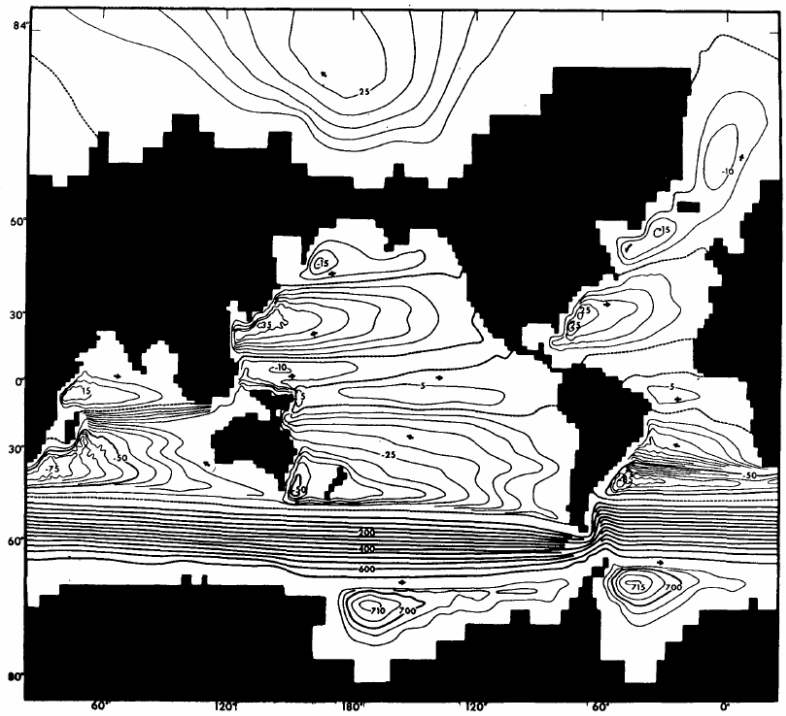

Figure 1.4: Transport streamlines for the case of uniform depth and homogeneous density from one of the first world ocean numerical model (Bryan and Cox, 1972). Units are in $10^6\, tons\, sec^{-1}$.

Alamos National Laboratory, and NEMO model, the one used in this thesis, that has many features in common with MOM. Nevertheless MOM was born to study the large scale circulation, and wasn't capable of properly reproduce the circulation in high resolution coastal area, where the bottom topography has an important role. Discontinuity effects due to a stepwise representation of the bathymetry and sidewall geometry can lead to spurious effects that can be avoided using a terrain-following vertical coordinate (σ-coordinate) that smoothly fits the irregular shape of the domain. One of the first models that uses this implementation of the vertical coordinate is the Princeton Ocean Model (POM) developed by G. Mellor and A. Blumberg (1987) that utilizes the widely used Mellor-Yamada turbulence closure scheme (Mellor and Yamada, 1982). Furthermore, observational evidences show that the water mass transport occurs mainly on isopycnal surfaces rather than on geopotential surfaces. Therefore the former seems the most natural vertical coordinate system to avoid spurious dyapicnal mixing due to numerical representation of advection. Another class of models with isopycnal vertical coordinate emerge, like the Miami Ispoycnal Coordinate Ocean Model (MICOM) (Bleck *et al.*, 1992; Bleck and Chassignet, 1994). In fig.1.5 a possible classifications of ocean models is presented. The last class of ocean models that will be cited here are the Spectral models. Spectral models use a *finite element* method rather than the *finite difference*, and despite the numerical complications and the high computational cost they offer geometrical flexibility with spatial discretization on unstructered grids, high-order convergence rates and dense computations at the elemental level leading to extremely good scalability characteristics on parallel computers. An example for this kind of model is the Spectral Element Ocean Model (SEOM) based on the

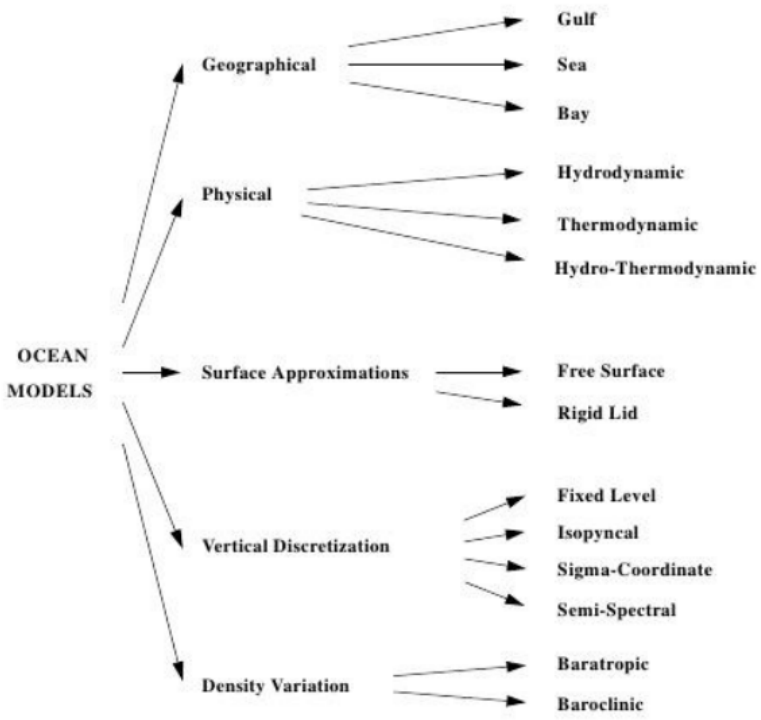

Figure 1.5: An ocean models classification.

spectral element method (Patera, 1984). The spectral element method can be described as a Galerkin finite element method which approximates the solution with a high order polynomial. The last picture of the section, (figure 1.6) shows a global high resolution model output of MIT general circulation model (MITgcm), where the surface currents and temperature are highlighted.

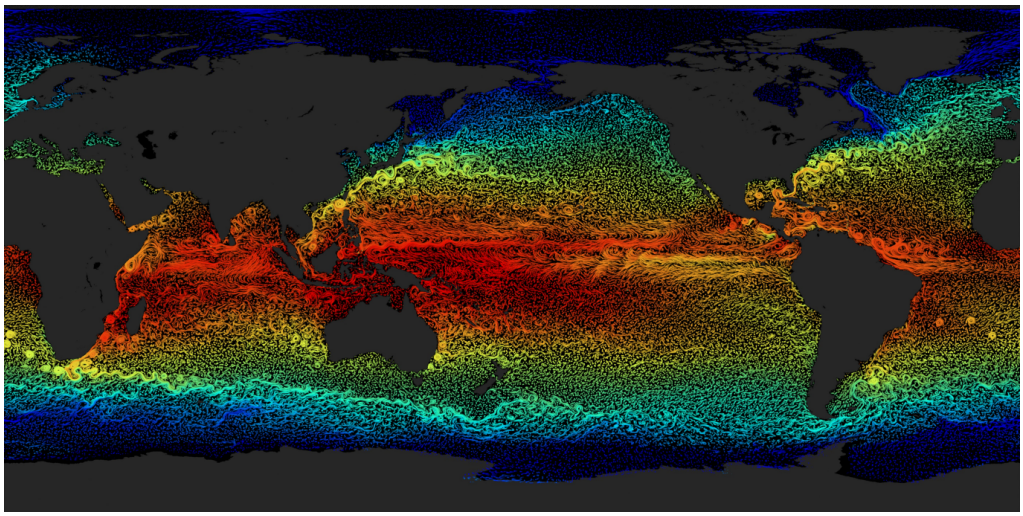

Figure 1.6: High resolution model output from MITgcm (ECCO2, 2011).

1.3 The Mediterranean Sea

The Mediterranean sea is a semi-enclosed, anti-estuarine basin at mid-latitude, between 30° and 46° N of latitude and from 6° W to 36° E in longitude extension. It can be subdivided into two anti-estuarine sub-basin, the western and eastern Mediterranean sea, named respectively WMED and EMED divided by the Sicily strait, which is 300 m deep and 35 km width. It is connected to the global ocean trough the narrow strait of Gibraltar, which is 300 to 900 m deep and whose width is 13 km, and to the Black Sea by the Dardanelles/Marmara Sea/Bosphorus system. The Mediterranean Sea has a complex topography which is determinant for some of the major circulation patterns. The mean depth is 1500 m, the maximum depth is 5267 m reached at Calypso Deep in the Ionian sea, south-west of Pylos in Greece. Maximum depth in both basins (WMED and EMED) are respectively 3785 m in the Tyrrhenian Sea and 4200 m in Ionian-Sea. The WMED major basins are the Alboran Sea, the Algero-Provencal basin and the Tyrrhenian Sea, while The EMED has a more complicated morphology, with two marginals seas, the Adriatic Sea and the Aegean Sea, and two more sub-basin, the Ionian sea and the Levantine basin separated by the island of Crete. The major islands are: Minorca, Majorca, Sardinia and Corsica in the WMED; Sicily, Crete, Rhodes and Cyprus in the EMED. (see fig.1.7).

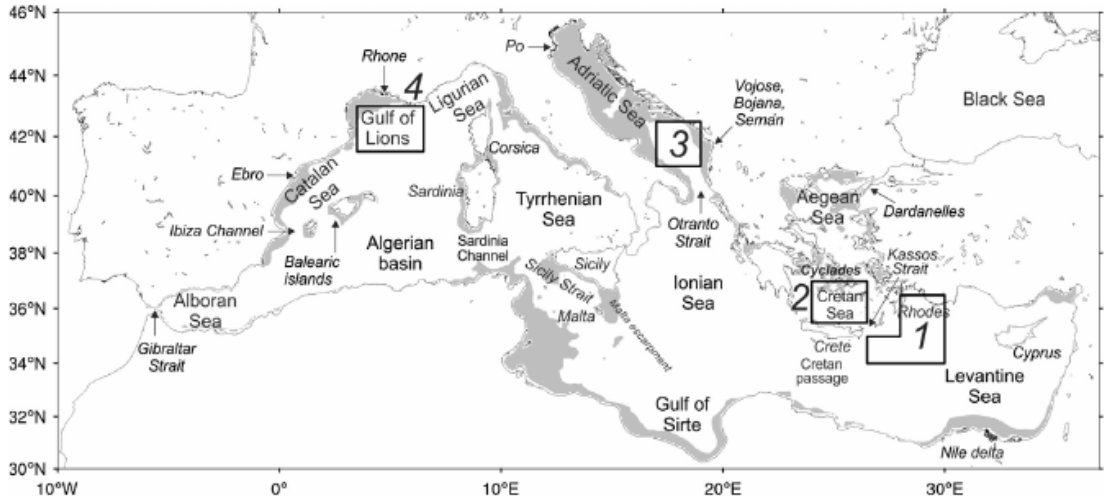

Figure 1.7: Geometry of the Mediterranean Sea and nomenclature for major basins and areas (Pinardi et al., 2015).

1.3.1 The Mediterranean circulation and variability

Many processes which are found fundamental to the general circulation of the world ocean also occur, with different scales, within the Mediterranean. The principal dynamic and thermodynamic forcing are provided by:

- inflow/outflow at Gibraltar strait, with anti-estuarine circulation given by the positive evaporative budget ($E > P + R$)
- wind stress applied on the ocean surface with a strong seasonal variability

- Thermal and evaporative fluxes at the air-sea interface

The inflow/outflow at Gibraltar strait is the controlling mechanism for the salt and mass budget of the overall Mediterranean basin on the time scale of several decades.
The semi-enclosed nature of the basin makes it possible to estimate the heat transport trough the strait, which may be equated (over sufficiently long timescale that the heat storage terms average zero) to a surface flux over the basin. The anti-estuarine circulation of the Mediterranean Sea imply that the flow trough the strait is essentially two layer (fig. 1.8) , with the upper layer consisting of warm, fresh inflow from the Atlantic ($15° C$ and $36.2\,psu$), and the lower layer consisting of a cool, salty outflow ($13.5° C$ and $38.4\,psu$; Lascaratos and Nittis, 1998). Considered the difference in the mean flow in the two layers and the net heat inflow trough the Strait the heat loss over the basin is $7\,W\,m^{-2}$. Low-salinity Atlantic water enters from Gibraltar at the surface and is transformed by intense air-sea interactions into deeper and saltier water that finally exit into the Atlantic.

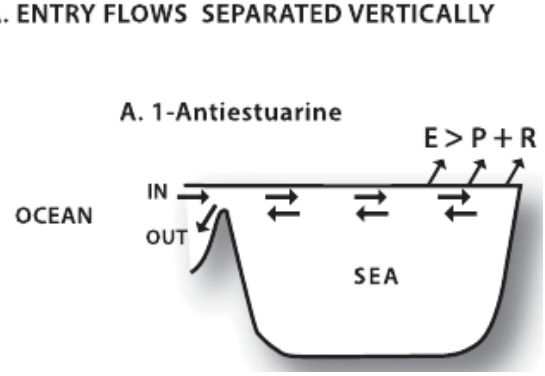

Figure 1.8: basin with anti-estuarine circulation as classified by Pickard and Emery (1982).

Large scale thermal and evaporative fluxes, vertical mixing and deep-water formation processes seasonally provide the complex water formation processes occurring in the Mediterranean Sea. The wind stress forces the circulation at seasonal time scale and on spatial scale of major sub-portions of the Mediterranean. Thus it is possible that the thermal and wind forcing could be acting on the same time scales, with the former inducing water transformation processes and the latter causing the transport and dispersal of such water (Pinardi and Navarra, 1993).

Water masses and thermohaline circulation

According to figure 1.7, Deep-water formation processes occur generally in four sub-basin areas where the principal water masses are formed. The Modified Atlantic Water (MAW) is the Atlantic Water (AW) entering the Strait of Gibraltar and occupies the first $100\,m$ of the water column. It has low salinity and is modified along the path into the Mediterranean Sea, with salinity varying from $36.5\,psu$ to $38.5\,psu$ in the eastern part of the basin. The Levantine Intermediate Water (LIW) is formed by winter convection processes in the Levantine basin (area 1 of fig. 1.7) with a depth range between $300\,m$ and $700\,m$ in WMED and 200 and $400\,m$ in the EMED and spread to the whole Mediterranean with high salinity values reaching

Gibraltar where it forms the Mediterranean outflow into the Atlantic Ocean. The deep-water formation areas of the WMED and of the EMED are geographically separate and the deep-water interface with the LIW is deeper than the sill depth of the Strait of Sicily, preventing exchange between water masses (fig. 1.9).

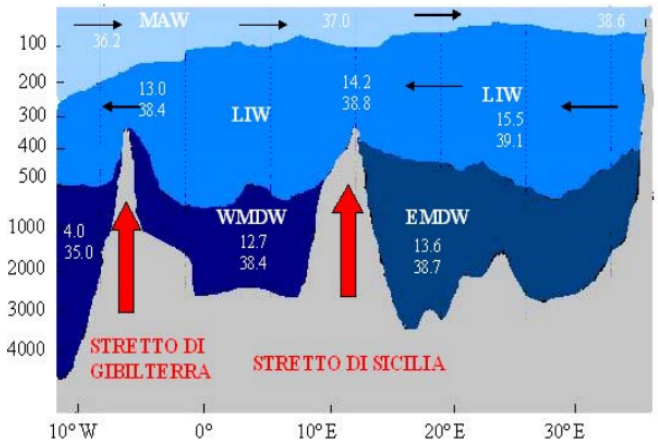

Figure 1.9: Vertical distribution of water masses (Zavatarelli and Mellor, 1995)

In the WMED the Western Mediterranean Deep Water (WMDW) is formed by deep convection processes (Stommel, 1972) in the Gulf of Lions (area 4) where cold and dry winds, causes the sinking and mixing of relatively cold and salty surface to depths of about 1200-1500 m with potential temperature $\theta = 12.70\,°C$ and salinity of $S = 38.40\,psu$. In the EMED the source of the Eastern Mediterranean Deep Water (EMDW) is the Adriatic Sea (area 3), where a water mass around $\theta = 13.60\,°C$ and $S = 38.70\,psu$ is formed in winter and spreads to the whole EMED deep basin. Particular events such the so-called Eastern Mediterranean Transient (EMT), can modify the formation of deep waters in the EMED. During the EMT Cretan Deep Water (CWD) was formed in the Cretan Sea spreading in the Deep layers of the EMED .The atmospheric forcing, *i.e.* the wind stress, and thermal and mass fluxes are strictly interconnected to provide the overall thermohaline circulation (fig. 1.10). It is possible to identify three major conveyor belts.

- a zonal cell forced by the AW entering the Gibraltar Strait and transformed into LIW in EMED with depth range from surface to 500 m and with a decadal timescale
- meridional cells in the WMED and EMED respectively, driven by the Deep water formation processes in the Gulf of Lions and Adriatic Sea (and occasionally in the Aegean Sea) with a multidecadal timescale (50-80 years).

zonal and meridional conveyor belts are strictly connected trough the LIW water mass. The LIW zonal overturning cell sustains the meridional cells contributing to the salt budget of the newly formed deep waters in the Adriatic and Gulf of Lions areas.

The surface and intermediate horizontal circulation

The recent studies of the general circulation have revealed a more complex picture of the circulation, in both WMED and EMED with a delicate interplay between

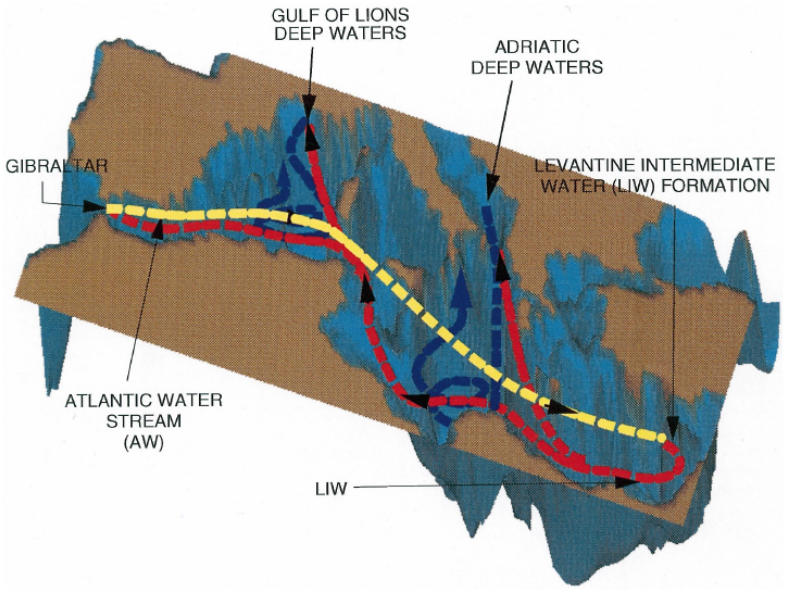

Figure 1.10: The thermohaline circulation of the Mediterranean Sea with the major conveyor belt systems indicated by dashed lines with different colours. Yellow indicate the AW and MAW on the surface spreading from Gibraltar to the eastern part of the basin. Red is the mid-depth LIW that spread from the Levantine basin and form the other part of the zonal conveyor belt. Blue indicate the meridional cell induced by deep waters. LIW branching connect the zonal and meridional conveyor belts

mesoscale and seasonal variability (Robinson et al., 1992; Millot, 1999). Numerical models (Speich et al., 1996) and laboratory experiments (Gleizon et al., 1996) underline the coupling between the regime of the Strait of Gibraltar, the general pattern of the Atlantic flow in the Alboran Sea, and the circulation of the underlying Mediterranean water. The horizontal circulation structures, as depicted by the 25-years reanalysis (Pinardi et al., 2015), can be summarized as in fig. 1.11 and table 1.1 where the nomenclature for the circulation structures are listed. The surface basin circulation is dominated, in the northern part of both western and eastern basins, by large permanent cyclonic gyres (Gulf of Lion Gyre, south-western Tyrrhenian Gyre, Rhodes Gyre...) while in the south-eastern part the basin is dominated by anticyclonic large scale gyres (Mersa-Matruh gyre, Syrte Gyre...). In the middle and south-western Mediterranean the circulation is dominated by a jet-like current both boundary intensified (Algerian current) and free (Atlantic Ionian Stream (AIS) and Mid-Mediterranean Jet).

Among the sub-basin gyres and eddies an active mesoscale activity emerge and contribute to the circulation variability in both eastern and western Mediterranean. The wind stress curl sign has a fundamental role in governing the surface circulation, providing a double-gyre structure of the Mediterranean basin, with a prevailing cyclonic circulation in the northern part, due to a positive wind stress curl sign, and an anticyclonic circulation in the southern part, caused by a negative wind stress curl. At intermediate depth, LIW spreads from the Rhodes Gyre (fig. 1.11, lower panel), where LIW is formed (Lascaratos et al., 1993), with a general westward and northward path with several branching. Particularly important is the path toward the Adriatic and Gulf of Lions areas which brings LIW in the deep convection areas, preconditioning the dense water formation processes and leading to the formation

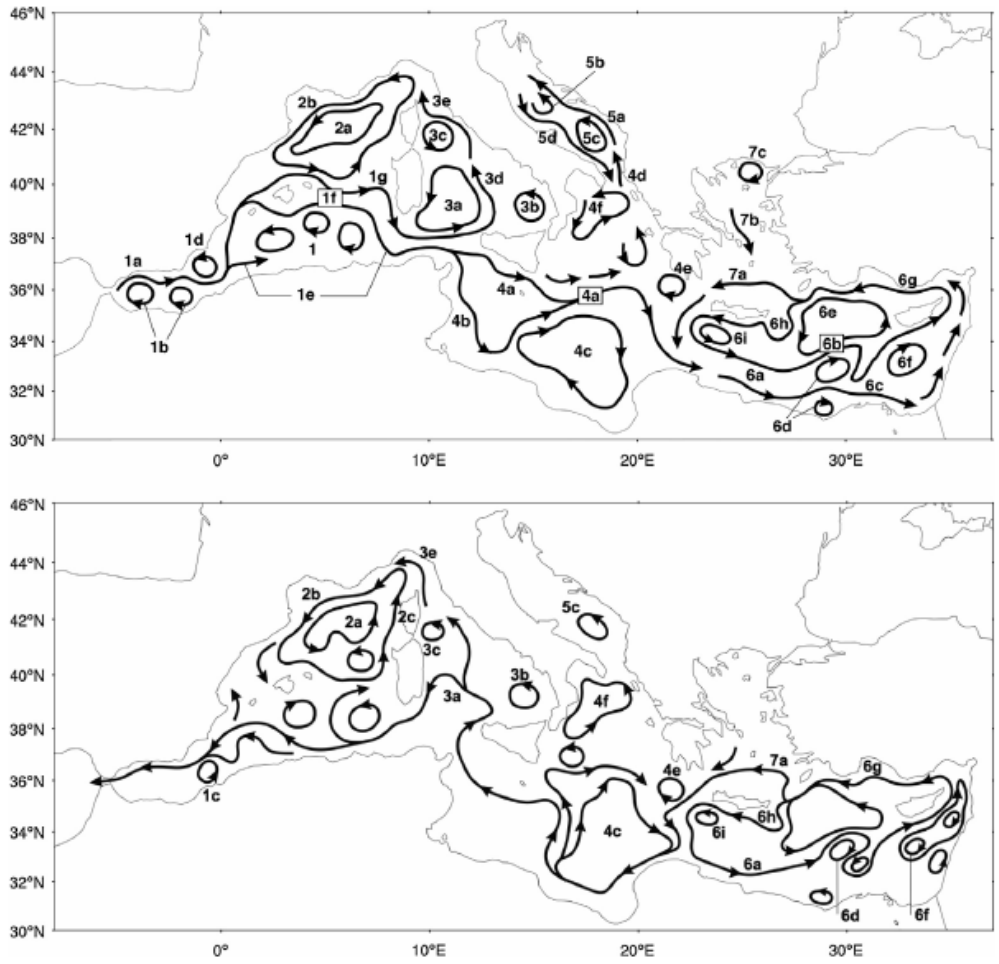

Figure 1.11: Surface (*upper panel*) and intermediate (*lower panel*) circulation as deduced from the 1987-2007 reanalysis mean flow field (Pinardi et al., 2015).

of deep water masses.

Seasonal variability

The variability of the Mediterranean Sea circulation appears to have important component at seasonal and interannual timescales. The seasonal cycle of the external forcing is strictly related to the seasonal variability of the water mass properties and to the large scale circulation (Pinardi and Navarra, 1993; Roussenov et al., 1995; Zavatarelli and Mellor, 1995). The wind stress structure over the basin is shown in fig. 1.12. The two important wind regimes are representative of the seasonal cycle of the atmospheric forcing.

- The Mistral westerly jet (black arrows in fig. 1.12). It is generally a Winter time zonal wind regime with a north-western component in the WMED.
- The Etesian North-easterly jet (Grey arrow in fig. 1.12. A Summer time wind regime with a strong northern component over the EMED.

current systems	Components
System 1	1a: Atlantic Water Current (AWC) 1b: Western and Eastern Alboran Gyres 1c: Almera-Oran front 1d: Almera-Oran cyclonic eddy 1e: Algerian Current segments 1f: Western Mid-Mediterranean Current (WMMC) 1g: Southern Sardinia Current (SCC)
System 2	2a: Gulf of Lion Gyre (GLG) 2b: Liguro-Provenal-Catalan Current (LPCC) 2c: Western Corsica Current (WCC)
System 3	3a: South-Western Tyrrhenian Gyre (SWTG) 3b: South-Eastern Tyrrhenian Gyre (SETG) 3c: Northern Tyrrhenian Gyre (NTG) 3d: Middle Tyrrhenian Current 3e: Eastern Corsica Current (ECC)
System 4	4a: Atlantic-Ionian Stream (AIS) 4b: Sicily Strait Tunisian Current (SSTC) 4c: Syrte Gyre (SG) 4d: Eastern Ionian Current (EIC) 4e: Pelops Gyre (PG) 4f: Northern Ionian Cyclonic Gyre
System 5	5a: Eastern South-Adriatic Current (ESAC) 5b: Middle Adriatic Gyre 5c: South Adriatic Gyre 5d: Western Adriatic Coastal Current (WACC)
System 6	6a: Cretan Passage Southern Current (CPSC) 6b: Mid-Mediterranean Jet 6c: Southern Levantine Current (SLC) 6d: Mersa Matruh Gyre System (MMGS) 6e: Rhodes Gyre (RG) 6f: Shikmona Gyre System (SGS) 6g: Asia Minor Current 6h: Ierapetra Gyre (IPG) 6i: Western Cretan Cyclonic Gyre
System 7	7a: Cretan Sea Westward Current (CSWC) 7b: Southward Cyclades Current (SWCC) 7c: North Aegean Anticyclone

Table 1.1: Nomenclature for surface and intermediate depth circulation

The curl of the wind stress associated with the wind stress lead to a double-gyre structure of the circulation as mentioned above. At the eastern flank of the jets positive vorticity is induced, leading to cyclonic circulation while at the western flank the vorticity is negative with anticyclonic circulation. This wind induced gyres interpretation of the circulation was formulated in numerical simulation of Pinardi and Navarra (1993) and Molcard (1998b). Realistic simulations consider also modifications of gyres due to the local topography and viscous boundary layers whose effects on the potential vorticity balance are of the same order of magnitude of the wind stress curl (Pinardi and Navarra, 1993). According to Pinardi and Masetti (2000) important aspects of the seasonal variability are:

- The surface water mass formation cycle (Hecht et al., 1988).
- The seasonal reversal of currents in different portions of the basin (Tziperman and Malanotte-Rizzoli, 1991).
- The strength of the mesoscale flow field (Ayoub et al., 1998).
- The winter deep convection sites in the Gulf of Lion, Adriatic Sea and Rhodes Gyre (Leaman and Shott, 1991; Lascaratos et al., 1993; Artegiani et al., 1997a, b).

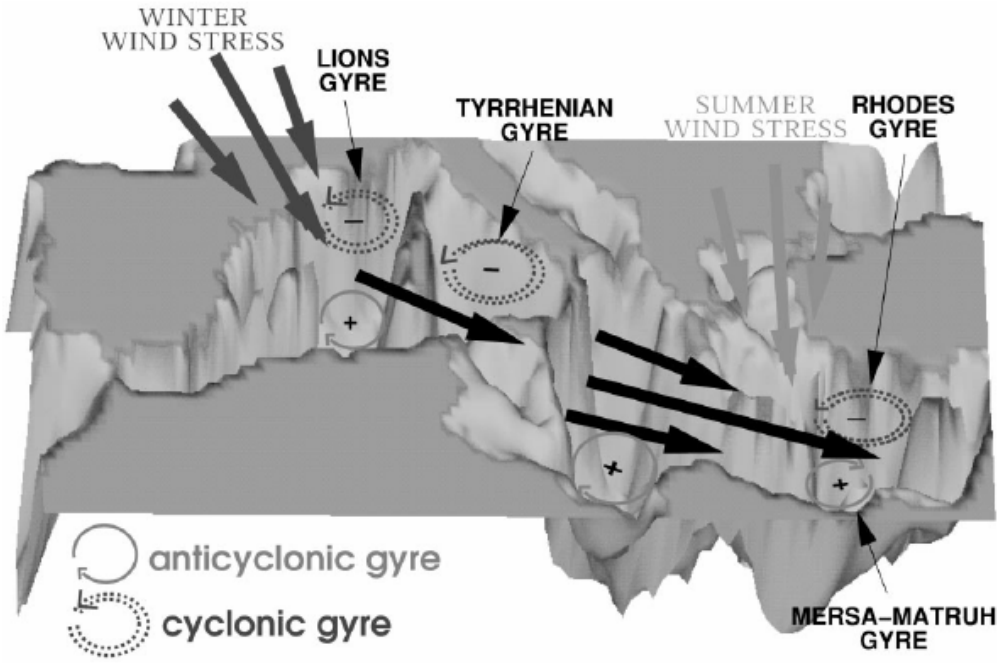

Figure 1.12: Schematic of the wind-driven surface circulation. The black thick arrows indicate the prevailing wind stress field direction during Winter. The grey thick arrows indicate the wind stress field during Summer. Thin dashed arrows indicate anticyclonic circulation while wile thin full arrows indicate cyclonic circulation (Pinardi and Masetti, 2000).

Interannual variability

Interannual changes in the surface meteorological forcing are considered an important component of the interannual variability of the Mediterranean Sea circulation, However interannual variations are more difficult to explain, since many different mechanism may contribute strongly. Important aspects of the interannual variability concern:

- The intermediate and deep water mass formation rates (Nittis and Lascaratos, 1998; Castellari et al. 1999).
- The large variations in volume transport between basins at the Straits (Astraldi et al., 1995).
- The sudden switches in the deep water mass formation areas for the EMED (Roether et al., 1996).
- The changes in the flow direction in several regions (Hecht et al., 1988; Nittis et al., 1993; Artale et al., 1994; Pinardi et al. 1997).
- The abrupt changes in LIW characteristics (Hecht, 1992).

External atmospheric forcing may have an immediate effect on the ocean circulation trough anomalous fluxes of momentum, heat and freshwater, which modify vertical mixing depths. Meteorological forcing may also have delayed effect on circulation modifying surface and intermediate water dispersal paths which in turn

modify the hydrography for subsequent winter formation events. Numerical simulations (Pinardi et al., 1997) show that WMED and EMED response to interannual changes in external atmospheric forcing, *e.g.* an anomalous Winter event, may be different. In the EMED the interannual variability can overcome the amplitude of the seasonal cycle, while in the WMED the circulation exhibit always a strong seasonal signal. A significant role in the interannual variability can be attributed to the internal non-linear ocean dynamics, such as the unstable mesoscale eddy field, that produce a chaotic element of redistribution of water masses.

Mesoscale variability

The Mediterranean have a dominant mesoscale circulation component (Robinson et al., 1987; Ayoub et al., 1998). The eddy field is similar to the world ocean, but also specific to the basin and is constituted by semi-permanent eddies that, due to this specific persistency in time, may be also called gyres (Iera-Petra gyre, Pelops gyres). The mesoscale variability of the basin could be an important component of the interannual signal in the Mediterranean, since the small Rossby radius of deformation produces slow phase speed for the Rossby waves in the basin, possibly producing a longer lived eddy field. Three factor probably contribute in the time persistency of the eddy field: the non-linear dynamical balances, the specific atmospheric forcing and the bathymetry. For the Mediterranean the Rossby radius of deformation is found to vary from 5 to 12 km in the whole Mediterranean. This value of the Rossby radius sets the scale at which important energy redistribution processes of the mesoscale field occur and lock this scale 25-60 km that is the observed scale of the mesoscale activity in the Mediterranean Sea (Robison et al., 1987; Paschini et al., 1993). The importance of the non-linear dynamics in the ocean is inversely proportional to the horizontal scale of the flow field. A measure of the importance of the non-linear advective term on the mesoscale eddie filed is given by the ratio of the Coriolis force term with respect of the non-linear term in the momentum equations. This value is called the β Rossby number, defined as:

$$\beta = \frac{\beta_0 L^2}{U_0} \tag{1.24}$$

In the Mediterranean sea $\beta_0 = 10^{-11}\, m^{-1}\, s^{-1}$ is the β plane parameter for the central latitude θ_0, $L = 10\, km$ is the horizontal scale and $U_0 = 0.01\, m\, s^{-1}$ is the velocity scale, resulting in a beta Rossby number of $\beta = 0.2$. Compared to the same value for the North Atlantic where $L = 50\, km$, $U_0 = 0.1\, m\, s^{-1}$ and $\beta = 2$, the value is small. Thus, in the Mediterranean the mesoscale eddy field is supposed to be dominated by strong non-linear interactions driving large inverse energy cascades (Rhines, 1979), inhibiting planetary waves dynamics, thus enhancing the persistency of the eddies in the basin. Many well known example of the mesoscale activity in the Mediterranean may be listed. Hydrodynamic instabilities of the AW entering the Gibraltar Strait are strongly connected to the eddy fields and ring-like structures emanating from the Algerian current (Millot, 1991). Eddies generate also in The EMED. The Mid-Mediterranean jet could detach eddies by mixed barotropic/baroclinic instabilities (Golnaraghi, 1993), and gyre-like structures.

1.4 NIR phenomenon

Since the early studies of Ovchinikov and Fedoseyev (1965), who already state a reversal of the current in the Ionian Sea, seasonal and interannual changing in the Mediterranean circulation were well observed and documented (Hecht et al., 1988; Pinardi et al. 1997). The 20-years-long reanalysis of the Mediterranean Sea allow to describe consistently the structure and the dynamics of the circulation and to study the time-mean circulation and its low-frequency, decadal components. A schematic representation of the circulation emerging from the reanalysis was already shown in fig. 1.11 (Pinardi et al., 2015). In this section what is analysed is the decadal variability of the circulation, that reveals interesting patterns. The reanalysis dataset can be divided into two periods. The first decade going from 1987 to 1996 (Period A) and the second decade between 1997 and 2006 (Period B). Period A coincides with a stable positive NAO index and it overlaps with the EMT event period. The decadal mean for the two period is shown in figure 1.13.

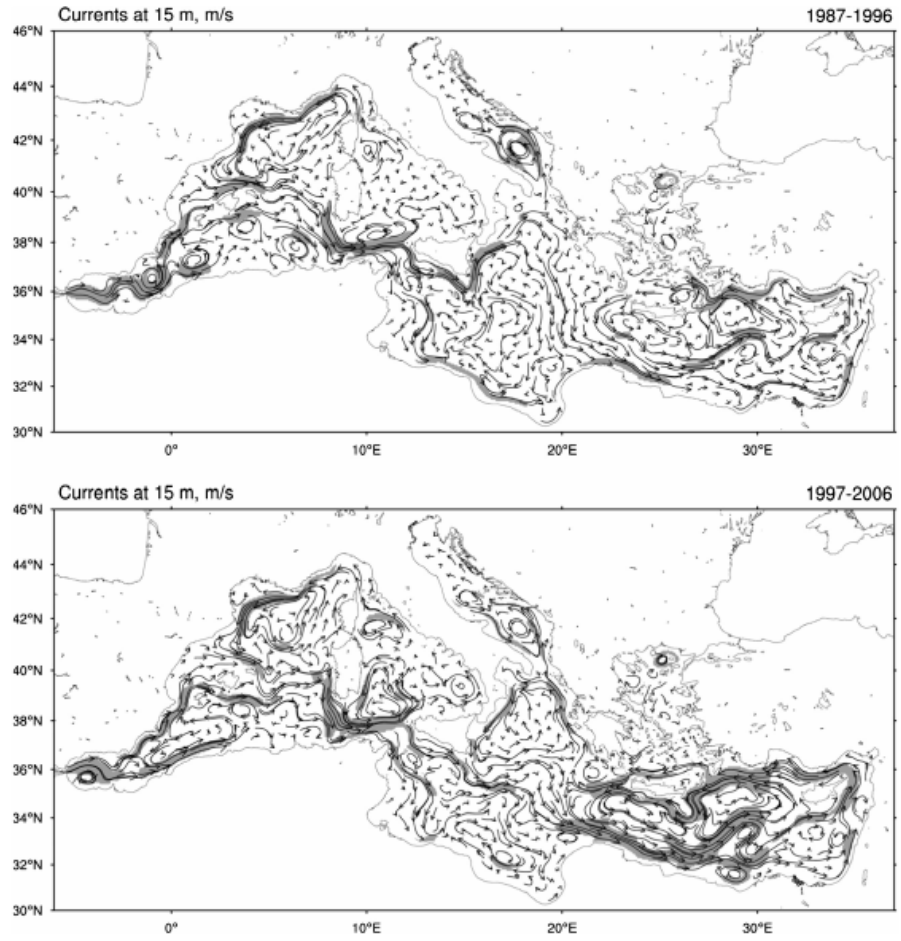

Figure 1.13: Decadal mean of the surface circulation for period A (upper panel) and period B (lower panel) from Pinardi et al. (2015).

In the WMED the largest changes occur in the Alboran and Tyrrhenian Sea, however the largest changes between period A and period B occur in the EMED, where a current reversal takes place in the northern Ionian Sea and large differences in gyres location and current amplitude are evident in the Levantine basin and in

the Cretan passage. During the period A, the AIS shows a large meander northward along the Italian coast, giving rise to an overall anticyclonic circulation in the northern Ionian basin. In period B the circulation is cyclonic and the AIS cut across the basin. This manifestation of the decadal circulation variability of the Mediterranean is called the Northern Ionian Reversal phenomenon (NIR) and is connected at the surface with the shift of the AIS position. Such a phenomenon was already observed for the same periods by surface drifters measurements (Poulain et al., 2012) and by satellite altimetry (Larnicol et al., 2002; Borzelli et al., 2009). The possible periodicity of the NIR phenomenon has to be verified by a longer reanalysis reconstruction. Nevertheless numerical simulations studies have documented a reversal from cyclonic to anticyclonic of the current in the northern Ionian Sea around the 1987 (Korres at al., 2000; Demirov and Pinardi, 2002) connecting the reversal with interannual changes in the prevalent wind stress curl sign.

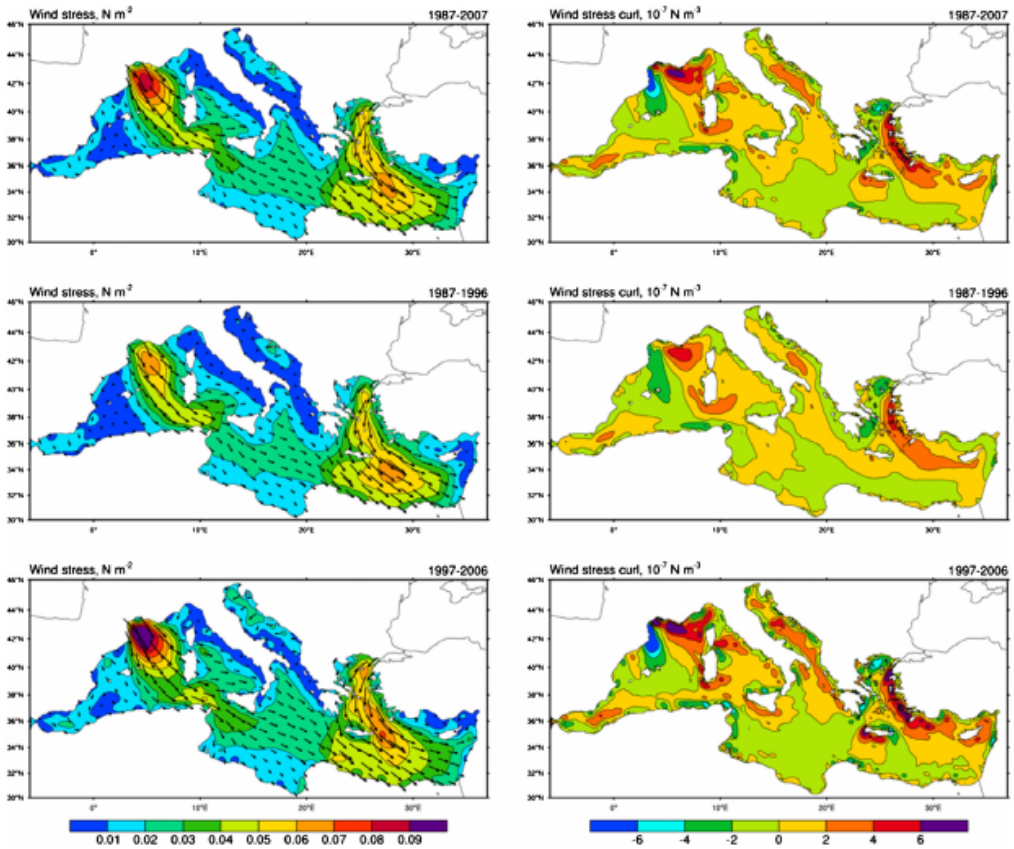

Figure 1.14: Wind stress (lef panels) and wind stress curl (right panels) average over 1987-2007, and for period A and period B(Pinardi et al., 2015)

Analysis of the barotropic wind driven circulation from the reanalysis dataset (Pinardi et al., 2015) show an evident correlation between the barotropic flow field and the surface and intermediate circulation structures indicating the importance of the mean basin scale barotropic wind driven circulation. In particular is evident how in the northern Ionian Sea the average wind stress curl changes sign going from period A to period B suggesting a connection between the wind stress curl and the NIR phenomenon. Such a point of view is not shared by Borzelli et al. (2009) and Gacic et al. (2011) that attribute the reversal of the surface circulation in the northern Ionian Sea to a baroclinic vorticity production due to strong density

gradient on the water column. Diagnostic study of the NIR phenomenon will be carried out on the reanalysis dataset, satellite observations and model output, in chapter 4 where an index (NIR index) is used to evaluate the circulation in the northern Ionian Sea exploiting the SSH values.

1.5 Thesis objectives

The aim of this thesis is to evaluate the role of the wind stress forcing on the Mediterranean Sea circulation focusing on the currents in the northern Ionian Sea to investigate on the NIR phenomenon.
The scientific question is how the wind stress amplitude and the wind stress curl can influence the Mediterranean Sea circulation and the reversal of the current in the northern Ionian Sea?
To answer such a question numerical simulations are carried out with the NEMO model at $\frac{1}{8}^{\circ}$ of horizontal resolution adapted for the Mediterranean Sea. Sensitivity experiment are realized using different wind dataset and physics parametrizations, and the response of the Mediterranean circulation is described in chapter 3.

Chapter 2

The ocean numerical Model

In this chapter the numerical models used for the simulations of the Mediterranean circulation are described and discussed. The NEMO ocean model implemented in SURF numerical platform is the choice for this thesis. SURF provides pre and post processing tools, while NEMO realizes the numerical computation that will be discussed in chapter 3. In the last section the characteristics of the Reanalysis datasets used for the diagnostic study in the chapter 4 are described.

2.1 NEMO Ocean model

The NEMO (Nucleus for European Modelling of the Ocean, Madec, 2008) is a state-of-the-art modelling framework for oceanographic research, operational oceanography, seasonal forecast and climate studies. NEMO is composed by 5 major components:

- the blue ocean (ocean dynnamics, NEMO-OPA)
- the white ocean (sea ice, NEMO-LIM)
- the green ocean (biogeochemistry NEMO-TOP)
- the adaptive mesh refinement software (AGRIF)
- the assimilation component (NEMO-TAM)

The NEMO-OPA (Océan Parallélisé) component is based on a finite-difference model, written in Fortran programming language, that solves the primitive equations,*i.e.* the Navier-Stokes equations (under the hydrostatic and Boussinesq approximations) along with a turbulence closure scheme and a non-linear equation of state, which couples the two active tracers (temperature and salinity) to the fluid velocity. The 3-dimensional space domain is discretised by a structured Arakawa-C grid (Mesinger and Arakawa, 1976) where the model state variables are horizontally/vertically staggered (2.1). Prognostic variables, *i.e* variables directly solved by model equations, are temperature, salinity and sea surface height, located in the centre of the cell(T-grid) and the 3-D velocity field located in the west/east and south/north edges of the cell for the zonal, U, and meridional, V, horizontal component respectively, and the vertical component W, computed at the bottom and top interfaces of cell(W-grid). The vector invariant form of the primitive equations provides a set of six equations(namely the momentum balance, the hydrostatic

equation, the incompressibility equation, the heat and salt conservation equation and an equation of state):

$$\frac{\partial \mathbf{U}_h}{\partial t} = -\left[(\nabla \times \mathbf{U}) \times \mathbf{U} + \frac{1}{2}\nabla\left(\mathbf{U}^2\right)\right]_H - f\mathbf{k} \times \mathbf{U}_h - \frac{1}{\rho_0}\nabla_h p + \mathbf{D}^{\mathbf{U}} + \mathbf{F}^{\mathbf{U}} \quad (2.1a)$$

$$\frac{\partial p}{\partial z} = -\rho g \quad (2.1b)$$

$$\nabla \cdot \mathbf{U} = 0 \quad (2.1c)$$

$$\frac{\partial T}{\partial t} = -\nabla \cdot (T\mathbf{U}) + D^T + F^T \quad (2.1d)$$

$$\frac{\partial S}{\partial t} = -\nabla \cdot (S\mathbf{U}) + D^S + F^S \quad (2.1e)$$

$$\rho = \rho\,(T, S, p) \quad (2.1f)$$

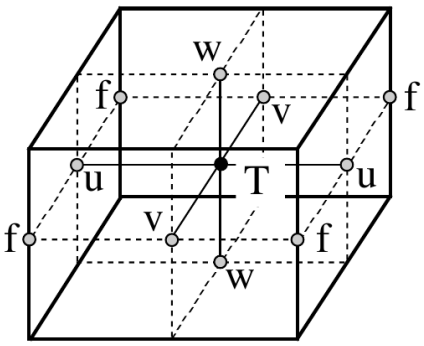

Figure 2.1: Arrangement of variables. t indicates scalar points where temperature, salinity, density, pressure and horizontal divergence are defined. (u,v,w) indicates vector points, and f indicates vorticity points where both relative and planetary vorticities are defined.

A special attention is required for the treatment of the vertical direction. There are three main choices for the vertical coordinate: z-coordinate with full step bathymetry, a z-coordinate with partial step bathymetry, or generalized terrain following s-coordinate. Hybridation of the three main coordinates are also available as shown in figure 2.2.

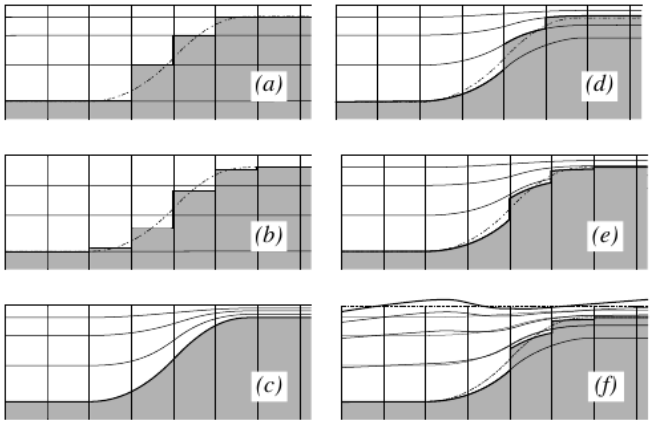

Figure 2.2: the ocean bottom as seen by the model: (a)z-coordinate with full step, (b)z-coordinate with partial step, (c)terrain following s-coordinate. (d)(e)(f) are hybrid s-z coordinate.

The primitive equations are expressed in the $(\mathbf{i}, \mathbf{j}, \mathbf{k})$ orthogonal vector system, linked to the earth such that $\mathbf{k}$ is the local upward vector, and $(\mathbf{i}, \mathbf{j})$ are the two horizontal vector orthogonal to $\mathbf{k}$. $\mathbf{U}$ represent the vector velocity defined as, $\mathbf{U} = \mathbf{U}_h + w\mathbf{k}$, with $\mathbf{U}_h$ be the horizontal velocity, T the potential temperature, S the salinity, ρ the *in situ* density. ∇ is the generalised derivative vector operator in $(\mathbf{i}, \mathbf{j}, \mathbf{k})$ directions, t is the time, z is the vertical coordinate, ρ_0 is the reference density, p the pressure, $f = 2\mathbf{\Omega} \cdot \mathbf{k}$ is the Coriolis acceleration, with Ω the Earth's angular velocity vector, and g is the gravitational acceleration. $\mathbf{D}^{\mathbf{U}}$, D^T and D^S are the parametrisations of small-scale physics for momentum, temperature and salinity, and $\mathbf{F}^{\mathbf{U}}$, F^T and F^S are the surface forcing terms. The following assumptions are made from scale considerations:

1. **Spherical earth approximation** : geopotential surfaces are assumed to be spheres, so that gravity is parallel to the earth radius

2. **Thin-shell approximation** : the ocean depth is neglected compared to the earth radius

3. **Turbulent closure hypothesis** : turbulent fluxes representing small-scale physics processes are expressed in terms of large scale features

4. **Boussinesq hypothesis** : state that density variations are considered only in their contribution in the buoyancy force

5. **Hydrostatic hypothesis** : the vertical momentum equation is reduced to a balance between the vertical pressure gradient and the buoyancy force(convective processes are removed from the Navier-Stokes equations and must be parametrised)

6. **Incompressibility hypothesis** : three dimensional divergence of the velocity vector is assumed to be zero

2.1.1 Boundary conditions

One of the fundamental issue in solving (both analytically or numerically) partial differential equations (PDE), regards the definitions of the boundary conditions. In a complex domain such of that of the global ocean a correct definition of the boundary conditions is even more important. In this section the available NEMO settings to define the boundary conditions are listed and discussed. The ocean is bounded by complex coastline, a bottom topography and an air-sea or ice-sea interface at its top. These boundaries can be defined by two horizontal surfaces, $z = -H(i,j)$ and $z = \eta(i,j,k,t)$, where H is the depth of the ocean bottom, and η the height of the free sea surface(figure 2.3). H and η are usually referenced to a mean sea surface, $z = 0$.

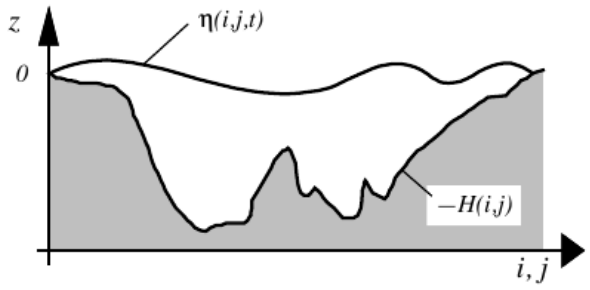

Figure 2.3: the ocean boundary sea surfaces , $z = -H(i,j)$ and $z = \eta(i,j,k,t)$. Both surfaces are referenced to $z = 0$

Trough this two boundaries the ocean can exchange fluxes of heat, fresh water, salt and momentum with the solid earth, continental margins and the atmosphere.

Solid earth-ocean interface : heat and salt fluxes trough tea sea floor are small and can be neglected.

$$A^{vT} \frac{\partial (T,S)}{\partial z}\bigg|_{z=-H} = 0 \tag{2.2}$$

where A^{vT} is the eddy diffusivity for the temperature and salinity. For the momentum the condition is that there is no flow across solid boundaries, *i.e.* the velocity normal to the ocean bottom and coastlines is zero. The boundary condition on the tangential velocity requires a more specific treatment, because it influences the relative vorticity and momentum diffusive trends, and is required in order to compute the vorticity at the coast. Four different type of lateral boundary conditions are available. These are:

free-slip boundary conditions, where the tangential velocity at the coastline is equal to the offshore velocity.

no-slip condition, where the velocity at the coastline is zero assuming a linear decrease from the closest ocean velocity grid point;

partial-free slip boundary conditions where there is some friction added to reduce tangential velocity at the coastline.

strong no-slip boundary conditions where the friction is stronger than in in the no-slip case.

The kinematic boundary condition at the bottom is:

$$w = -\mathbf{U}_h \cdot \nabla_h (H) \tag{2.3}$$

in addition there is a momentum exchange between ocean and the sea floor due to frictional processes parametrised in terms of turbulent fluxes using bottom and/or lateral boundary conditions. Its specifications depends on the nature of the physical parametrisation used for $\mathbf{D}^{\mathbf{U}}$ defined as:

$$\mathbf{D}^{\mathbf{U}} = \frac{\partial}{\partial z}\left(A^{vm}\frac{\partial \mathbf{U}_H}{\partial z}\right) \tag{2.4}$$

With A^{vm} be the vertical eddy viscosity coefficient.

$$A^{vm}(\frac{\partial \mathbf{U}_H}{\partial z})\Big|_{z=-H} = \mathcal{F}_H^{\mathbf{U}} \tag{2.5}$$

where $\mathcal{F}_H^U$ represent the downward flux of horizontal momentum.

Atmosphere-ocean and land-ocean interface : the kinematic surface condition at the surface is:

$$w|_{z=\eta} = \frac{\partial \eta}{\partial t} + \mathbf{U}_h|_{z=\eta} \cdot \nabla_h (\eta) + P + R - E \tag{2.6}$$

Where P is the precipitation, E is the evaporation and R is river runoff at the river estuary divided by the cross sectional area of the estuary. Atmosphere and ocean also exchange horizontal momentum (wind stress), and heat. The two component of the stress,τ_u and τ_v, are interpolated on the u and v-point of the model grid. They are applied as a surface boundary condition of the momentum vertical mixing trend:

$$\left(\frac{A^{vm}}{e_3}\frac{\partial \mathbf{U}_h}{\partial z}\right)\Big|_{z=1} = \frac{1}{\rho_0}\begin{pmatrix}\tau_u\\ \tau_v\end{pmatrix} \tag{2.7}$$

The surface heat flux can be written:

$$A^{vT}\frac{\partial T}{\partial z}\Big|_{z=\eta} = \frac{Q}{\rho_0 C_p} \tag{2.8}$$

where Q represent the non penetrative net heat flux at the surface, $\rho = 1020\,kg/m^3$ is the reference density and $C_p = 4000\,J/(kg\,K)$ is the specific heat. For salinity it is:

$$A^{vT}\frac{\partial S}{\partial z}\Big|_{z=\eta} = (E - P - R)\,S|_{z=\eta}\rho_0 \tag{2.9}$$

Open boundary conditions : the open boundary is necessary for model configurations limited to an oceanic region or a basin which communicates with global ocean. In this boundary the perturbations generated inside the computational domain have to leave it without deterioration of the inner model solution. However an open boundary also has to let information from the outer ocean enter the model and should support inflow and outflow conditions. Two different numerical algorithm are adopted to treat open boundaries depending on the prognostic variables. For the barotropic velocity the *Flather radiation scheme*(Flather,1994) is used, which allow gravity waves generated internally to exit the model boundary, and has the form:

$$U = U_e + \frac{c}{h}(\eta - \eta_e) \tag{2.10}$$

For baroclinc velocity, active tracers and sea surface height the *flow relaxation scheme*(Davies 1976, Engerdhl 1995) is considered. It applies a simple relaxation scheme of the model field to externally-specified value over a zone next to the edge of the model domain and takes the form:

$$\phi(d) = \alpha(d)\phi_e(d) + (1 - \alpha(d))\,\phi_m(d), \qquad d = 1, N \tag{2.11}$$

where ϕ represent a prognostic variable of the model, ϕ_m is the model solution and ϕ_e is the specified external field. d is the discrete distance and α a parameter that varies from 1 at $d = 1$ to a small value at $d = N$.

2.2 SURF ocean model platform

SURF, the *Structured and Unstructured grid Relocatable Ocean platform for Forecasting* (Trotta et al., 2016), is a numerical platform developed for short-time forecasts and designed to be embedded in any region of the large scale Mediterranean Forecasting system(MFS) via downscaling. It is based on the NEMO structured model described above and can be coupled with the wind wave-model SWAN based on the standard NEMO-SWAN configuration. It implements also an unstructured model named SHYFEM, useful for modelling complex coastal domain. It is designed to be the "child" of a "father" model with normally a lower horizontal and vertical resolution. The father model provide initial and lateral boundary conditions for the SURF child components. SURF is working on a virtual machine where the model components are connected to a pre- and post-processing tools that are specifically developed and optimise for SURF in order to reduce the latency of the computation, and to have efficient memory usage. The pre-processing phase allow interpolation of input data on the model domain. The post processing allow to perform diagnostic analysis and visualization procedures. Both pre- and post-processing operations are written in NCL, NCO and Python programming languages. In the following section the work-flow of SURF platform is described.

2.2.1 SURF work flow

The work flow of SURF can be resumed in five steps as shown in figure 2.4. These steps are described below:

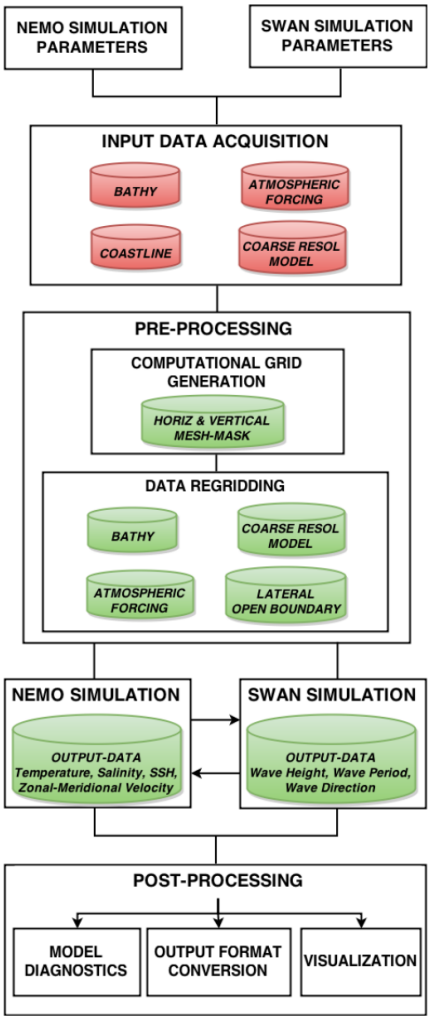

Figure 2.4: work-flow of the relocatable ocean platform SURF, based on NEMO-SWAN coupled model (Trotta et al., 2016).

Simulation parameters : input simulation parameters have to be chosen properly for the specific experiment that one wants to carry out with the implemented models.

Input Datasets : in this step one has to provide input datasets to needed for the model run. These datasets are: (1) Bathymetry, (2) the coastline, (3) coarse resolution model input fields and (4) the atmospheric surface fields. Ocean input fields are normally downloaded from the operational Mediterranean Forecasting System (MFS) while atmospheric forcing is provided by the European Centre Medium-range Weather Forecast (ECMWF) products.

Pre-processing operations : after data acquisition the generation of the horizontal and vertical grid is performed. Then input data are interpolated on the model child grid providing the forcing, boundary and initial conditions. The Sea-Over-Land (SOL) procedure provide extrapolations of the fields values on the areas where the parent model solutions are not defined.

Model run : now the program proceeds with code compilation, together with

data upload in the local database, and then numerical integration starts and produces the final output files.

Post-processing operations : output can be converted in one of the supported format, and data analysis can be performed. Visualizations procedures can be activated in order to display the resulting output fields.

2.3 Reanalysis Datasets

Reanalysis are a method to combine historical observational data with numerical ocean model simulations with the help of a data assimilation scheme. Data assimilation procedures assure the model output to be corrected and coherent with observations. The reanalysis represents a valuable tool for climate monitoring and process studies, long-range forecasts and regional studies. In chapter 4 a diagnostic study is based on the analysis of the 27 years (1987-2014) Copernicus Marine Environment Monitoring Service (CMEMS) reanalysis dataset (Simoncelli et al., 2014), CMCC Global Ocean Reanalysis System (C-GLORS) from CMCC (Storto and Masina, 2016) and a 61 years (1955-2015) reanalysis from Nextdata project (NextData_RR, Fratianni et al., 2017), that are briefly described in this section. Since the CMEMS reanalysis, Nextadata_RR and C-GLORS share many special features, only the fundamental differences between the datasets will be pointed out. The monthly climatology of Temperature and Salinity computed from the CMEMS reanalysis is used in the numerical experiments described in the next chapter as initial and boundary conditions.

2.3.1 CMEMS reanalysis

CMEMS has produced a reanalysis for the Mediterranean Sea with the 3.4 version of the NEMO ocean model to solve the primitive equations at eddy-permitting horizontal resolution of $\frac{1}{16}^\circ \times \frac{1}{16}^\circ$ (6-7 km) and 72 unevenly spaced vertical levels and provides the 3D, daily and monthly mean fields of temperature, salinity, zonal and meridional velocity, and 2D daily and monthly mean of the Sea surface Height. The model is nested in the Atlantic, within the monthly mean climatological fields computed from the daily output of a $\frac{1}{4}^\circ \times \frac{1}{4}^\circ$ global model from Mercator climatology (www.mercator-ocean.fr). The model is forced by momentum, heat and water fluxes computed by bulk formulae using the 6-h, 0.75° horizontal resolution ECMWF reanalysis fields from the European Centre for Medium-Range Weather Forecast (ECMWF). It implements the data assimilation system OceanVar, a three dimensional variational scheme, developed by Dobricic and Pinardi (2008). The assimilated data include sea level anomaly (SLA) and in situ temperature and salinity profiles. The SLA is assimilated from satellite altimetry along track data. The in situ temperature and salinity profiles belong to different instrumental data types. Data are collected from measurements of CTDs, XBTs, MBTs, bottles and ARGO floats, and are archived in a specific format adapted for assimilation. The reanalysis has been initialized by temperature and salinity monthly climatology calculated from an extensive historical in situ dataset from 1900 to 1987. CMEMS reanalysis was initialized on the 1^{st} of January 1985 and run till 31^{st} of December 2014. Considering two years as the model spin-up time, the dataset is 27 years long.

The Reanalysis is validated trough quality control procedures (QUality Information Document, QUID) that provides a comparison between the dataset variables and Observation, climatology and literature.
The quality of Data is assessed for the entire period computing BIAS and RMSE between the analysis fields and the observations for:

- **Sea Surface Temperature (SST)**
- **Temperature(T)**
- **Salinity(S)**
- **Sea Level Anomaly (SLA)**

The results of the validation are summarized in table 2.1

Parameter	**BIAS**	**RMSE**
SST[$^{\circ}C$]	0.18 ± 0.25	0.56 ± 0.13
T[$^{\circ}C$]	-0.02 ± 0.005	0.34 ± 0.02
S[psu]	-0.01 ± 0.003	0.1 ± 0.01
SLA[cm]	0.09 ± 0.13	3.5 ± 0.55

Table 2.1: RMSE and BIAS computed for different parameter over the entire period of CMEMS reanalysis (1987-2014).

2.3.2 NextData Reanalysis

The NextData_RR 61 years reanalysis uses the 3.2 and 3.4 NEMO-OPA model with the same resolution and domain of the CMEMS reanalysis. The model is nested in the same way of CMEMS in the Atlantic and uses the same Data assimilation scheme. The model is forced by momentum, heat and water fluxes computed by bulk formulae adapted to the Mediterranean case, using AMIP data (Cerchi and Navarra, 2007). The reanalysis has been initialized by monthly climatology fields on the 1^{st} of January 1953 till the 31^{st} of December 2015 with two years of spin-up time. The performance of the reanalysis is evaluated in the same way of CMEMS and the BIAS and RMSE are provided in table 2.2.

Parameter	**BIAS**	**RMSE**
SST[$^{\circ}C$]	0.22 ± 0.30	0.56 ± 0.16
T[$^{\circ}C$]	-0.02 ± 0.004	0.4 ± 0.02
S[psu]	0.01 ± 0.004	0.11 ± 0.01
SLA[cm]	-0.09 ± 0.02	3.76 ± 0.65

Table 2.2: RMSE and BIAS computed for the parameter assessed over the entire period of NextData_RR reanalysis (1955-2015).

2.3.3 C-GLORS reanalysis

The C-GLORS reanalysis is done for the global ocean, including the Mediterranean Sea. The reanalysis shares many features with CMEMS analysis. It runs with NEMO ocean model at eddy-permitting horizontal resolution of $\frac{1}{4}^\circ \times \frac{1}{4}^\circ$ and 50 vertical depth levels and shares the same data assimilation scheme of CMEMS reanalysis (OceanVar). Since C-GLORS is a global reanalysis, NEMO is coupled with a sea-ice model, LIM2 (Louvain-la-NeuveSea Ice Model). C-GLORS is forced by ECMWF ERA-Interim atmospheric reanalysis, using bulk formulas from Larges and Yeager (2004). It is initialized using the 1979-1982 mean January conditions and reanalysis data are provided starting from 1980 till 2015. Figure 2.5 shows an overview of the C-GLORS reanalysis system.

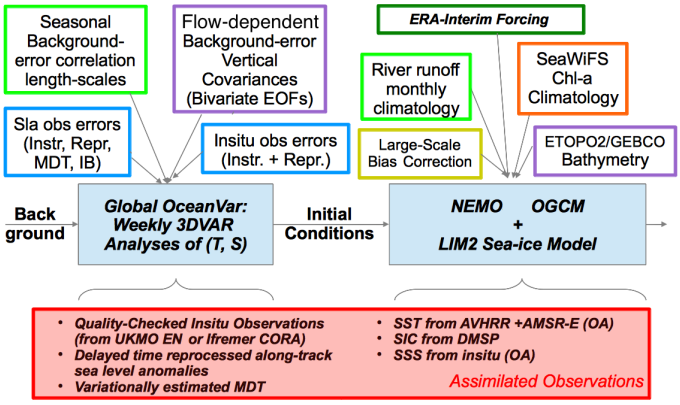

Figure 2.5: Work-flow of the CMCC global ocean reanalysis system (C-GLORS).

Chapter 3

Perpetual year simulations

Perpetual year simulations are carried out using NEMO ocean numerical model implemented in the SURF platform, described in the previous chapter, to study the behaviour of the wind-driven circulation of the Mediterranean sea. The model run with climatological perpetual-monthly mean forcing. A run with this kind of forcing, that last enough time, allow to reproduce the circulation of the Mediterranean Sea in equilibrium with the external forcing. The central idea of these experiments is to observe the response of the Mediterranean Sea circulation when subjected to different wind stress forcing.
First is necessary to find an adequate wind dataset that allow to reproduce a realistic kinetic energy for the whole Mediterranean Sea. Sensitivity experiments are then carried out, changing the parametrization of sub-grid small scale physics and the numerical schemes in order to find better results. Thus, the last series of experiments is performed modifying the wind dataset chosen and the results are analysed and discussed.
The reanalysis dataset, CMEMS, produced by Copernicus Marine Environment Monitoring Service, provide the fields of Temperature and salinity to compute the climatological forcing for the boundary and initial conditions of the model.

3.1 Initial model set up

the ten years simulations are carried out considering no leap years, and month with 30 days each to avoid inhomogeneities in the monthly mean fields computations of the output data. The starting date is chosen arbitrary as the 1^{st} of January 1985. Thus, each simulation run from this day to the 30^{th} of December 1994. The output are 10 days mean data stored in NetCDF files, and the date assigned to each timestep is chosen in the middle of the mean computation interval.

3.1.1 Space domain

the domain of the simulation is the whole Mediterranean basin, with the eastern Atlantic ocean included in the domain (Atlantic box) to better evaluate the influence of the open ocean forcing in a semienclosed basin like the Mediterranean sea. The zonal extension of the horizontal domain is of about $5160\,km$, from $17.5°W$ to $36.125°E$, while the meridional extension is around $1750\,km$ from $30.25°N$ to $45.875°N$. The horizontal resolution is of $\frac{1}{8}^{\circ}$ in both horizontal direction, so an

eddy-permitting regime is defined. In the vertical direction, 50 levels are determined, from the surface to a maximum depth of about $6000\,m$. The thickness of each layer varies from $4\,m$ at the surface to about $480\,m$ at the maximum depth in the Atlantic area. The vertical location of the W- and T-levels are defined from the following coordinate transformation (figure 3.1):

$$z(k) = h_{sur} - h_0 k - h_1 \left[cosh\left(\left(k - h_{th}\right) h_{cr}\right)\right] \tag{3.1}$$

where the coefficients $h_{sur}, h_0, h_1, h_{th}$ and h_{cr} are free parameters to be specified. h_{cr} represents the stretching factor of the grid and h_{th} is approximately the model level at which maximum stretching occurs.

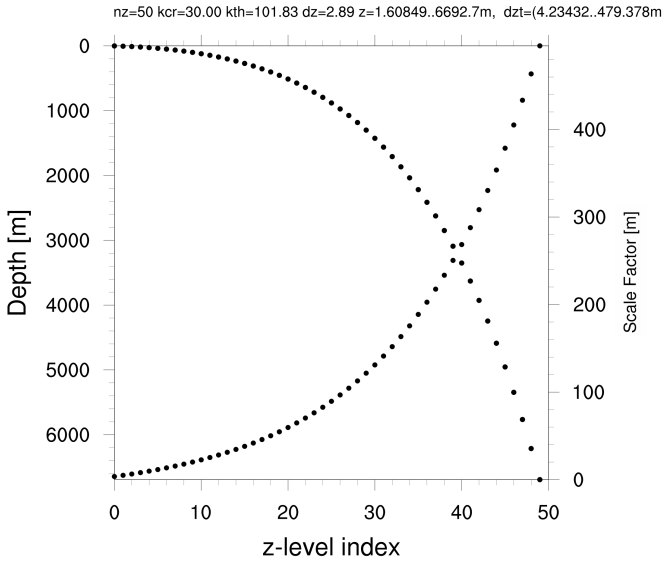

Figure 3.1: Vertical layer distribution for the simulations. Each point represent a vertical grid point. The dotted curve starting from the bottom represent the thickness of each layer (scale factor, right scale). The dotted curve starting from the top represents the depth of each layer (depth, left scale)

Reproducing correctly the bathymetry is an important feature to appropriately simulate the ocean circulation. GEBCO (General Batymetric Chart of the Ocean) chart is used. GEBCO website provide bathymetry charts for almost the whole world ocean at very high resolution of 30-arc second and in different format. SURF perform the interpolation on the domain of interest at the model resolution as shown in figure 3.2. GSSHS provide data for the high resolution coastline.

3.1.2 Boundary conditions

Generally SURF is optimized for short-time run, and it requires daily forcing fields. The code for Pre-processing procedures was modified to allow a better performance with monthly mean forcing. The flux formulation set up is used for NEMO run, so the input forcing fluxes are directly provided as surface boundary conditions. The heat flux for the flux formulation is:

$$Q = Q_0 + \frac{\partial Q}{\partial T}\left(T|_{z=\eta} - SST_{clim,m}\right) \tag{3.2}$$

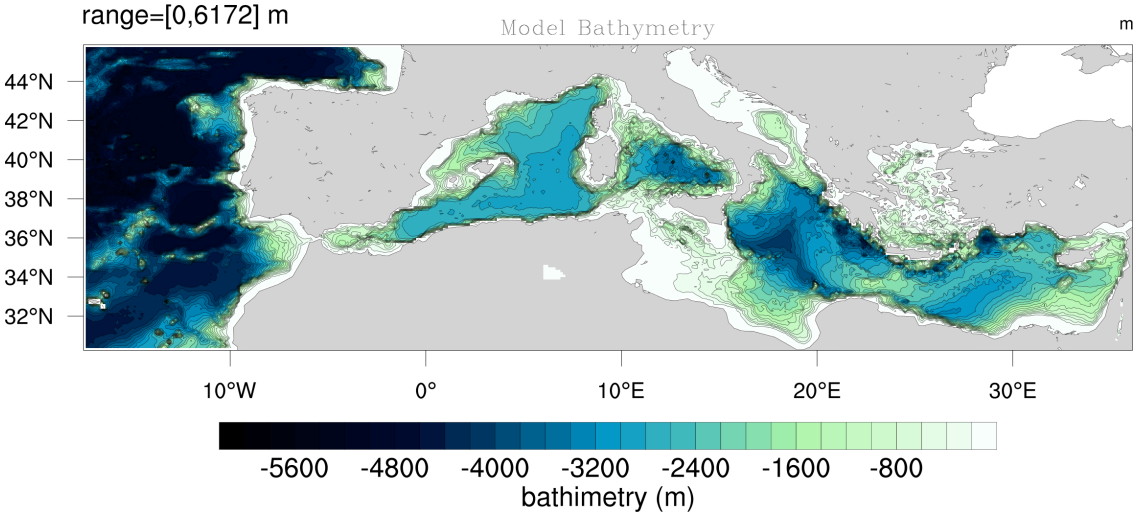

Figure 3.2: Model domain bathymetry interpolated from the GEBCO high resolution bathymetry.

where Q_0, the mean heat budget is imposed equal to zero. T is the surface model temperature and $SST_{clim,m}$ represent the monthly climatological sea surface temperature field. $\frac{dQ}{dT}$ is a negative feedback coefficient, equal to $-80\,W/m^2\,K$, necessary to relax the model temperature to the climatological value. For a given ocean depth, Δz, it is possible to estimate a relaxation time Δt:

$$\frac{dQ/dT}{\rho_0 C_p} = \frac{\Delta z}{\Delta t} \qquad \Delta t = \Delta z \frac{\rho_0 C_p}{dQ/dT} \tag{3.3}$$

Where $C_p = 4000\,J/kgK$ is the specific heat and $\rho_0 = 1020\,kg/m^3$ is the reference density. If $\Delta z = 50\,m$, the thickness of the mixed layer, the relaxation time is $\Delta t \cong 40\,days$. In the freshwater budget is also possible to add a feedback term. It takes the form of a freshwater flux and can be written as:

$$emp = emp_0 + \gamma_s^{-1} e_{3t} \frac{(S|_{z=\eta} - SSS_{clim,m})}{S|_{z=\eta}} \tag{3.4}$$

where emp_0 is the net fresh water flux, imposed equal to zero, e_{3t} the scale factor, *i.e.* the thickness of the layer, S the computed model sea surface salinity, SSS the monthly climatological surface salinity and $\gamma_s = -1630\,m^2 s/K$ a negative feedback coefficient to ensure the relaxation of the model salinity to $SSS_{clim,m}$.
The close boundary are treated with the **no-slip condition**, while in the Atlantic box, open boundary conditions are defined by monthly mean oceanic fields. The bottom friction is not considered. This condition can be written as follows

$$A^{vm}\left(\frac{\partial \mathbf{U}_H}{\partial z}\right)\Big|_{z=-H} = 0 \tag{3.5}$$

3.2 The wind dataset

The discussion in chapter one introduced the problem of the wind driven circulation of the oceans. Indeed, the wind stress applied on the sea surface account for a large portion of the circulation that may be observed in the Mediterranean Sea. The

prevailing wind regimes over the Mediterranean are the ones depicted in chapter one: a strong north-westerly mistral wind regime during winter in the WMED, and a weaker but still strong north-easterly Ethesian wind regime over the EMED during Summer.

3.2.1 From wind data to wind stress

A very sensitive issue is the parametrization of the shear stress that the wind exerts on the sea surface. Apart from the uncertainties that affect the observations of the surface wind field over the ocean, the wind stress is affected by many physical processes as the presence and the shape of the wind waves and the momentum exchanges between ocean and atmosphere (air-sea interactions) that are complicated by the stratification and stability of the atmospheric boundary layer. Usually an empirical formula is used. The wind stress $\boldsymbol{\tau}$ can be defined as:

$$|\boldsymbol{\tau}| = \rho_a C_D \left(u_a^2 + v_a^2\right) \tag{3.6}$$

where $\rho_a = 1.2 \times 10^{-3}\, g\, cm^{-3}$ is the air density, u_a and v_a are the zonal and meridional air velocity measured at $10\, m$ and C_D is the *Drag coefficient* that is of the order of 2×10^{-3}, but can vary with wind speed and other parameters. If the formula (3.6) is widely accepted, the same can not be said for the empirical coefficient C_D. A variety of formulations exists, and choosing the most appropriate can not be always an easy task. To asses the role of wind and stability on $\boldsymbol{\tau}$, the wind stress is computed with a wind speed and stability C_D from Hellermann and Rosenstein (1983). The Drag coefficient depends upon two variables M and ΔT defined as:

$$M = \sqrt{u_a^2 + v_a^2}\,, \qquad \Delta T = T_a - T_s \tag{3.7}$$

where T_a is the air temperature at $2\, m$ and T_s is the sea surface temperature. Thus, the coefficient C_D is defined as a second degree polynomial defined as follow:

$$\begin{aligned} C_D\left(M, \Delta T\right) = 0.934 \times 10^{-3} + 0.788 \times 10^{-4} M + 0.868 \times 10^{-4} \Delta T \\ -0.616 \times 10^{-6} M^2 - 0.120 \times 10^{-5} \left(\Delta T\right)^2 - 0.214 \times 10^{-5} M \left(\Delta T\right) \end{aligned} \tag{3.8}$$

The air temperature is given by the ERA-INTERIM atmosphere reanalysis (Dee et al., 2011), while the SST is provided By Copernicus Marine Service and CNR -ISAC by infra-red satellite radiometry measurements. The fundamental input parameter necessary to compute the wind stress $\boldsymbol{\tau}$ in (3.6) (and C_D in (3.8)) is the wind speed at $10\, m$. In the next section the different wind dataset used to compute the wind stress are discussed in order to evaluate differences and to choice the best dataset for the purpose of this work.

3.2.2 Dataset experiments

There are a multitude of techniques and products providing information and data on the wind speed and direction, each with their advantages and weaknesses. Sensitivity experiments with different wind datasets are listed in table 3.1. In the first column the name of the experiments are listed, while the remaining columns provide informations on the wind datasets. All the wind stress data are obtained from daily wind data applying formulas (3.6) and (3.8) or daily mean is computed from

hourly data and then the wind stress is computed. The only exception is for the CMEMS reanalysis dataset that provided directly the wind stress data computed in slight different way. Indeed, the CMEMS computation of wind stress uses data wind from ERA-interim reanalysis, but to compute the wind stress, it account also for the velocity of the ocean current, while this parameter is not considered in the computation of the wind stress effectuated here.

	Wind dataset			
Run name	**Dataset provided**	**Temporal coverage**	**horizontal resolution**	**Length of integration**
MED_exp_10y_cntr	CMEMS 27-year reanalysis	1987-2014	$\frac{1}{16}^\circ \times \frac{1}{16}^\circ$	10 years
MED_exp_15y	CMEMS 27-year reanalysis	1987-2014	$\frac{1}{16}^\circ \times \frac{1}{16}^\circ$	15 years
MED_exp_10y_nowind	No wind stress	na	na	10 years
MED_exp_10y_ASCAT	ASCAT scatterometer	2013-2015	$\frac{1}{4}^\circ \times \frac{1}{4}^\circ$	10 years
MED_exp_10y_ECMWF	ECMWF analysis	2010-2015	$\frac{1}{8}^\circ \times \frac{1}{8}^\circ$	10 years
MED_exp_10y_ERA_INT	ERA-Interim reanalysis	1987-2013	$0.75^\circ \times 0.75^\circ$	10 years

Table 3.1: Wind dataset sensitivity experiments

From the datasets obtained, a monthly climatology is then built and used as wind forcing. It is important to clarify that as it is indicated in table 3.1, each dataset has its own temporal coverage, with its particular variability, smoothed by the computation of the climatology, but still present and strongly dependent from the lengthiness of the dataset. The aim of this process is to build a climatology that correctly reproduces the prevailing wind regimes observed in the Mediterranean Sea, with low interesting in keep the interannual variability that can be present in a particular time interval.
This set of experiments includes a run where the wind stress is put equal to zero (MED_exp_nowind), so the circulation is governed only by baroclinic processes forced by the temperature and salinity surface forcing and by the open boundary in the Atlantic box. In this set of experiments the reference run is MED_exp_10y_cntr, where CMEMS reanalysis wind forcing is used. CMEMS forcing is also used for another experiments with a longer integration time of 15 years to asses whether 10 years of integration is an adequate time to reach an energetic stability. Run MED_exp_10y_ASCAT uses wind data from the Metop/ASCAT and OSCAT scatterometer measurements. The wind forcing in simulation MED_exp_10y_ECMWF are the wind data analysis from ECMWF. The last experiment listed is MED_exp_10y_ERA_INT and uses wind from ERA-Interim reanalysis. To have some insights in the wind dataset, an integrated basin monthly average of the wind stress and of the curl of the wind stress can be computed for each dataset (figure 3.3). The upper panel shows the typical two wind stress peaks in Winter and Summer. The wind stress

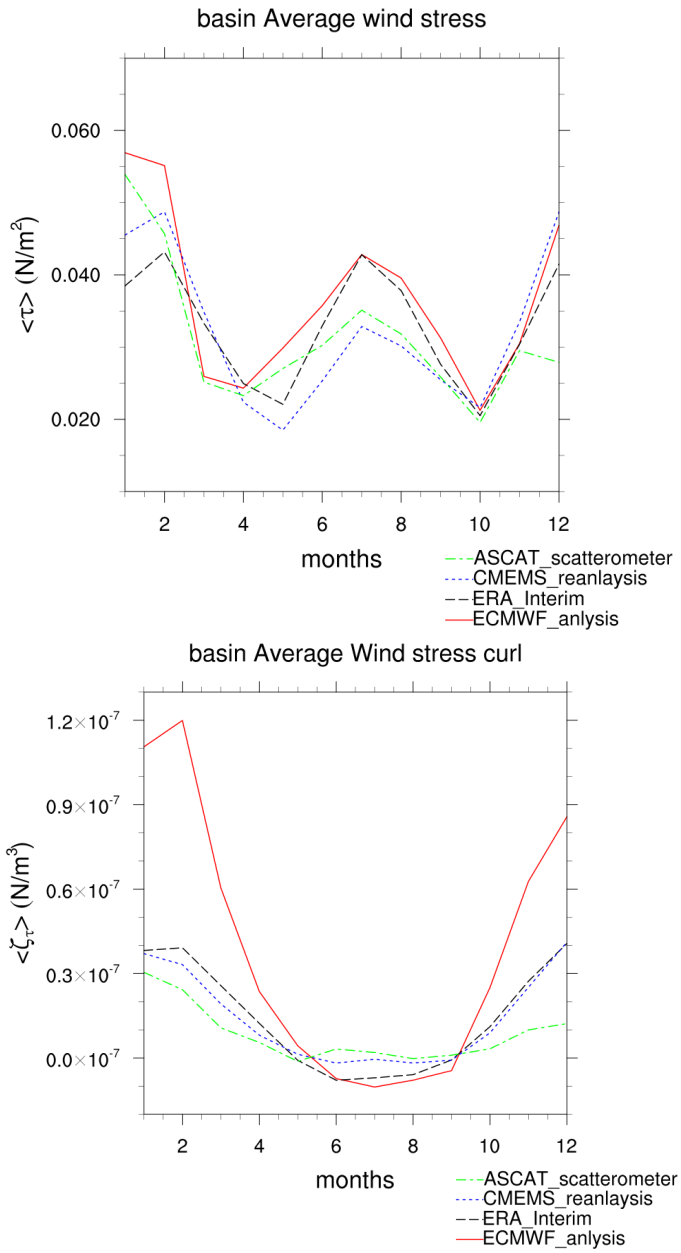

Figure 3.3: basin averaged wind stress and wind stress curl for wind dataset listed in table 3.1.

curl has positive values in Winter, with very high values for ECMWF analysis, and is negative during Summer. The Differences are evident both for wind stress and wind stress curl, even for those datasets that share almost the same temporal coverage. A key factor in determine the amplitude of the wind stress is the resolution of the gridded data. Forcing wind data with coarser resolution in respect of the model horizontal resolution, lack in catching the more energetic processes at the model resolution scale, leading eventually to a low kinetic energy in the model output relative to that forcing. The wind stress curl also is an important parameter to evaluate because it induces the ocean circulation to be cyclonic or anti-cyclonic according to its sign. As a further example, wind stress and wind stress curl maps for February and August are shown for CMEMS reanalysis and for the ECMWF analysis in figure 3.4, 3.5, 3.6 and 3.7.

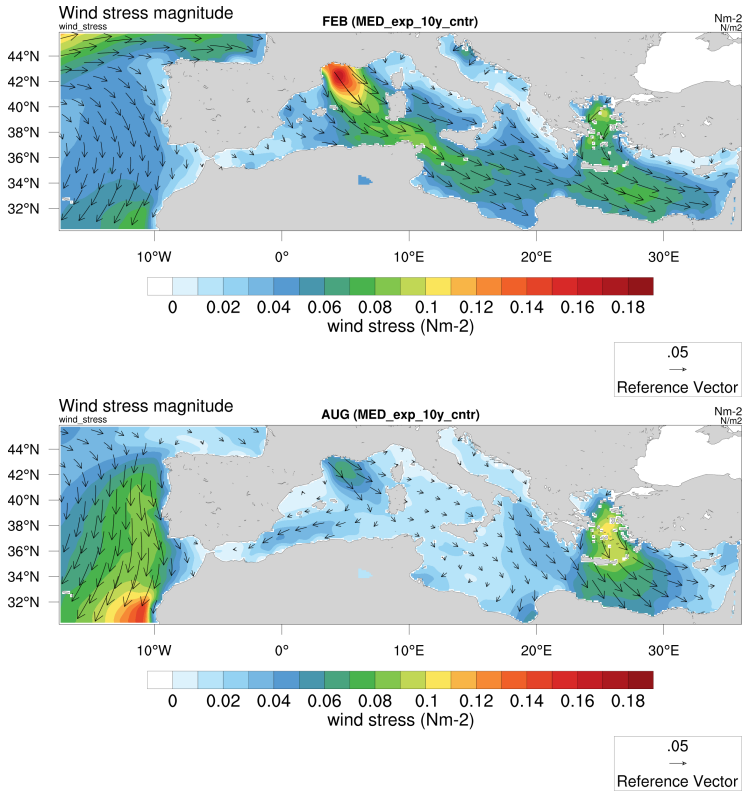

Figure 3.4: Wind stress monthly climatology of February and August computed from CMEMS reanalysis forcing.

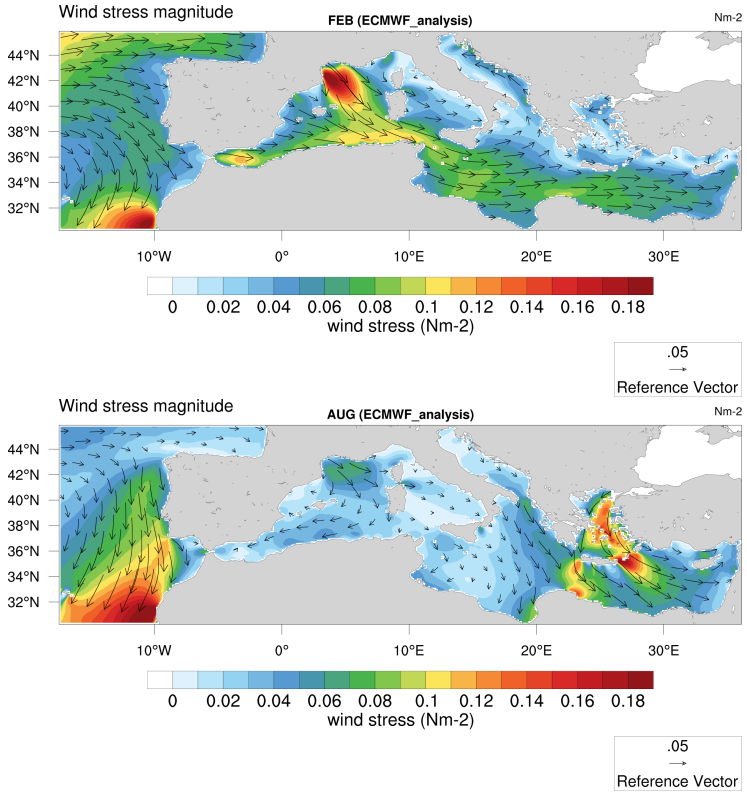

Figure 3.5: Wind stress monthly climatology of February (upper panel) and August (lower panel) from ECMWF analysis.

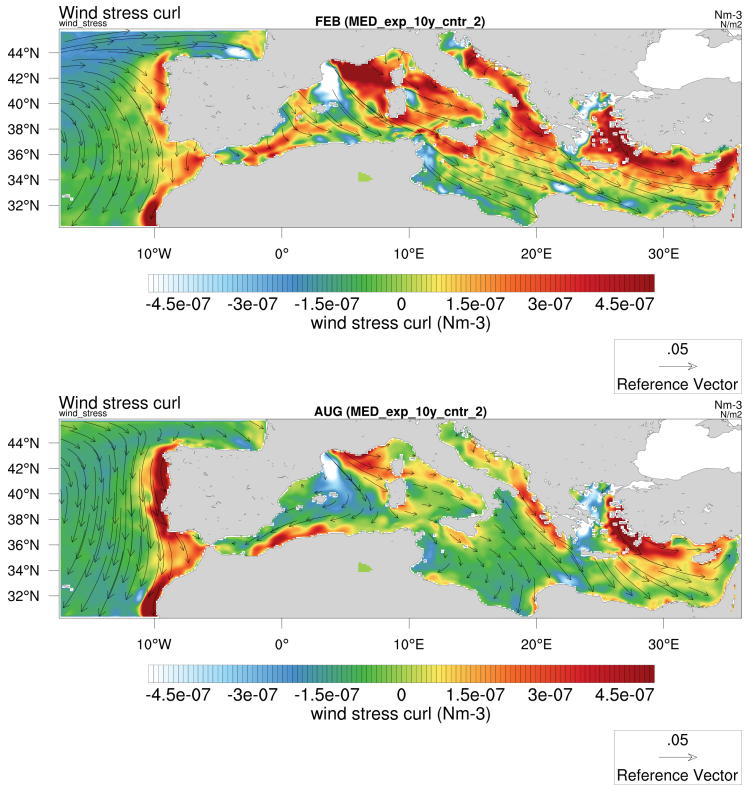

Figure 3.6: Wind stress curl monthly climatology of February (upper panel) and August (lower panel) computed from CMEMS reanalysis forcing.

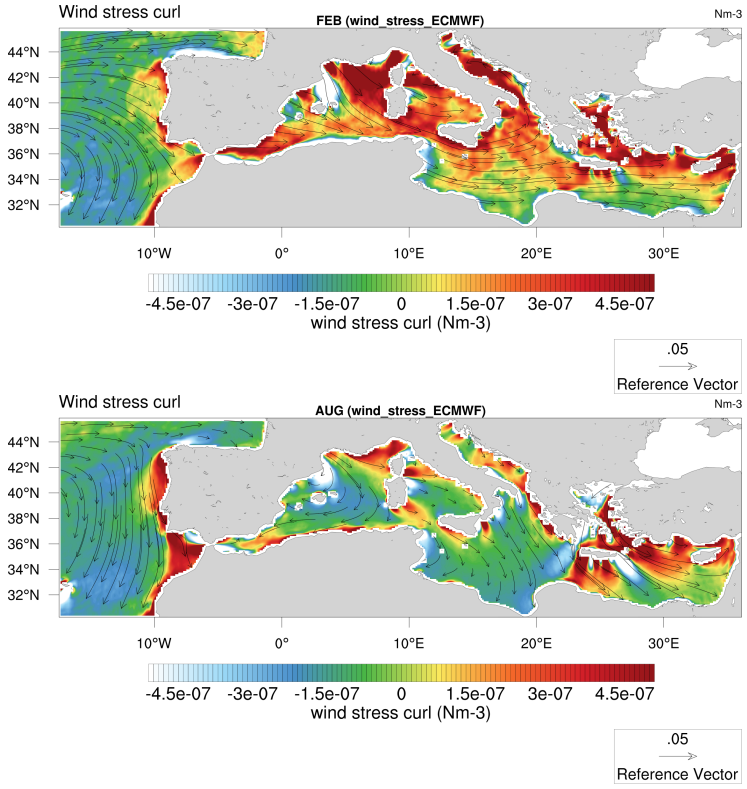

Figure 3.7: Wind stress curl monthly climatology of February (upper panel) and August (lower panel) from ECMWF analysis.

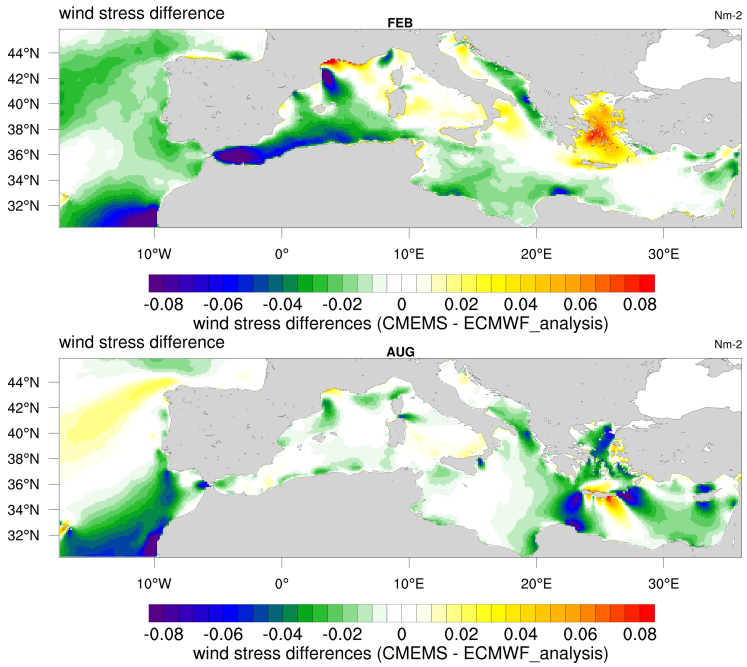

Figure 3.8: Wind stress amplitude differences between CMEMS dataset and ECMWF analysis for February (upper panel) and August (lower panel).

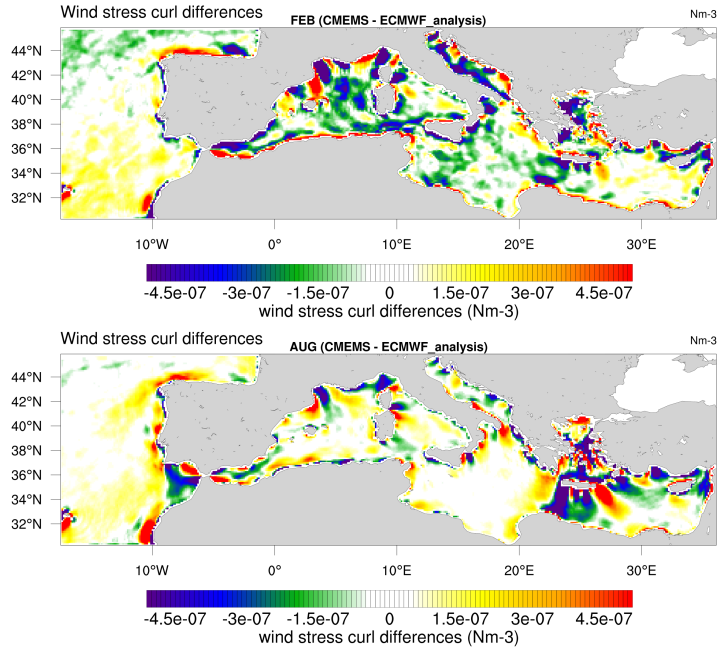

Figure 3.9: Wind stress curl differences between CMEMS dataset and ECMWF analysis for February (upper panel) and August (lower panel).

These figures are representative of the typical wind stress and wind stress curl that can be found in the Mediterranean sea in Winter and Summer. The Mistral induces a nearly zonal wind stress with a maximum in the central WMED in the Gulf of Lions during Winter (upper panels of figures 3.4 and 3.5), while Etesian winds produces a wind stress with a strong northern component and with his maximum in the EMED in the Aegean Sea. The wind stress curl is shown in figures 3.6 and 3.7 with the superimposed wind stress vectors. It shows the typical double gyres

structure with negative values in the northern Mediterranean and positive values in the south (Pinardi and Navarra, 1993). The wind stress curl pattern correctly reflects the circulation observed in the Mediterranean sea, with strong cyclonic gyres in winter, and anticyclonic activity during Summer (Malanotte-Rizzoli and Bergamasco, 1989,1991). It is to note the high seasonal changes of the wind stress curl in the western EMED that contribute to the variability of the circulation in that area. Differences between wind stress and wind stress curl amplitudes of the two datasets for the months of February and August are shown in figure 3.8 and 3.9. ECMWF analysis data show highest values of wind stress amplitude in the WMED during Winter and in the EMED during Summer. CMEMS shows higher values only during Winter in the EMED. As can be expected from 3.3 (lower panel), wind stress curl differences are much more evident during Winter where ECMWF analysis shows an overall high value of positive wind stress curl. In Summer sensible differences can be observed in the EMED. Where CMEMS shows a slightly negative wind stress curl, ECMWF analysis has strong positive values. These contrasting values can be related both to differences in wind stress amplitude and direction between the two datasets. Indeed, the direction of ECMWF wind stress is more zonal than CMEMS, especially during Winter. The discrepancies between the two datasets can be explained in terms of the different horizontal resolution and of the different time interval used to compute the climatological monthly mean fields, 27 years for the CMEMS dataset (1987-2014) and 6 years (2010-2015) for the ECMWF analysis.

Model output

Here the results of this set of simulations are briefly discussed. The basin average kinetic energy (KE) of the horizontal circulation is used as a diagnostic parameter to evaluate the role of the wind forcing in the energetic balance of the Mediterranean circulation and is defined as:

$$KE = \frac{1}{V} \int_V \left(u^2 + v^2\right)\, dV \tag{3.9}$$

In figure 3.10 is plotted the kinetic energy for the experiments of the table 3.1 but is also reported from the literature the kinetic energy of a $\frac{1}{8}^\circ \times \frac{1}{8}^\circ$ horizontal resolution model (MOM model) simulation of the Mediterranean Sea (Tonani, 2003), hereafter TONANI_exp. The TONANI_exp is a perpetual year simulation forced with wind data from ECMWF. The integrated kinetic energy of this experiment oscillates between 7 and 10 cm^2/s^2 and is taken as a reference. The kinetic energy of no-wind experiment rapidly decrease and approximate to zero leading to a very low horizontal circulation. MED_exp_10y_ASCAT and MED_exp_10y_cntr have a similar behaviour, with the former experiment slightly more energetic and with a more pronounced Summer peak. The MED_exp_ERA_INT experiment shows a similar pattern. The energy is too low and the energetic cycle is not properly reproduced. MED_exp_10y_ECMWF appear to be the most energetic forcing and the annual cycle is well reproduced, but the KE is still low compared with TONANI_exp. The ECMWF analysis wind data are then chosen to be the forcing for the central experiments. The KE for MED_exp_15y seems to stabilize after 10 years of integrations, so this time is maintained also for the next simulations.

Figures 3.12 and 3.13 show the mean surface circulation of February and Au-

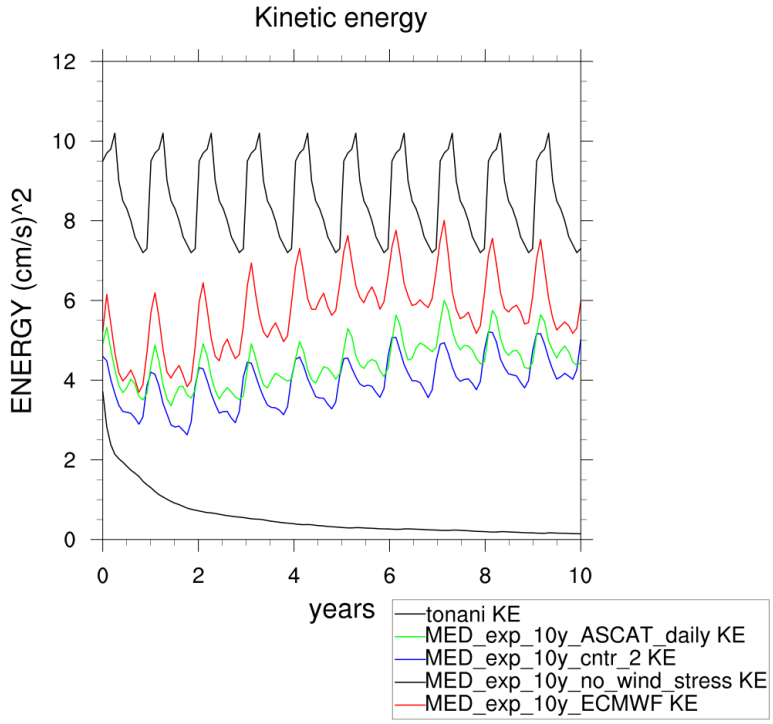

Figure 3.10: basin average kinetic energy for the experiment listed in table 3.1 (MED_exp_15y and MED_exp_10y_ERA_INT are not shown).

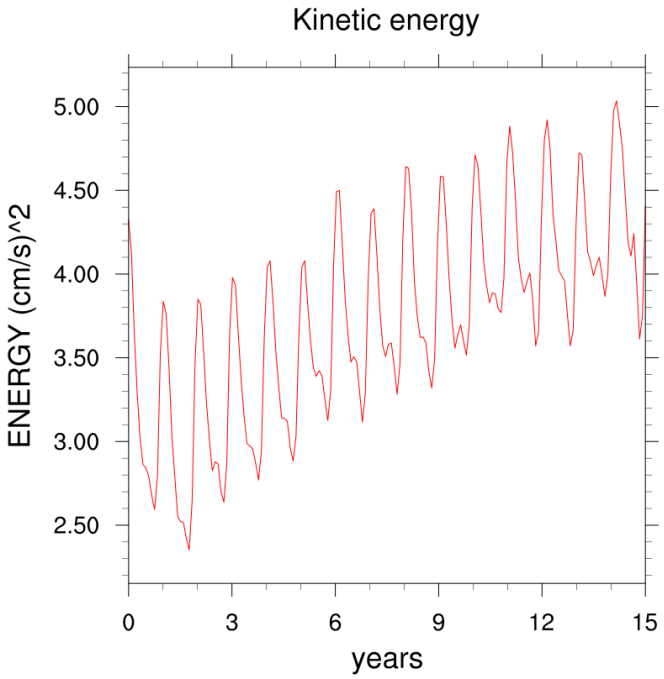

Figure 3.11: Basin average kinetic energy for the experiment MED_exp_15y.

gust for MED_exp_10y_cntr and MED_exp_10y_ECMWF experiments. Differences in the circulation of the simulations are only due to the different wind forcing used. The main circulation features are well reproduced by the two experiments, but MED_exp_10y_ECMWF shows a stronger general circulation both in February and

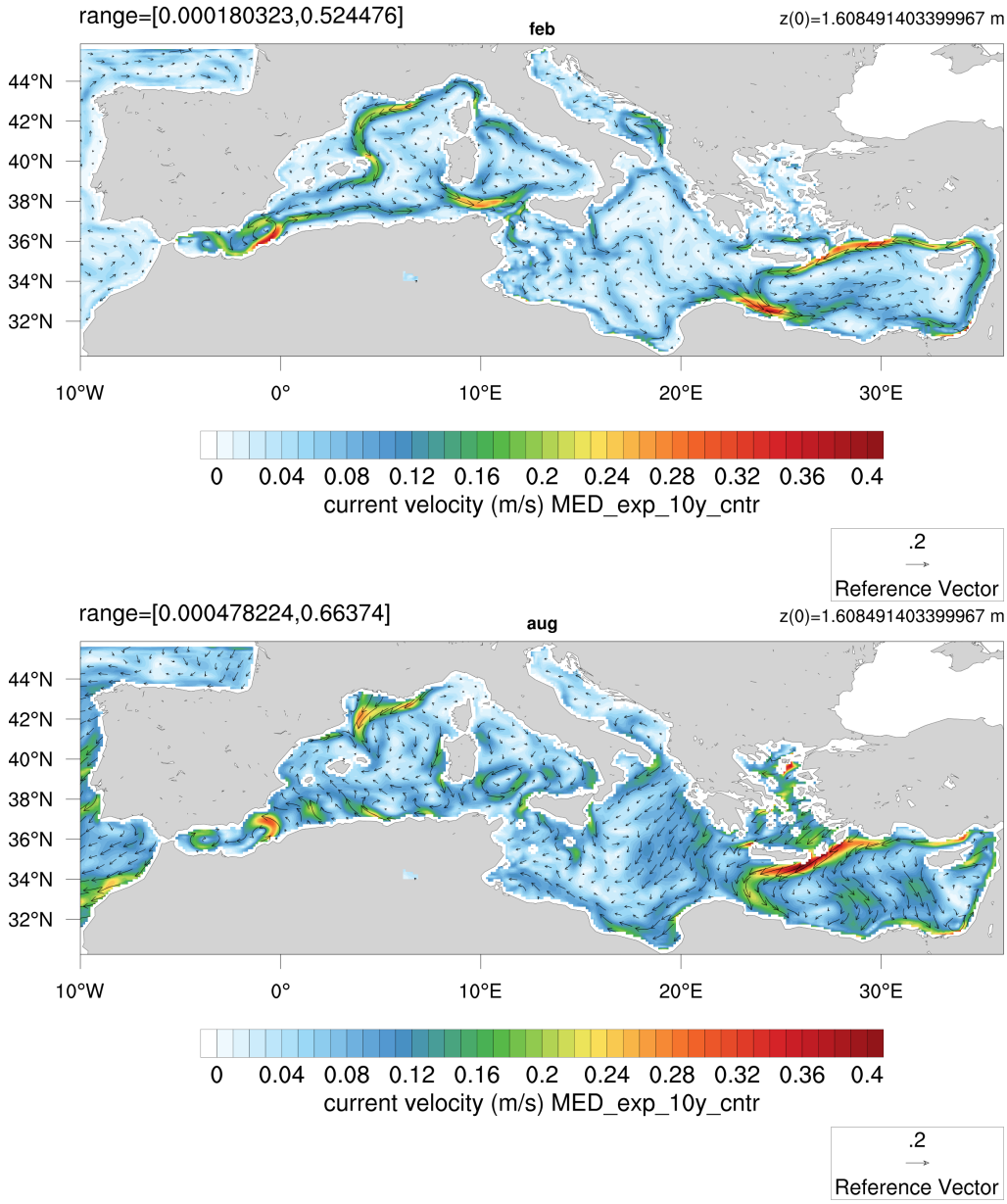

Figure 3.12: Mean Mediterranean circulation for February and August for simulation forced with CMEMS wind stress.

August. In particular in February all the boundary currents are more intense (Algerian current, Asia minor current, Liguro-Provencal-Catalan current (LPCC) and Cretan Passage southern current (CPSC)) in MED_exp_10y_ECMWF. These currents contribute greatly to the kinetic energy of the Mediterranean and can explain the higher values of KE in 3.10, and in turn can be explained by the high value of wind stress. In August the circulation is more chaotic. In MED_exp_10y_ECMWF the circulation shows a stronger anticyclonic activity in the WMED, while in the EMED the signal of the Mersa-Matruh gyre appear to be more evident than in MED_exp_10y_cntr and the boundary current south of Crete is slightly westward shifted.

From the energetic point of view, an important parameter to evaluate is the wind work that the wind stress exert on the sea surface. The wind work, W, can be

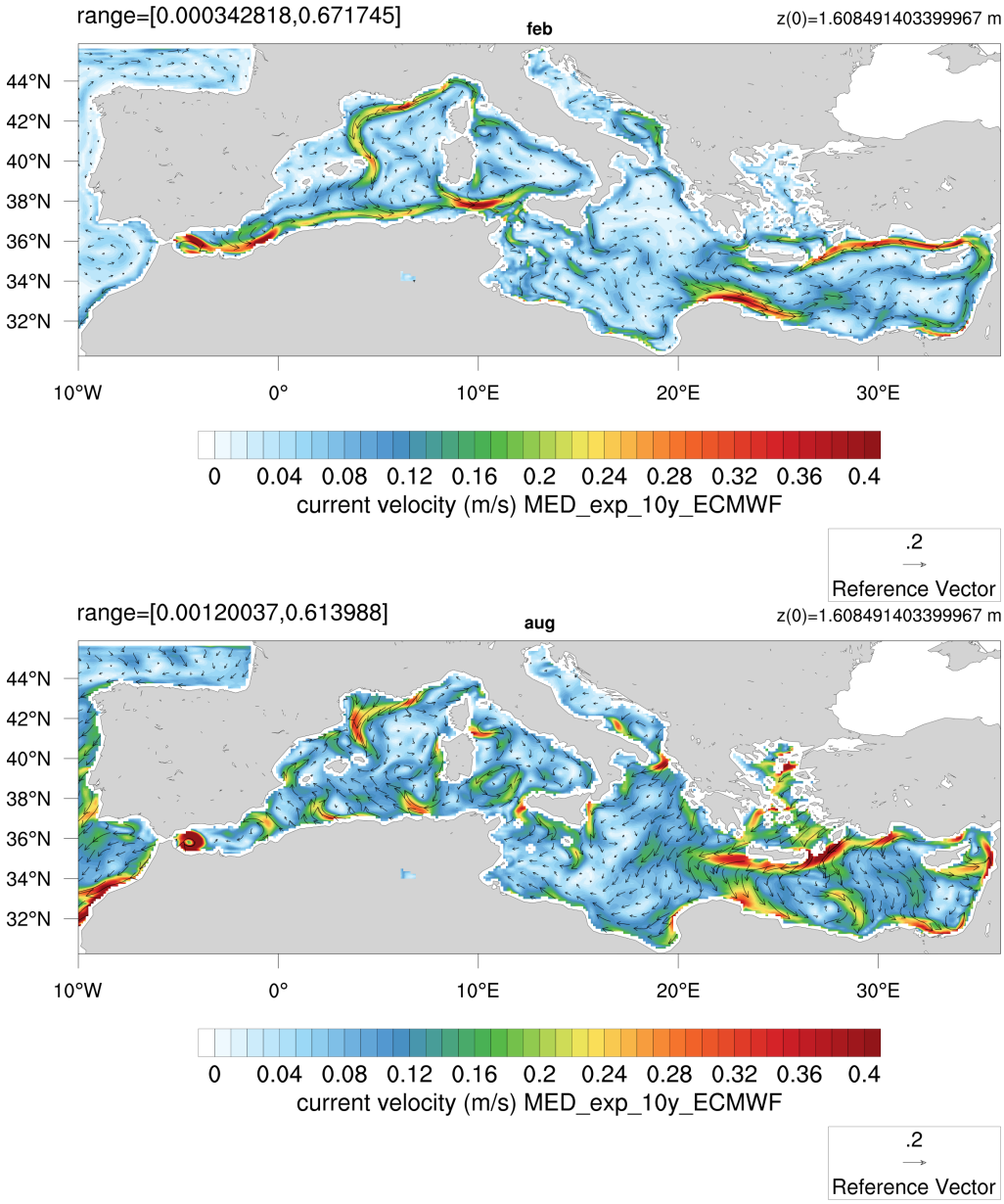

Figure 3.13: Mean Mediterranean circulation for February and August for simulation forced with ECMWF analysis wind data.

computed as:

$$W = \boldsymbol{\tau} \cdot \mathbf{V_s} \tag{3.10}$$

where $\boldsymbol{\tau}$ is the wind stress, $\mathbf{V_s}$ is the surface current velocity and W has units of W/m^2. The wind work allow to specify whether the wind stress act with or against the circulation in a determined area. In figures 3.14 and 3.15 the mean wind work for both experiments is shown. The pattern of wind work for the two simulations is very similar but with higher values (absolute values) for MED_exp_10y_ECMWF. Important gyre structures are highlighted by the wind work amplitude and sign. The western flank of the Gulf of Lion gyre has high positive values of the wind work while the northern part show high negative values. In the EMED remarkable positive values are in the CPSC while wind work is negative in the Asia minor current and in Cretan Sea westward current (CSWC). The wind work shows high

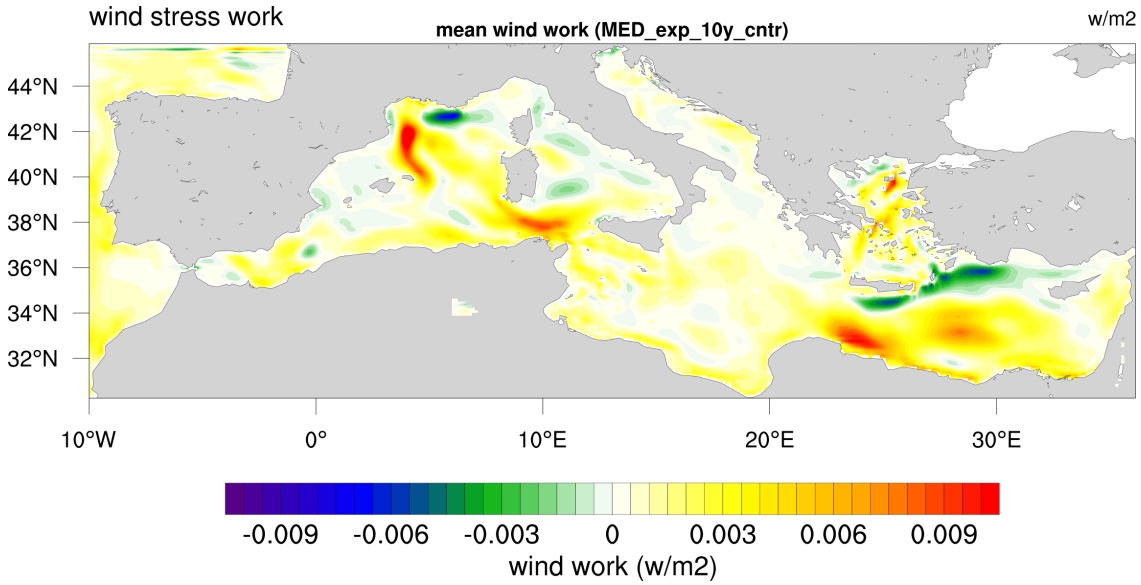

Figure 3.14: Mean wind work in W/m^2 for MED_exp_cntr experiment.

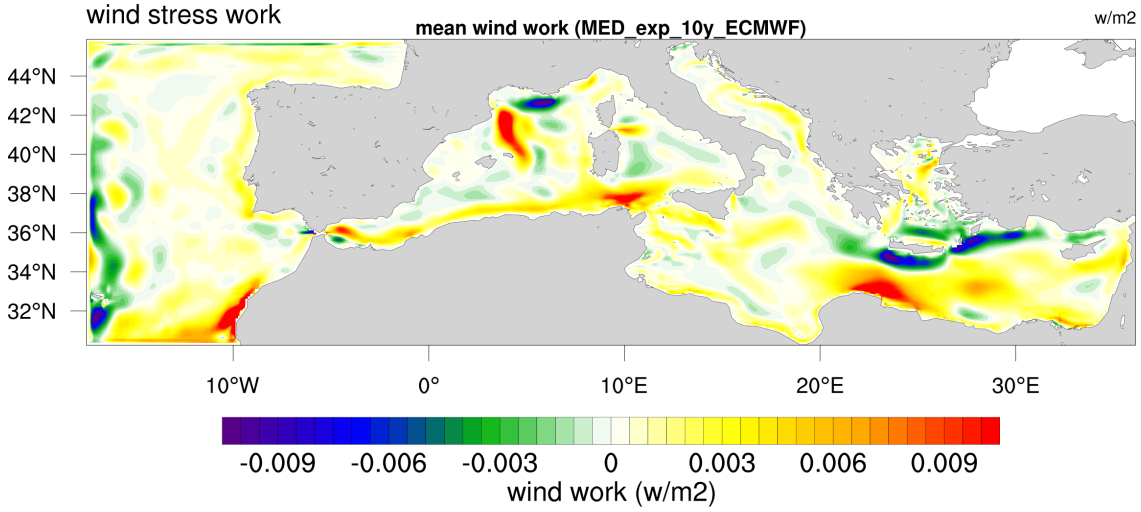

Figure 3.15: Mean wind work in W/m^2 for MED_exp_ECMWF experiment.

values also in the last part of the Algerian current before entering the Sicily strait.

3.3 Model physics sensitivity

In NEMO ocean model many choices are available concerning the numerical schemes used to solve the discretized equations and the physical parametrization implemented to treat the unsolved small scale processes. Sensitivity experiments are then carried out on the vertical physics parametrization, lateral boundary conditions and on the numerics regarding the momentum equations. The characteristics parameter and all the simulations accomplished are listed in table 3.2 with synthetic results in the last column.

In this set of simulations the reference run is MED_exp_10y_ECMWF. In all the numerical experiments the wind forcing is the wind stress computed from ECMWF analysis.

Run name	**Momentum advection scheme**	**Vertical physics**	**Closed boundary conditions**	**Results**
MED_exp_10y_ECMWF	vector form: ENE scheme	PP scheme	no slip	slightly decrease of KE in last years
MED_exp_10y_ECMWF _flux_form	flux form: 2^{nd} order centered scheme	PP scheme	no slip	OK
MED_exp_10y_ECMWF _mix	vector form: MIX scheme	PP scheme	no slip	unstable
MED_exp_10y_ECMWF _tke	vector form: ENE scheme	TKE closure scheme	no slip	Low KE values
MED_exp_10y_ECMWF _ml_PP	vector form: ENE scheme	PP scheme with ML parametrization	no slip	Summer KE peak not reproduced
MED_exp_10y_ECMWF _frslp_vec	vector form: ENE scheme	PP scheme	free slip	OK Highest KE
MED_exp_10y_ECMWF _frslp_flux	flux form: 2^{nd} order centered scheme	PP scheme	free slip	OK
MED_exp_10y_ECMWF _cst	vector form: ENE scheme	Constant coefficients	no slip	circulation not well reproduced

Table 3.2: Sensitivity experiments on model numerical schemes and physics

3.3.1 Numerical scheme

the numeric discretization of the primitive equations can be achieved in different ways. The advection term of the momentum equation is a delicate part to treat. Variations in the numerical scheme changes sensibly the parameter that are better conserved, as the total energy and the total vorticity. The advection term can be generally written in two distinct ways:

- **The vector invariant form**:

$$\mathbf{U} \cdot \nabla \mathbf{U} = \zeta \mathbf{k} \times \mathbf{U} + \frac{1}{2} \nabla \left(\mathbf{U}^2 \right) \tag{3.11}$$

- **The flux form**:

$$\mathbf{U} \cdot \nabla \mathbf{U} = \nabla \cdot \begin{pmatrix} \mathbf{U}u \\ \mathbf{U}v \end{pmatrix} \tag{3.12}$$

where ζ is the relative vorticity, and in the latter equation the vectorial identity $\nabla \cdot (\mathbf{A}\alpha) = \mathbf{A} \cdot \nabla \alpha + \alpha \nabla \cdot \mathbf{A}$ and the fact that $\nabla \cdot \mathbf{U} = 0$ was used. Considering the continuous form of the equations the two formulation are identical, but discretization procedures can lead to substantially different results. The flux formulation form is the more conservative form but it does not adequately conserve the absolute vorticity, and can produces spurious vorticity values. The vector-invariant form has the constraint to conserve the absolute vorticity, but is less effective in conserving the total energy. The vector-invariant formulation allow to choose among four

discretizations of the vorticity term. Without going in further details, an energy and enstrophy conserving scheme is chosen (EEN; Arakawa and Hsu, 1990). A trial with another scheme, a mixed energy and enstrophy scheme (MIX), was done with no positive results. The run MED_exp_10y_ECMWF_mix shows instability after a short integration time. There are two simulations that uses the flux formulation (MED_exp_10y_ECMWF_flux_form and MED_exp_10y_ECMWF_frslp_flux). This form is implemented trough a 2^{nd} order centered finite difference scheme (Madec, 2008).

3.3.2 Vertical physics and lateral boundary conditions

The model resolution is always larger than the scale at which the major sources of vertical turbulence occurs. Thus, turbulent motion is never solved explicitly and the small scale processes has to be parametrized. The vertical turbulent fluxes are assumed to depend linearly on the gradients of large-scale quantities:

$$\begin{aligned} \overline{w'u'} &= -A^{vm}\frac{\partial u}{\partial z}, \quad \overline{w'v'} = -A^{vm}\frac{\partial v}{\partial z}, \\ \overline{w'T'} &= -A^{vT}\frac{\partial T}{\partial z}, \quad \overline{w'S'} = -A^{vT}\frac{\partial S}{\partial z} \end{aligned} \tag{3.13}$$

where the primed variables are perturbations and A^{vm}, A^{vT} are the vertical eddy viscosity and eddy diffusivity coefficients. Thus, the operators D^{vU}, D^{vT} and D^{vS} can be defined in order to account for the turbulent process in the momentum and tracer equations.

$$D^{vU} = \frac{\partial}{\partial z}\left(A^{vm}\frac{\partial \mathbf{U}_h}{\partial z}\right), \qquad D^{vT} = \frac{\partial}{\partial z}\left(A^{vT}\frac{\partial T}{\partial z}\right), \qquad D^{vS} = \frac{\partial}{\partial z}\left(A^{vT}\frac{\partial S}{\partial z}\right)$$

All the vertical physics is embedded in the specification of the eddy coefficients. They can be assumed to be constant or function of the local fluid properties or computed from a turbulent closure model.

Constant eddy coefficients

In MED_exp_10y_ECMWF_cst the eddy coefficients are simply maintained constant in all the spatial domain and equal to:

$$A^{vm} = 1.5 \times 10^{-4}\, m^2/s \qquad A^{vT} = 3 \times 10^{-5}\, m^2/s \tag{3.14}$$

Richardson dependent eddy coefficients

The control run implements the Richardson number dependent eddy coefficients (Pacanowski and Philander, 1981; PP scheme in table 3.2). The hypothesis of a mixing mainly maintained by the growth of Kelvin-Helmotz like instabilities lead to a dependency of the eddy vertical coefficients on the local Richardson number, Ri, that is a measure of the local stratification of the ocean. These quantities are defined as:

$$Ri = \frac{N^2}{\left(\frac{\partial \mathbf{U}_h}{\partial z}\right)^2}, \qquad A^{vm} = \frac{A^{vm}_{max}}{(1+aRi)^n} + A^{vm}_b, \quad A^{vT} = \frac{A^{vT}_{max}}{(1+aRi)} + A^{vT}_b,$$

$$A^{vm}_b = 1.5 \times 10^{-4}\, m^2/s, \quad A^{vT}_b = 3 \times 10^{-5}\, m^2/s$$

where $N^2 = -\frac{g}{\rho}\frac{\partial \rho}{\partial z}$ is the local Brunt-Vaisälä frequency and A_b^{vm} and A_b^{vT} are the background values of the coefficients, A_{max}^{vm} and A_{max}^{vT} are the maximum values that can be reached in case of instability ($Ri \leq 0$), and $a = 5$ and $n = 2$ are constant values. The PP scheme is adopted for most of the simulations except MED_exp_10y_ECMWF_tke, MED_exp_10y_ECMWF_ml_PP and MED_exp_10y_ECMWF_cst.

Mixed layer parametrization

The MED_exp_10y_ECMWF_ml_PP rather than using another scheme, add a Mixed-layer parametrization (ML) to the PP scheme. The ML parametrizes the vertical transfer and the dissipation of the atmospheric forcing. The local depth of the turbulent wind-mixing, the "Ekman depth", $h_e(x, y, t)$ is evaluated, and the vertical eddy coefficients prescribed within this layer. The Ekman depth is defined as:

$$h_e = Ek\frac{u^*}{f_0} \tag{3.15}$$

Where Ek is an empirical parameter and u^* is the friction velocity defined by:

$$u^* = \sqrt{\frac{|\boldsymbol{\tau}|}{\rho_0}} \tag{3.16}$$

TKE closure scheme

The MED_exp_10y_ECMWF_tke experiment uses a "one-and-a-half order" turbulent kinetic energy (TKE) closure scheme to compute vertical viscosity and diffusivity coefficients (Bougeault and Lacarrere, 1989). It is based on a closure assumption of the turbulent length scale, and solve a prognostic equation for TKE, e, that with the help of (3.13) can be written:

$$\frac{\partial e}{\partial t} = \frac{\partial}{\partial z}\left(K_m\frac{\partial e}{\partial z}\right) - K_m\left[\left(\frac{\partial u}{\partial z}\right)^2 + \left(\frac{\partial v}{\partial z}\right)^2\right] - K_\rho N^2 - \epsilon \tag{3.17}$$

where K_m and K_ρ are the eddy viscosity and diffusivity coefficients and ϵ is the dissipation of TKE by molecular processes and are defined as:

$$\begin{aligned} K_m &= C_k l_k \sqrt{e}, \quad K_\rho = K_m/P_{rt} \\ \epsilon &= C_\epsilon e^{3/2}/l_\epsilon \end{aligned} \tag{3.18}$$

$C_k = 0.1$ and $C_\epsilon = \sqrt{2}/2$ are constant values, P_{rt} is the Prandtl number and l_ϵ and l_k are the dissipation and mixing length scale.

Closed lateral boundary conditions

In simulation MED_exp_10y_ECMWF_frslp_vec and MED_exp_10y_ECMWF_frslp_flux the **free slip lateral boundary conditions** are used. This condition implies the tangential velocity at the coastline to be equal to the offshore current velocity. This condition is used with the aim to increase the integrated KE that is heavily influenced by the boundary currents and was low in the previous set of experiments.

3.3.3 Model output diagnostic

Among the simulations realized only MED_exp_10y_ECMWF_mix was unstable. The KE of all the other run listed in table 3.1 is shown in figure 3.16. Both

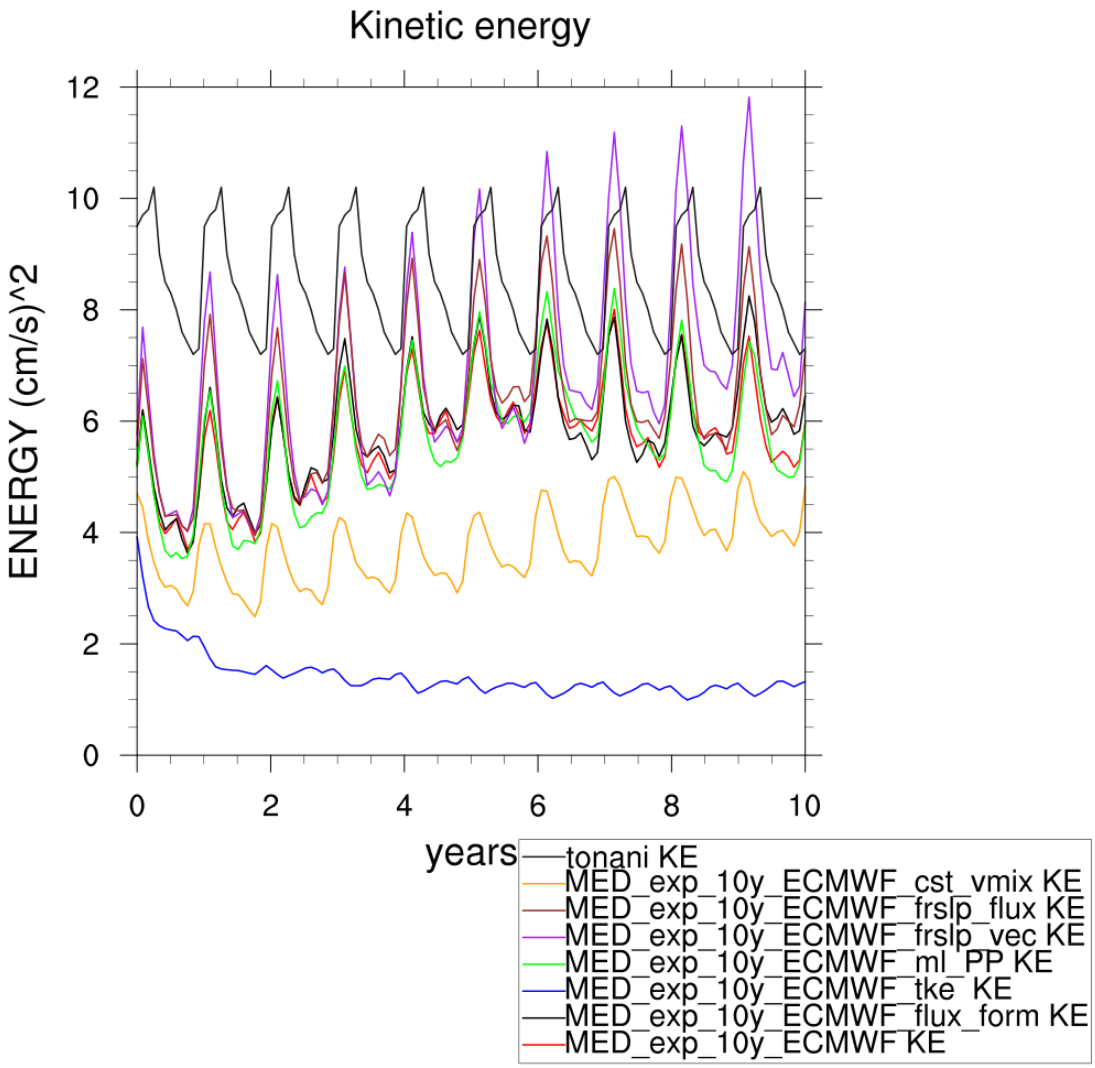

Figure 3.16: KE for the Physics sensitivity simulations.

MED_exp_10y_ECMWF_tke and MED_exp_10y_ECMWF_cst_vmix have low KE. The former run does not reproduce correctly the seasonal energetic cycle. MED_exp_10y_ECMWF_cst_vmix can reproduce the principal features of the Mediterranean circulation, but many details are lost (not shown). The choice of the vertical physics parametrization is a delicate question and may substantially change the results of the simulations. The MED_exp_10y_ECMWF_ml_PP does not reproduce the Summer peak of the KE and slightly enhance the Winter peak of KE. Maintain the PP scheme for the central experiments seems to be the most appropriate choice. Constant values of the eddy coefficients is not recommended and is not realistic, while the fail of the TKE scheme may be connected to the values of the characteristics parameter of the TKE scheme that have to be accurately choose for every specific problems trough sensitivity experiments, that were not carried out in this

work.
The MED_exp_10y_ECMWF_flux_form show a similar behaviour to the control run MED_exp_10y_ECMWF except in the last years where the former run has high values of KE. The free slip closed boundary conditions experiments show the highest values of KE, with MED_exp_10y_ECMWF_frslp_vec reaching the highest value up to about $12\,cm^2/s^2$. It is not straightforward to know which choice of the closed boundary conditions is the more accurate. In this work the choice is based on energetic considerations. It is important to have a KE comparable to the reference value, to reproduce accurately the Mediterranean circulation, so for the last set of experiments, MED_exp_10y_ECMWF_frslp_vec is used as control run.

3.4 Wind forcing sensitivity

To have further insight on the role of the wind stress in the Mediterranean circulation a last set of simulations is performed. The chosen wind dataset from ECMWF analysis is used and modified, and the response of the Mediterranean circulation, in particular the upper circulation, is discussed. The experiments performed are listed in table 3.3.

All the simulations have the same physical and numerical set up as the control run, but differ in the wind forcing. MED_exp_10y_ECMWF_frslp_vec_feb and MED_exp_10y_ECMWF_frslp_vec_aug uses the wind stress of February and August respectively, throughout all the integration time but with the monthly mean thermal and salinity surface boundary conditions that varies normally.
MED_exp_10y_ECMWF_frslp_vec_atl is forced only on the Atlantic box to evidence the remote response of the Mediterranean Sea to the Atlantic circulation. As the set up of the model changed in respect to the initial runs, another simulation with no

Run name	**Dynamical configuration**	**Comments**
MED_exp_10y_ ECMWF_frslp_vec	Monthly mean wind forcing	Control run
MED_exp_10y_ ECMWF_frslp_vec_feb	February wind forcing	Winter typical conditions
MED_exp_10y_ ECMWF_frslp_vec_aug	August wind forcing	Summer typical conditions
MED_exp_10y_ ECMWF_frslp_vec_atl	Wind forcing on the Atlantic box	Response of the Mediterranean Sea to remote forcing
MED_exp_10y_ no_wind_stress	No wind forcing	Internal Mediterranean dynamics
MED_exp_10y_ECMWF _frslp_vec_EOF_1	Idealized wind forcing 1	Wind stress field built from the 1^{st} EOF
MED_exp_10y_ECMWF _frslp_vec_EOF_2	Idealized wind forcing 2	Wind stress field built from the 1^{st} and 2^{nd} EOFs

Table 3.3: Wind sensitivity experiments

wind stress is performed with the new conditions. The last two experiments in table 3.3 are carried out with an idealized wind built from the first EOFs components of the wind stress field.

3.4.1 The idealized wind stress

The *empirical orthogonal functions* analysis (EOF) is a useful tool widely used in atmosphere and ocean science. It can be used to study the variability of ocean and atmosphere variables. EOFs analysis consists in a decomposition of a signal or a data set in term of orthogonal basis functions which are determined from the data. This new set of variables, the EOFs, are completely independent of each other, *i.e.* orthogonal, and are ordered so that the first *few* retain the most of the variations present in all of the original variables. Typically, EOFs are found computing the eigenvalues and eigenvectors of the covariance matrix of an anomaly field. The derived eigenvalues provide a measure of the percent variance explained by each mode. The time series of the amplitude associated with each eigenvalue of an EOF (*aka*, principle components) are determined projecting the derived eigenvectors onto the anomalies field,*i.e* calculating the dot product between EOF spatial patterns and data. The EOF analysis is performed on the monthly mean wind stress fields.

Before to try any physical interpretation of the results obtained, it is to point

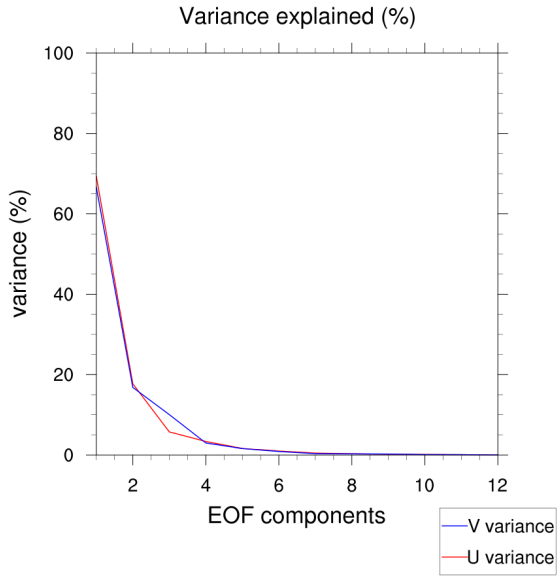

Figure 3.17: The variance explained by each EOF in %.

out that EOF analysis is strictly a mathematical operation, and is not based upon physics. Furthermore, the results may produce patterns that are similar to physical modes within the system. However, physical meaning is dependent on the interpretation given to the mathematical results.

The figure 3.17 shows the variance explained by each EOF component. Both zonal and meridional 1^{st} EOF components explain almost the 70 % of the variance of the wind stress. The 2^{nd} components explain about the 15 % of the variance. In the following pictures 3.18 and 3.19 the spatial patterns and the PC for the first two EOFs are shown. The 1^{st} EOF of the zonal component has

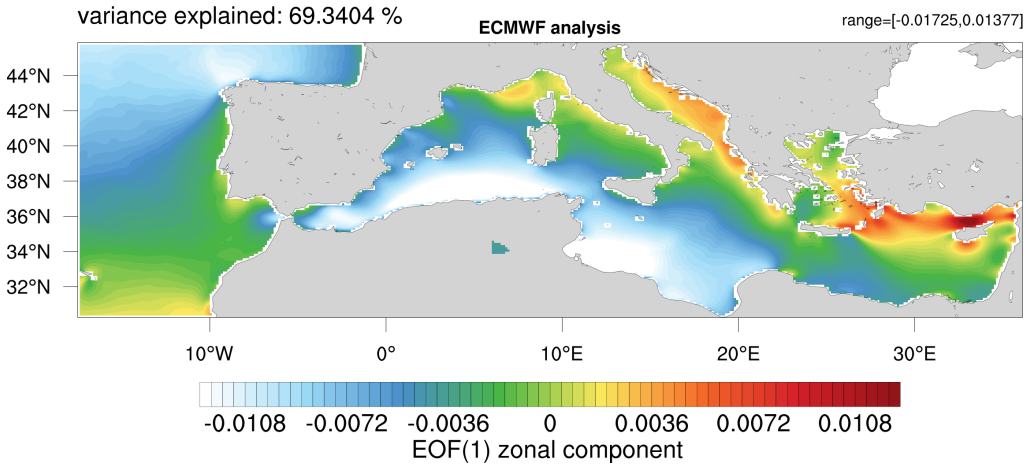

(a) The 1^{st} EOF component of the zonal wind stress

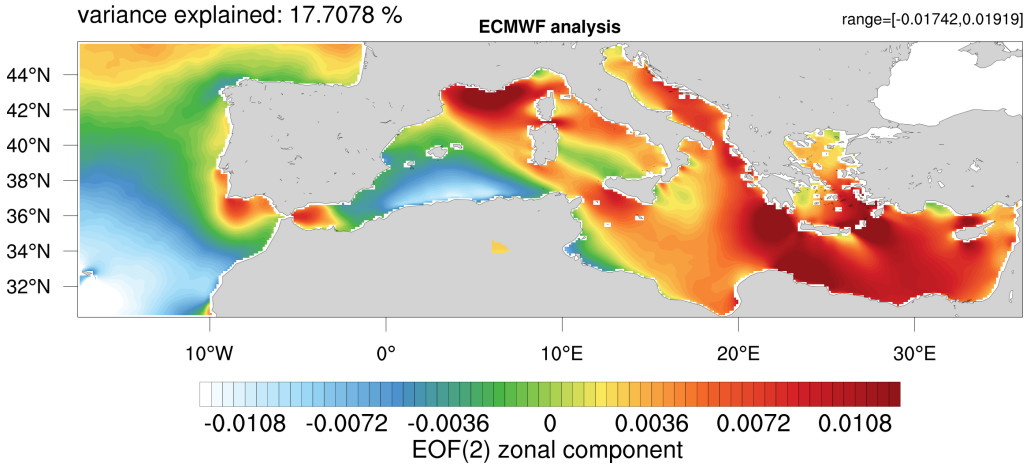

(b) The 2^{nd} EOF component of the zonal wind stress

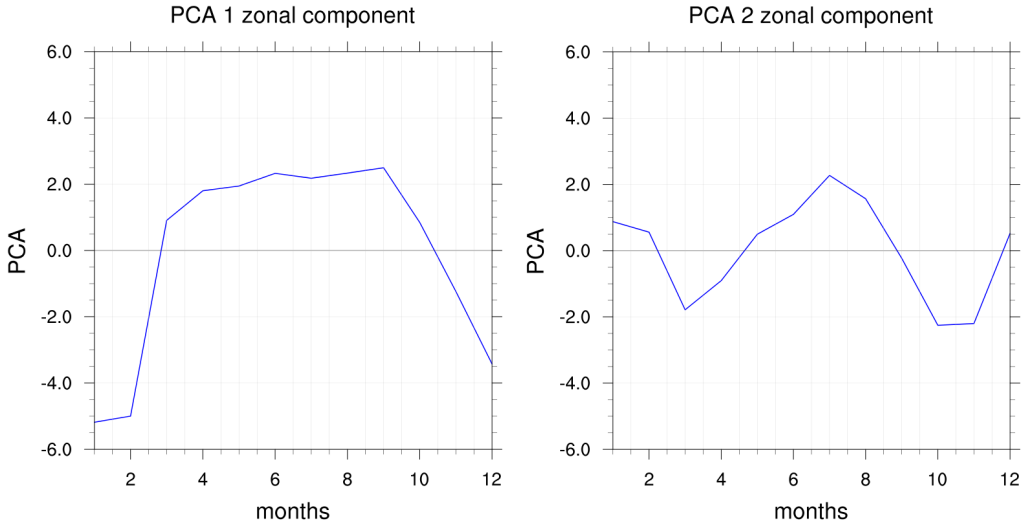

(c) The 1^{st} PC of the zonal wind stress

(d) The 2^{nd} PC of the zonal wind stress

Figure 3.18: EOF components and PCs for the zonal component of the wind stress

a strong north-south gradient, while in the 2^{nd} EOF the same gradient occurs but more shifted westward. The meridional component of both 1^{st} and 2^{nd} EOF

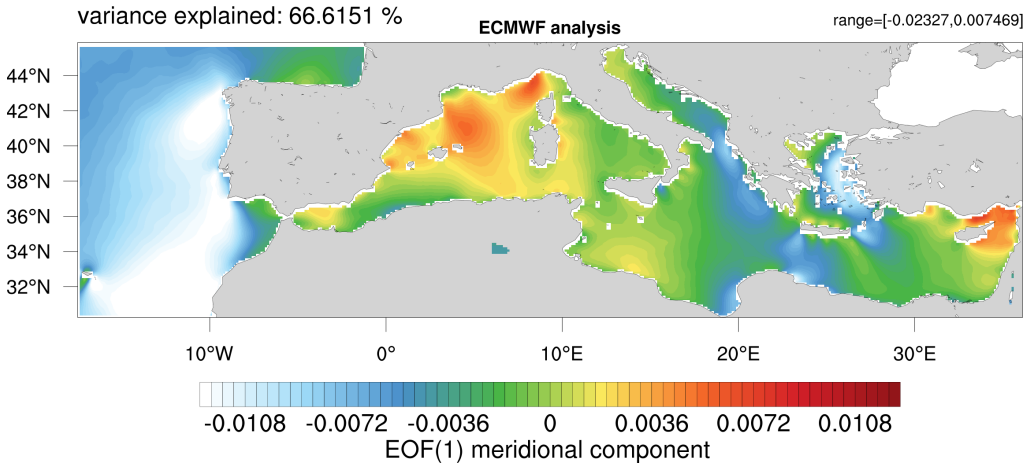

(a) The 1^{st} EOF component of the meridional wind stress

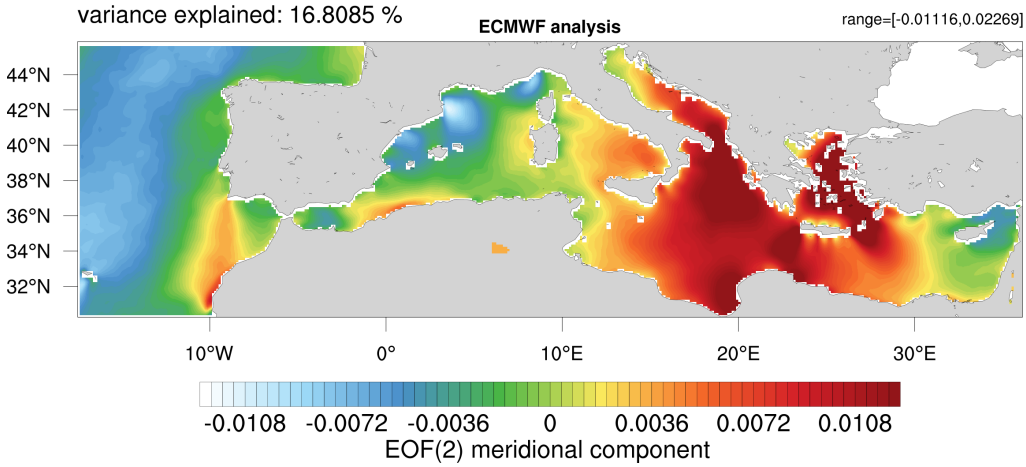

(b) The 2^{nd} EOF component of the meridional wind stress

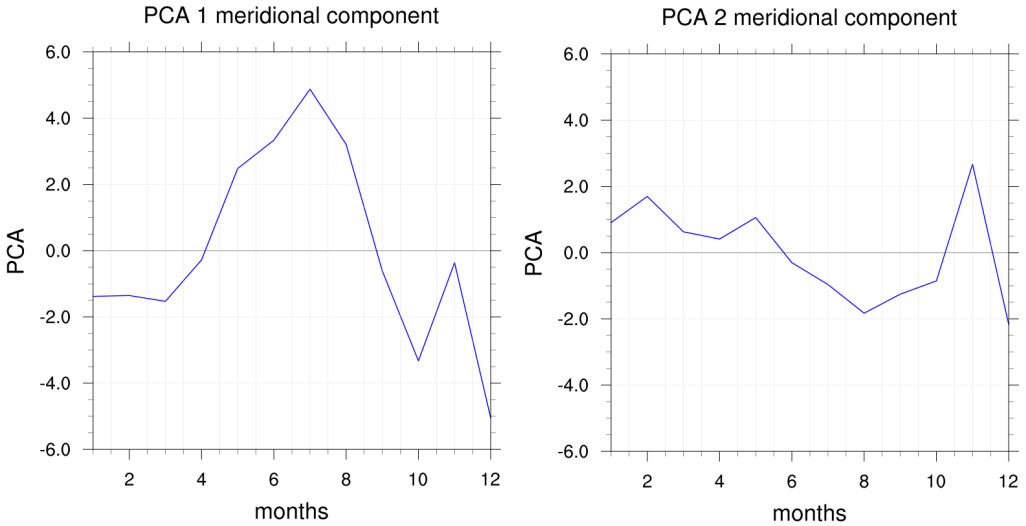

(c) The 1^{st} PC of the meridional wind stress (d) The 2^{nd} PC of the meridional wind stress

Figure 3.19: EOF components and PCs for the meridional component of the wind stress

has an east-west gradient. The PC may give some insights on the physical interpretation of the EOFs. The 1^{st} PC of both u and v components, seems con-

nected to the annual cycle of the wind stress as it shows a period of about twelve months. The 2^{nd} PC shows an intra-annual variability with a period around the 6 months, more defined for the zonal component, and may be related to intra-seasonal variability of the wind stress field. MED_exp_10y_ECMWF_frslp_vec_EOF_1 and MED_exp_10y_ECMWF_frslp_vec_EOF_2 uses both the wind stress reconstruction based on the EOF analysis. The former uses the wind stress rebuilt with the 1^{st} EOF of zonal and meridional components (hereafter EOF_1), while the latter adopt the wind stress reconstruction where both the 1^{st} and the 2^{nd} EOF were used (EOF_2). The 2^{nd} EOF appear to have a sensible role in the intensity of the Summer wind stress conditions and affect also the direction of the wind stress. EOF_1 has weaker but more zonal wind stress during Summer while in winter, especially in the EMED, the direction turn southward in the Levantine Sea and remain zonal in the Ionian Sea. figure 3.20 shows the wind stress rebuilt for the month of August of both EOF_1 and EOF_2. Differences between the two pictures are evident in the EMED. The Etesian winds regime is weaker for EOF_1.

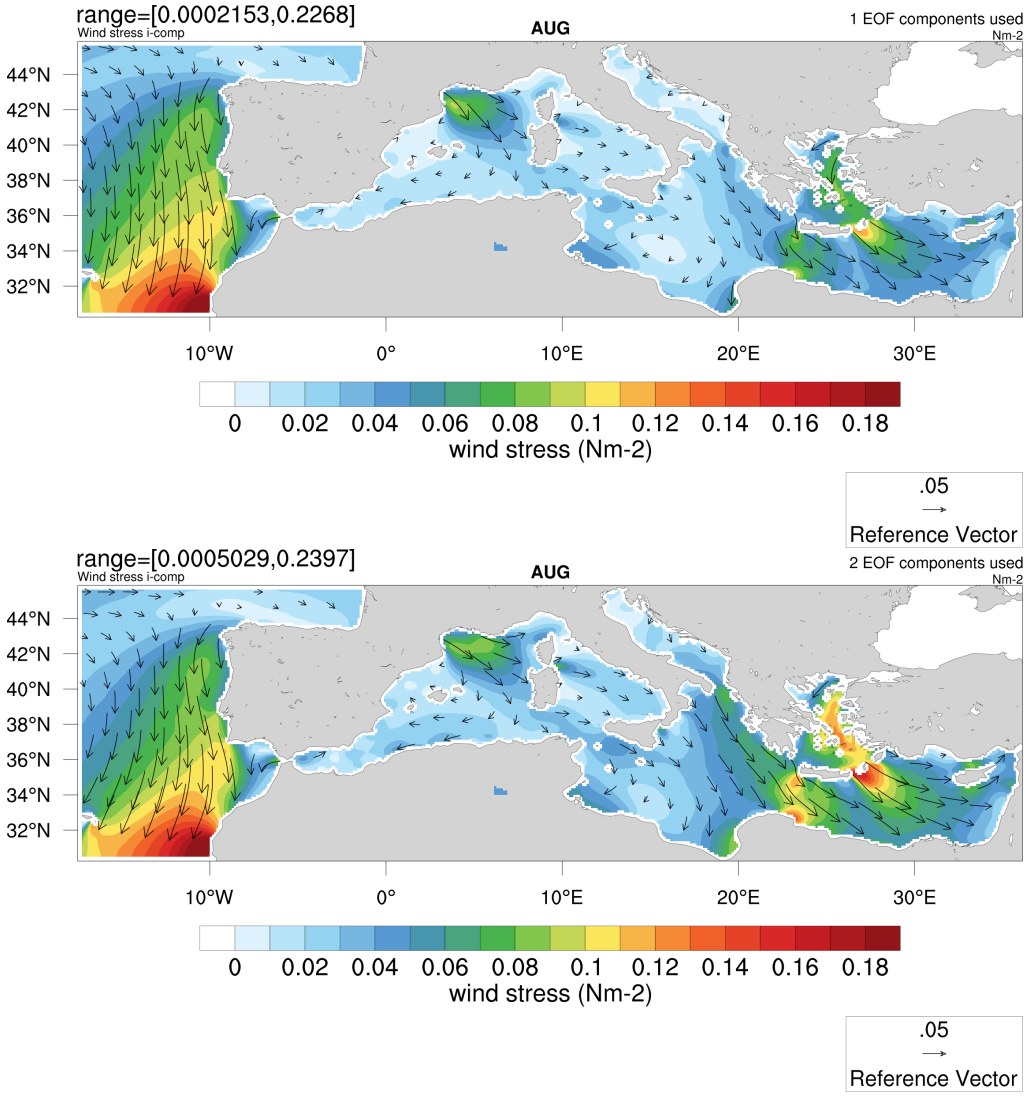

Figure 3.20: August wind stress rebuilt from the 1^{st} EOF component (upper panel) and from the 1^{st} and the 2^{nd} EOF (lower panel).

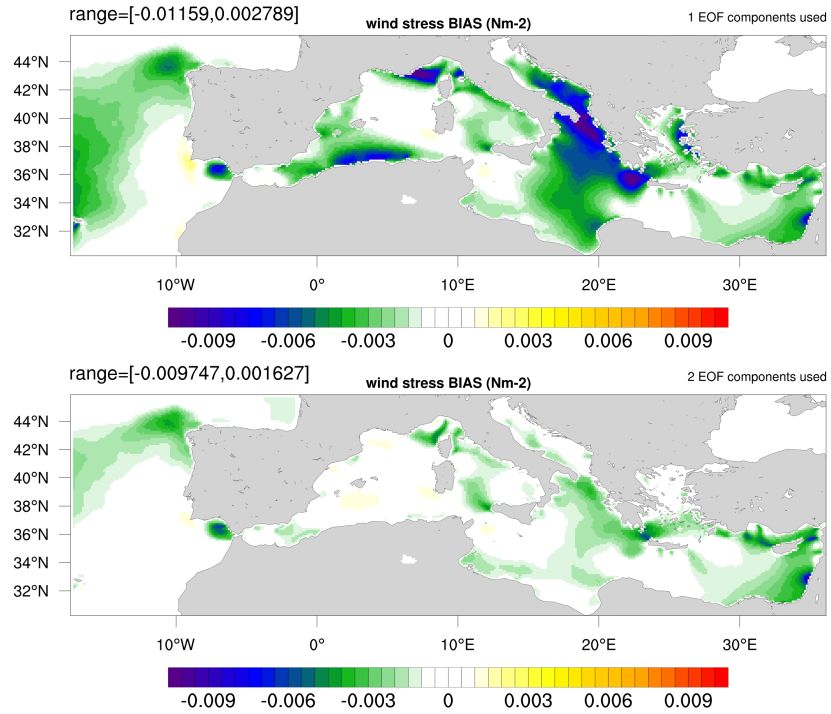

Figure 3.21: Bias computed between the original ECMWF dataset and the two reconstruction of the wind stress based on EOF analysis.

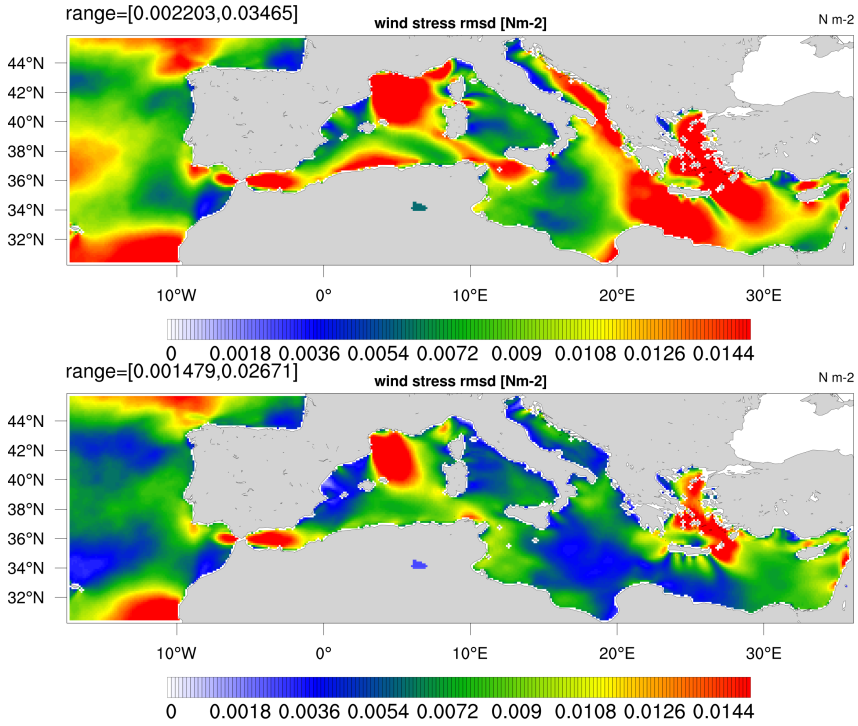

Figure 3.22: RMSD computed between the original ECMWF dataset and the two reconstruction of the wind stress based on EOF analysis.

The bias between the rebuilt wind stress and original dataset in figure 3.21, confirm that the second EOF affects sensibly the EMED and, to a lesser extent, the WMED. EOF_1 has a high negative bias in the western EMED, in the Adriatic Sea, the Aegean Sea and eastern Levantine Sea, and in the south-eastern

and north-western part of the WMED. EOF_2 shows punctual high negative values of bias, especially in the eastern Levantine Sea. The RMSD in figure 3.22 shows that in both EOF_1 and EOF_2 the areas less effective reproduced are the Gulf of Lions and the Aegean Sea. This is not surprisingly as these are the areas with the highest variability of the wind stress. These considerations have to be taken in account when MED_exp_10y_ECMWF_frslp_vec_EOF_1 and MED_exp_10y_ECMWF_frslp_vec_EOF_2 simulations are discussed.

3.4.2 Model output

As a first evaluation of the results of the simulations, the integrated KE is shown in figure 3.23. The MED_exp_10y_ECMWF_frslp_vec_feb show an incredibly high KE with values that oscillates between 23 and more than $30\,cm^2/s^2$, that is more than the double of the KE of the control run. This prove the importance of the wind stress winter time conditions in provide KE to the Mediterranean Sea, supporting the idea of Winter time anomalous event that can overcame the seasonal cycle, especially in the EMED (Pinardi et al., 1997). MED_exp_10y_ECMWF_frslp_vec_atl and MED_exp_10y_no_wind_stress share almost the same decay of KE from $4\,cm^2/s^2$ of the initial conditions to a near-zero value. This may suggests that the circulation induced by the wind stress on the Atlantic ocean provide only a very small fraction of the KE to the Mediterranean Sea. However, this is a really delicate part. The coarse resolution of the model may not be adequate to reproduce a realistic Gibraltar Strait, that is a fundamental area for the exchanges between the Mediterranean Sea and the Atlantic Ocean. Indeed, in the model grid there is a single u-point that connect the Atlantic ocean and the Mediterranean basin. This fact has to be considered in all the following discussions. MED_exp_10y_ECMWF_frslp_vec_aug has a KE comparable with the control run, but the maximum values are shifted towards the Summer period. This is a characteristic even better observable in MED_exp_10y_ECMWF_frslp_vec_feb and can be due to the seasonal cycle of the thermal and saline surface boundary conditions, that in this simulations are the only fields that varies monthly. It is to point out that the KE of MED_exp_10y_ECMWF_frslp_vec_feb is much more affected from the seasonal cycle of temperature and saline in respect of MED_exp_10y_ECMWF_frslp_vec_aug. Simulations that uses an idealized wind have a KE closer to the control run but with differences that grow as the integration time grows especially from the 5^{th} year of integration. The two runs share almost the same kinetic energy during Winter, while in Summer the discrepancies are more evident due to the differences in EOF_1 and EOF_2 seen in the discussion of the previous section.

Another important diagnostic parameter is the volume integral of temperature and salinity, defined as:

$$< T >= \frac{1}{V}\int_V TdV, \qquad < S >= \frac{1}{V}\int_V SdV \tag{3.19}$$

The figures 3.24 and 3.25 show temperature and salinity volume integrals for the experiments carried out in this section. The seasonal variation of the temperature is evident in all the runs with the minimum value in February-March and maximum in August-September. The temperature integral for the control run, MED_exp_10y_ECMWF_frslp_vec_EOF_1 and MED_exp_10y_ECMWF_frslp_vec_EOF_2

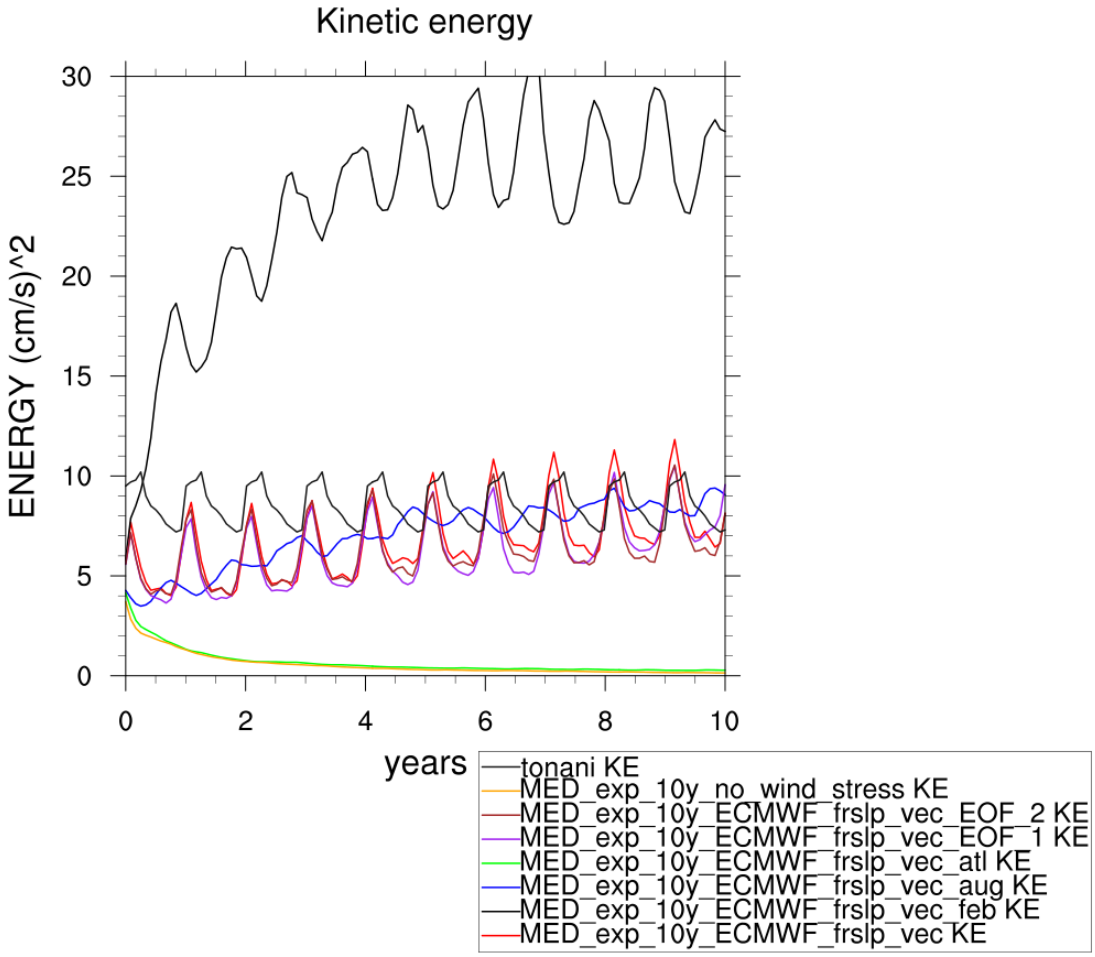

Figure 3.23: KE for the wind sensitivity simulations.

is very close with a starting value of $13.29\,°C$ and a final value of $13.55 - 13.56\,°C$. MED_exp_10y_ECMWF_frslp_vec_aug has an analogous behaviour with a more pronounced seasonal oscillation. MED_exp_10y_ECMWF_frslp_vec_feb shows the biggest change, with the same starting value of temperature and a final value of $13.76\,°C$. The wind seems to have an important role in the climatic temperature shift as MED_exp_10y_ECMWF_frslp_vec_atl shows a smaller temperature shift in respect of the full wind forced experiments and MED_exp_10y_no_wind_stress has no shift of temperature.
The salinity integral shows the biggest decrease for MED_exp_10y_ECMWF_frslp_vec_feb and MED_exp_10y_ECMWF_frslp_vec_aug with a difference of $0.0195\,psu$ for the latter run, with a starting value of $38.5264\,psu$ to $38.5069\,psu$ at the end of the integration. The seasonal cycle is still present with maximum decrease of salinity occurring in the end of the Winter and Spring. It is to notice the behaviour of MED_exp_10y_ECMWF_frslp_vec_atl, as it is the only run to have a gain in the salinity with a final value of $38.5325\,psu$. The other simulations have a similar curve with a small loss of salinity. Salinity for long simulations should be conserved, but

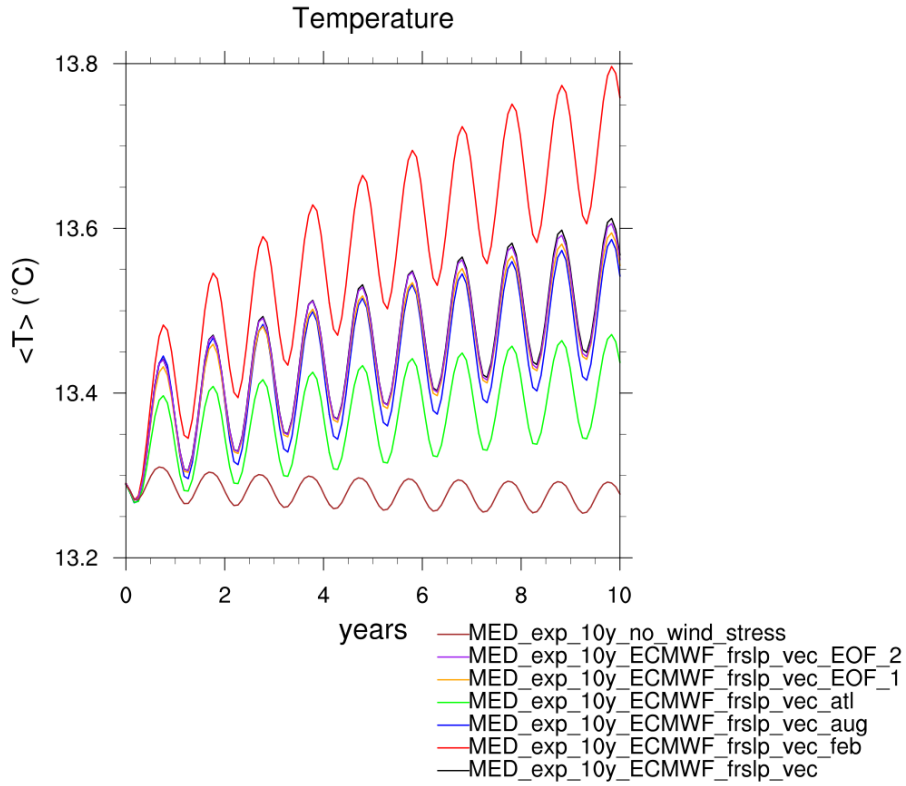

Figure 3.24: The basin average temperature for the experiment in table 3.3.

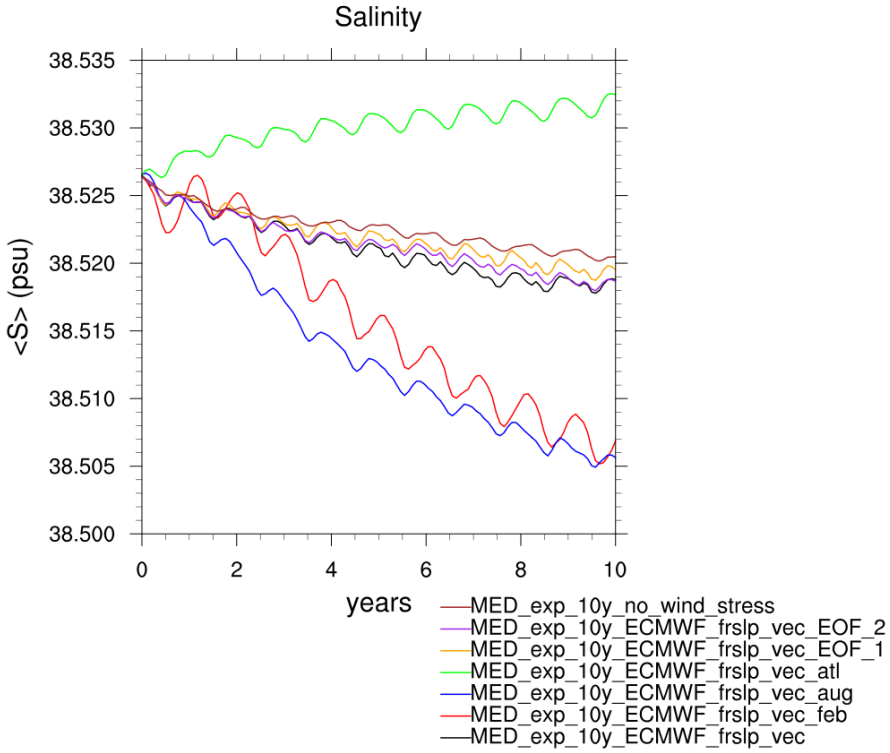

Figure 3.25: The basin average salinity for the experiment in table 3.3.

in the model the salinity is relaxed to a climatological value that introduces a feedback mechanism between water flux and the surface salinity that has no physical reasons, and then the salinity conservation is not assured (Roullet et Madec, 2000).

The surface circulation

The sea surface is strongly affected by the wind stress and wind stress curl and then the surface circulation response to changes in the wind stress is very high. The following picture 3.26 shows circulation snapshot for January and August of the last year of integration of the control run. It shows the principal permanent and

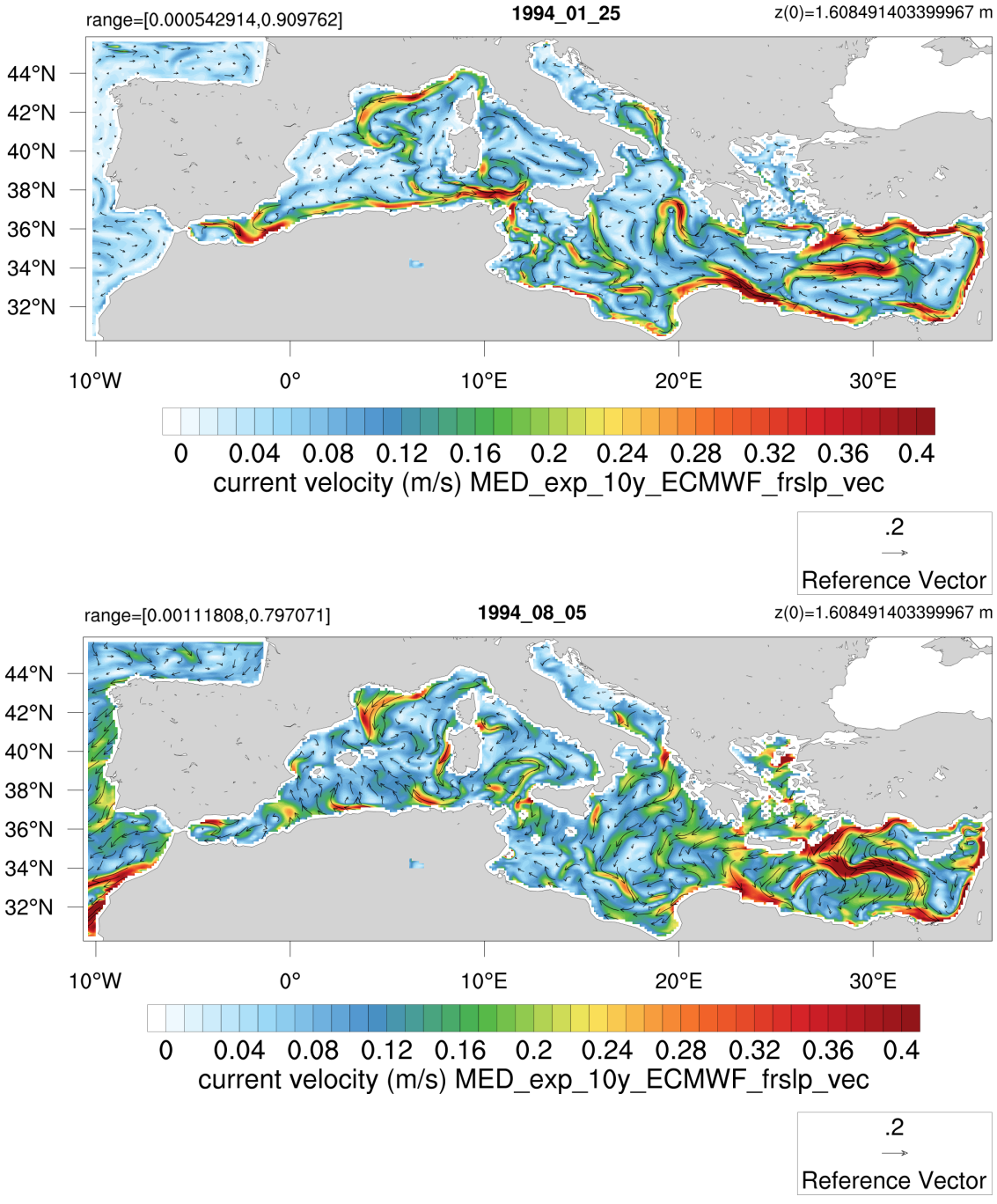

Figure 3.26: Circulation snapshot for the end of January (upper panel) and the beginning of August (lower panel) of the last year of integration of the control run.

semi-permanent features of the Mediterranean circulation of Winter and Summer. In Winter Starting from the WMED there are the Alboran gyres and the Almeraoran cyclonic eddy, the Algerian current in the northern African coast, the South-

Eastern Tyrrhenian Gyre (SETG) and the Norhtern Tyrrhenian Gyre (NTG) in the Tyrrhenian Sea, and a strong Liguro-Provencal-Catalan current (LPCC) as the northern branch of the Gulf of Lions Gyre (GLG). In the EMED, from the Sicily strait there is the Atlantic-Ionian Stream (AIS) going in south-eastern direction, the Northern Ionian Cyclonic gyre, the Southern Adriatic Gyre in the Adriatic Sea and the Syrte Gyre (SG) in the south-western EMED. More east there is the Cretan Passage Southern current (CPSC) and the double gyre system of anti-cyclonic Mersa-Matruh gyre (MMGS) and cyclonic Rhodes Gyres (RG) divided by a strong Mid-Mediterranean jet and a low signal of the Shikmona gyre system (SGS) in the eastern part of the Levantine Sea. In Summer boundary currents are less characterized. The Algerian current is no more recognizable, but an anti-cyclonic eddy appear south of Sardinia. In the EMED the SG extends toward north-west and an anti-cyclonic eddy appears in the central Ionian Sea. The double gyre system in the Levantine Sea persist but with a stronger Mid-Mediterranean jet.

The figures 3.27 and 3.28 represent circulation snapshot of MED_exp_10y_ECMWF_frslp_vec_feb

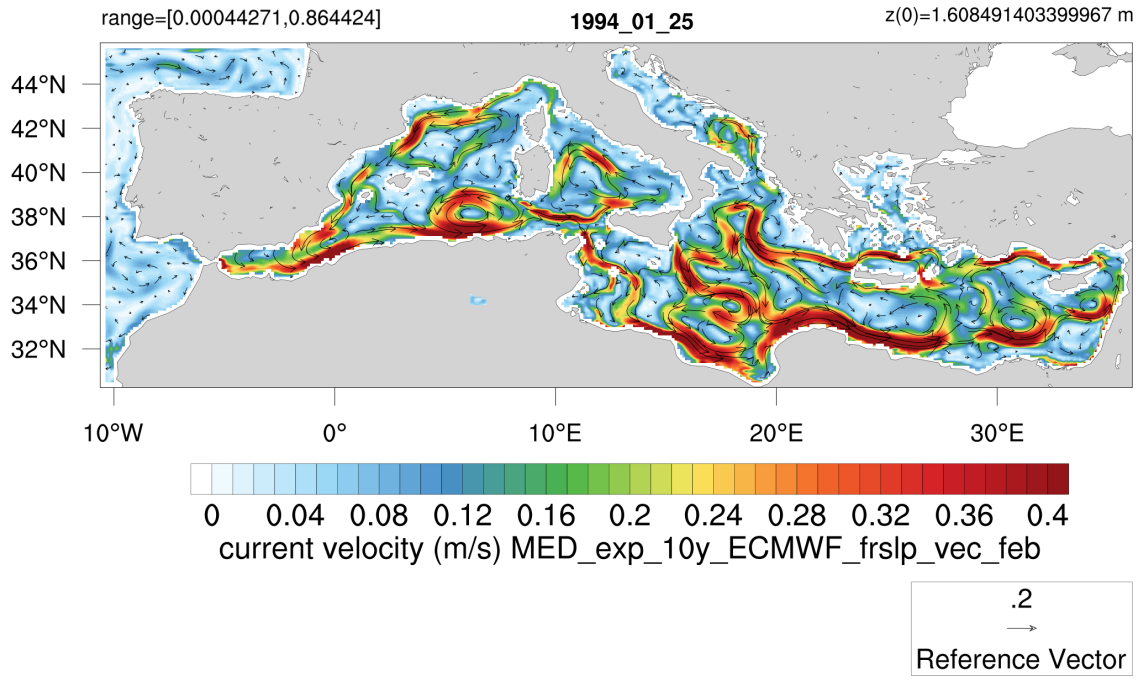

Figure 3.27: The surface circulation for MED_exp_10y_ECMWF_frslp_vec_feb at the end of January of the last year of integration.

and MED_exp_10y_ECMWF_frslp_vec_aug. These simulations, forced with the February and August forcing respectively throughout all the integration time, do not show a sensible seasonal variability, then these snapshot of the circulation are representative for the circulation patterns that can be permanently observed at each timestep and in the mean circulation. The Winter conditions experiment is very energetic. All the boundary and free jet currents are enhanced as well as all the cyclonic gyres and eddies that are peculiar of the Winter circulation. The SETG is bigger and occupies also the eastern Tyrrhenian sometime merging with the NTG. A branch of the LPCC continues his path along the southern coasts of France and Spain while the other branch turn southward east to the Balearic islands and form a strong GLG. A big Cyclonic eddy, that is not observed in normal conditions, is

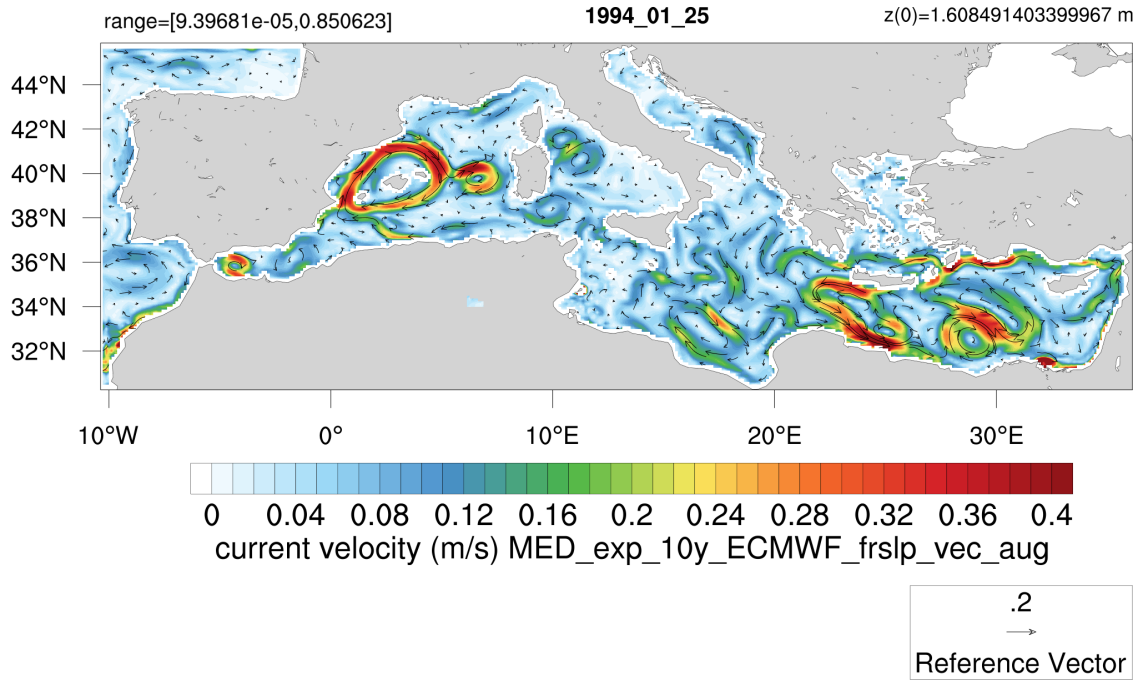

Figure 3.28: The surface circulation for MED_exp_10y_ECMWF_frslp_vec_aug at the end of January of the last year of integration.

formed south-west of Sardinia island. This is an interesting eddy because it is a permanent and energetic feature of MED_exp_10y_ECMWF_frslp_vec_feb. In the EMED the AIS is completely shifted southward. Instead of the anti-cyclonic SG, a cyclonic eddy appears occasionally. the AIS continue eastward along the African coast. The strong CPSC continue eastward and the mid-Mediterranean current is shifted southward, producing a big RG and only a small MMGS. The energetic flow of this simulation generates hydrodynamic instabilities, especially in free jets, like the mid-Mediterranean jet leading to a production of a large number of cyclonic and anti-cyclonic eddies. This feature is also observed in the current entering the Ionian sea along the Greek coasts, where the prevailing cyclonic circulation is often substitute by a large number of turbulent eddies. MED_exp_10y_ECMWF_frslp_vec_aug uses the typical Summer condition. The Summer wind stress is not as strong as the Winter stress. The circulation appear to be dominated by anti-cyclonic gyres and meanders. The only permanent cyclonic gyres are the Almera-Oran cyclonic eddy, the NTG and a weak SETG in the WMED, while in the EMED there are the South Adriatic gyre and the RG. Occasionally a weak GLG forms in the WMED and a Ierapetra gyre (IPG) in the EMED. The most peculiar permanent features are in the WMED. An anti-cyclonic gyres around Balearic islands forms after one and half years of integration and become permanent together with an anti-cyclonic eddy west of Sardinia. Another permanent anti-cyclone is always present between the SETG and NTG. In the EMED the circulation is more chaotic. In the central Mediterranean the SG is often present together with a varying number of anti-cyclonic eddies. The AIS is shifted northward, meandering in the Ionian Sea and forming, sometimes, anti-cyclonic eddies. More in the East the IPG gyre often occurs and the double gyres systems of MMGS and RG persist. These experiments are indeed not realistic, but may help to understand the role of the wind stress

in the Mediterranean surface circulation. The simulations show some characteristics of Winter and Summer circulation that can be recognized in the control run pictures (3.26), such the enhancement of the cyclonic circulation in Winter, and of the anti-cyclonic circulation in Summer. Moreover the AIS location seems to be very sensitive to the wind stress. This is a really important point as the NIR phenomenon is highly affected by the position of the AIS.

The circulation of the idealized wind stress experiments is depicted in 3.29 and 3.30.

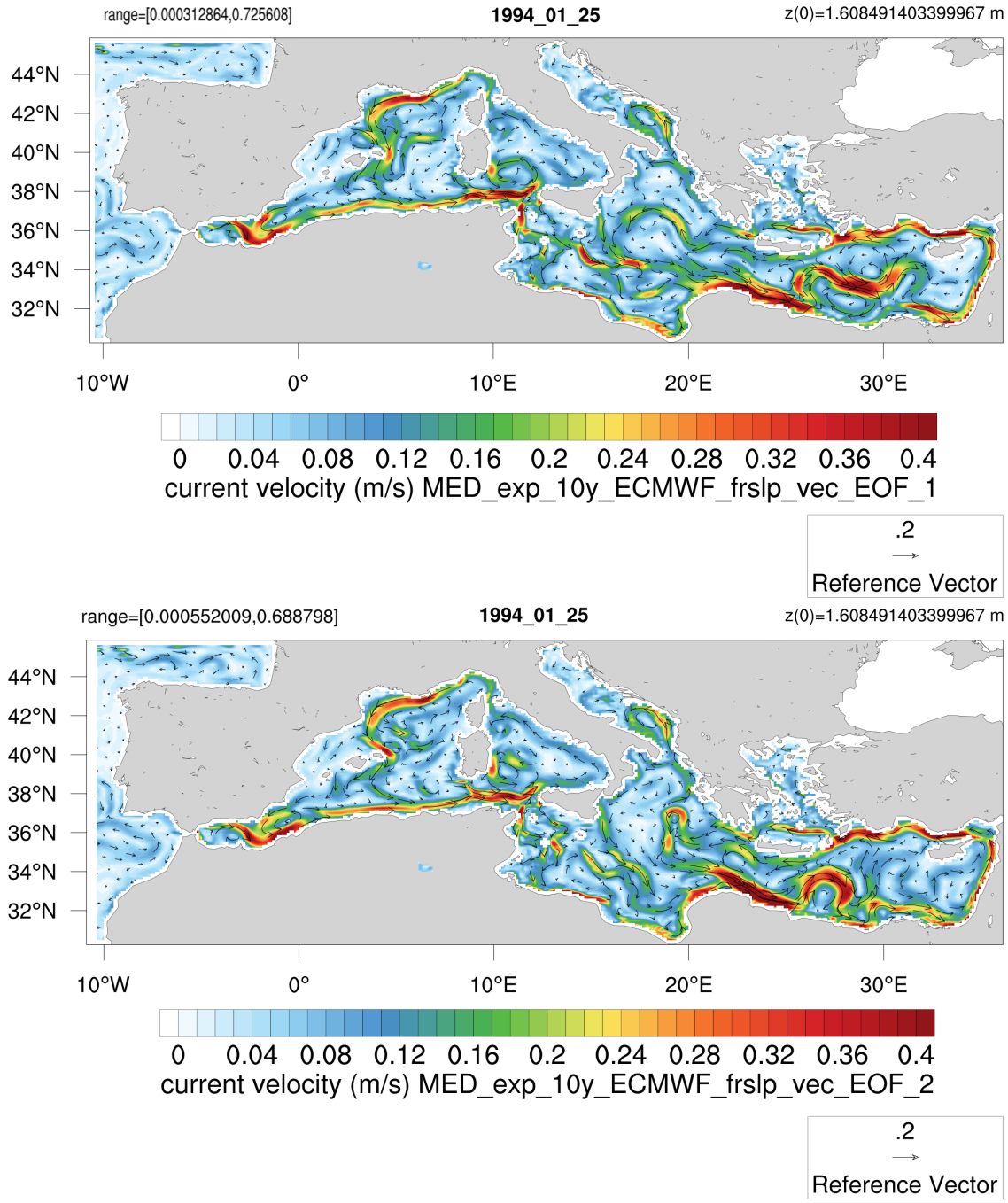

Figure 3.29: The surface circulation for MED_exp_10y_ECMWF_frslp_vec_EOF_1 (upper panel) and MED_exp_10y_ECMWF_frslp_vec_EOF_2 (lower panel) at the end of January of the last year of integration.

In the first figure The snapshot of the 25^{th} of January 1994 is shown to compare the results with the other simulations. The WMED circulation is represented quite good by MED_exp_10y_ECMWF_frslp_vec_EOF_1, and MED_exp_10y_ECMWF_frslp_vec_EOF_2 add only some details to the circulation. The biggest differences occur in the EMED. the EOF_1 winter wind stress has a weaker intensity and a slightly different direction, toward south-east in the Levantine sea, while remain zonal in the central Mediterranean, where the full forcing turn toward north-east. These conditions, applied on MED_exp_10y_ECMWF_frslp_vec_EOF_1, lead to a southward shift in the mid-Mediterranean jet position and then to a smaller MMGS and a bigger RG, while in the Ionian sea a branch of the westward current goes across the Ionian basin before rejoins the AIS. EOF_2 wind stress is very similar to the full forced

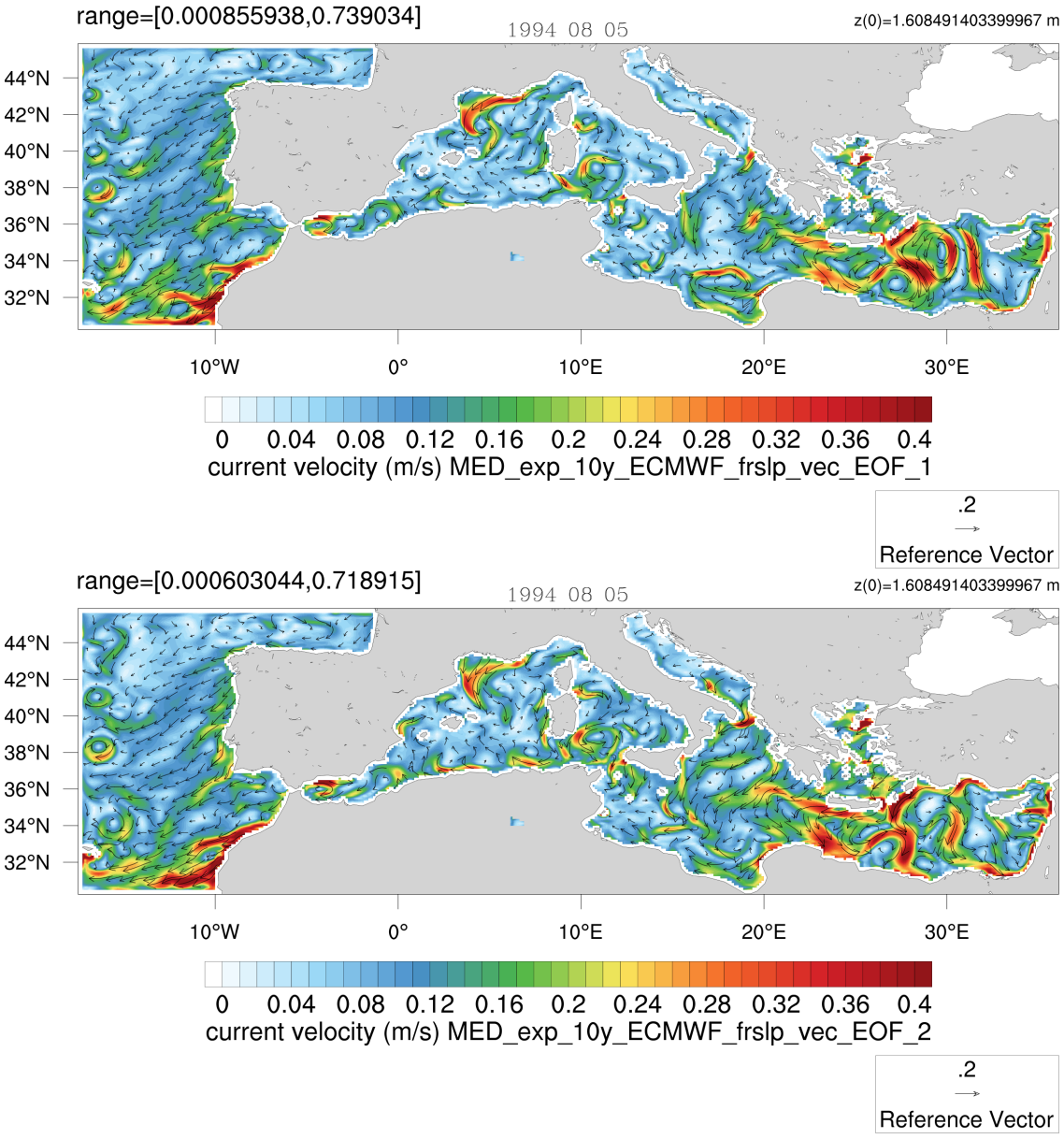

Figure 3.30: The surface circulation for MED_exp_10y_ECMWF_frslp_vec_EOF_1 (upper panel) and MED_exp_10y_ECMWF_frslp_vec_EOF_2 (lower panel) at the beginning of August of the last year of integration.

conditions and explain about the 85 % of the wind stress annual variability. It

catch well the direction of the stress, lacking in the intensity. Again the differences with the control run focus in the EMED, specifically in the double gyre system of MMGS and RG. The axis of the gyres system is slightly rotated clockwise lying on a north-east south-west line instead of being north-south oriented. It is interesting to note that the westward current in the Ionian Sea agrees with the one observed in the control run turning southward and join the AIS before going across the Ionian Sea. Similar considerations can be done for the Summer circulation in figure 3.30 except for some features like the axis of the MMGS/RG system that appear rotated also in MED_exp_10y_ECMWF_frslp_vec_EOF_1 and the Syrte gyre that, for EOF_1 experiment, is bigger than in the control run. If the EOF_2 wind stress add an intra-seasonal variability in the wind stress field as suggested in the previous section it can signify that this kind of variability may have a sensible role in the Ionian Sea, especially in Winter as the behaviour of the westward current differ sensibly in the two simulations. The EOF_1 wind stress conditions can be connected to the seasonal variability of the wind stress and explain enough variability (about 70 %) to reproduce almost entirely the circulation in the WMED. This can be seen as a further confirm of the fact that the WMED circulation is dominated by the seasonal cycle as suggested also in Pinardi et al. (1997).

The simulations MED_exp_10y_ECMWF_frslp_vec_atl and MED_exp_10y_no_wind_stress are discussed together as they show a similar pattern but with peculiar and interesting differences. The seasonal cycle of the circulation is small in both the runs but with a bigger signal in MED_exp_10y_ECMWF_frslp_vec_atl due to the wind stress seasonal cycle in the Atlantic box. In figure 3.31 the circulation of the 5^{th} of August 1994 for both experiments are shown. In the run not forced a small alboran gyre appear, then the current follows the Spanish coasts and branch south of Balearic islands. One branch follow the coast till Italian coasts while the other branch forms a jet in the middle WMED. In MED_exp_10y_ECMWF_frslp_vec_atl the Alboran gyre does not form, the current goes along the Spanish coasts and branch two times. The first branch occurs in the same position of the no wind case with one branch going across the WMED and the other following the coast. This along coast current branch again north of Balearic. One branch goes across the WMED and join the first branch's jet east of Balearic. The other branch goes through the Ibiza channel and join the jet south of the islands. The remote response of the circulation to the Atlantic forcing is sufficient to generate some interesting circulation feature. In this case the second branch of the current, that does not occur in the no wind case, is due to a stronger input current at Gibraltar Strait and to a small LPCC that forms along the French and Italian coasts. In the EMED the current passes across the Sicily strait along the Sicilian coasts. In the no wind case the current follow the Italian coast and branch in three parts south-east of Calabria. One branch continue along the coast, one branch forms a weak anti-cyclone in the middle of the Ionian and the last branch goes across the Ionian. This branch follow the greek coast southward and form a weak boundary current on Libyan and Egyptian coasts, then it forms a cyclonic gyre in the Levantine Sea. The remote wind case follow a similar path but branches in different points. The first branch in the EMED occurs south-east of Sicily. One weak branch follow the coasts, the other forms a weak AIS and eventually become a boundary currents like in the no wind case but this

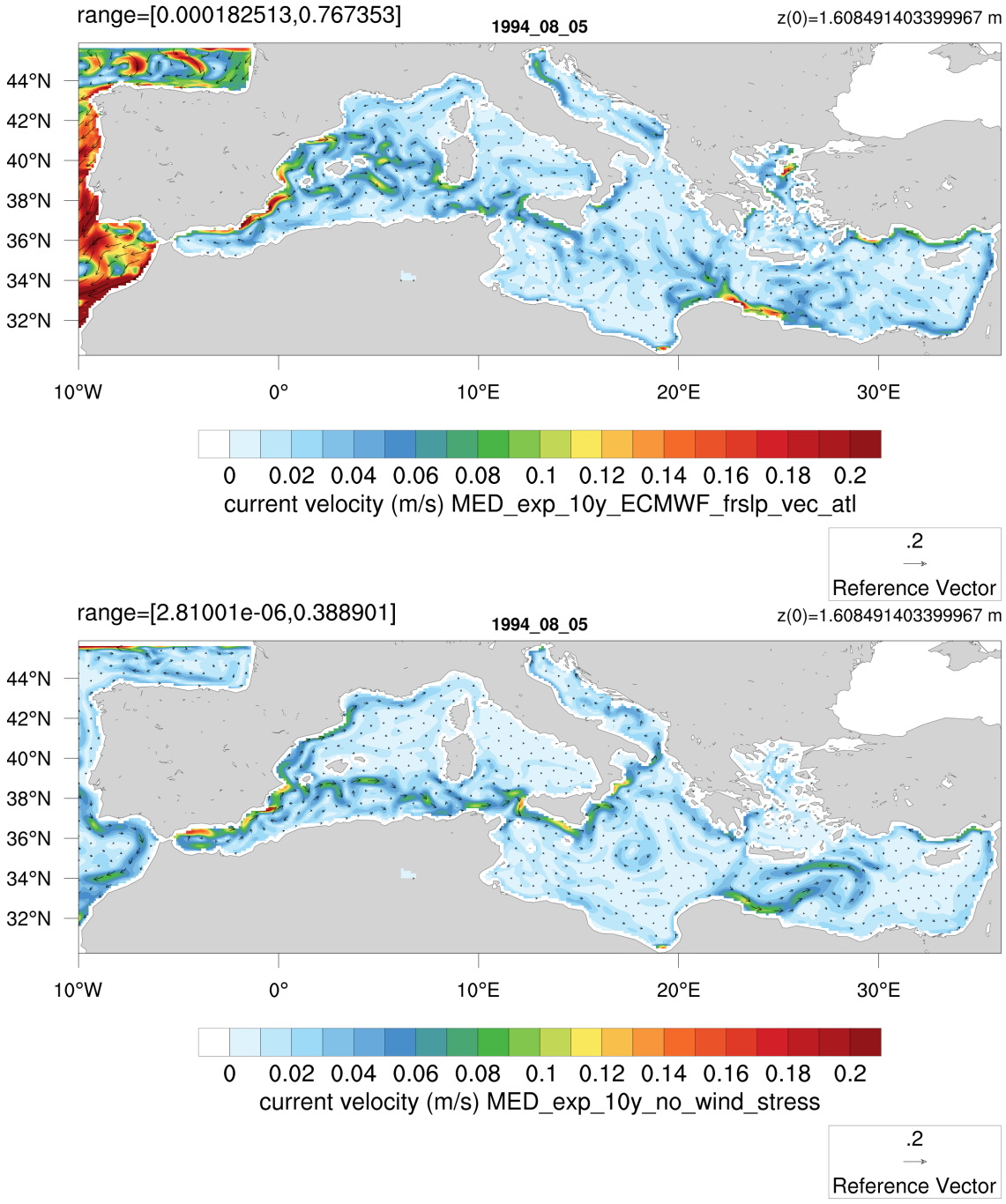

Figure 3.31: The surface circulation for MED_exp_10y_ECMWF_frslp_vec_atl (upper panel) and MED_exp_10y_no_wind_stress (lower panel) at the beginning of August of the last year of integration.

time it branches again leading to a boundary current along all the eastern coasts and to a weak current that disperses in the Levantine Sea. In both the simulations an anti-cyclonic circulation prevails in the northern Ionian. The remote forcing of the wind is sufficient to differentiate the circulation from the no wind case. in fact MED_exp_10y_ECMWF_frslp_vec_atl shows, even if weak, the AIS going across the central Mediterranean, while in the no wind case this branching is shifted northward. The remote forced run shows also a boundary current in the Levantine Sea that is not observed in the no wind case.

The Ionian Sea

Now the model output surface circulation of the Ionian sea is analysed with more details. The domain is reduced and is considered the Mediterranean Sea between 15 and 22° E longitude, and 34 and 40° N latitude. Figures 3.32 show the monthly

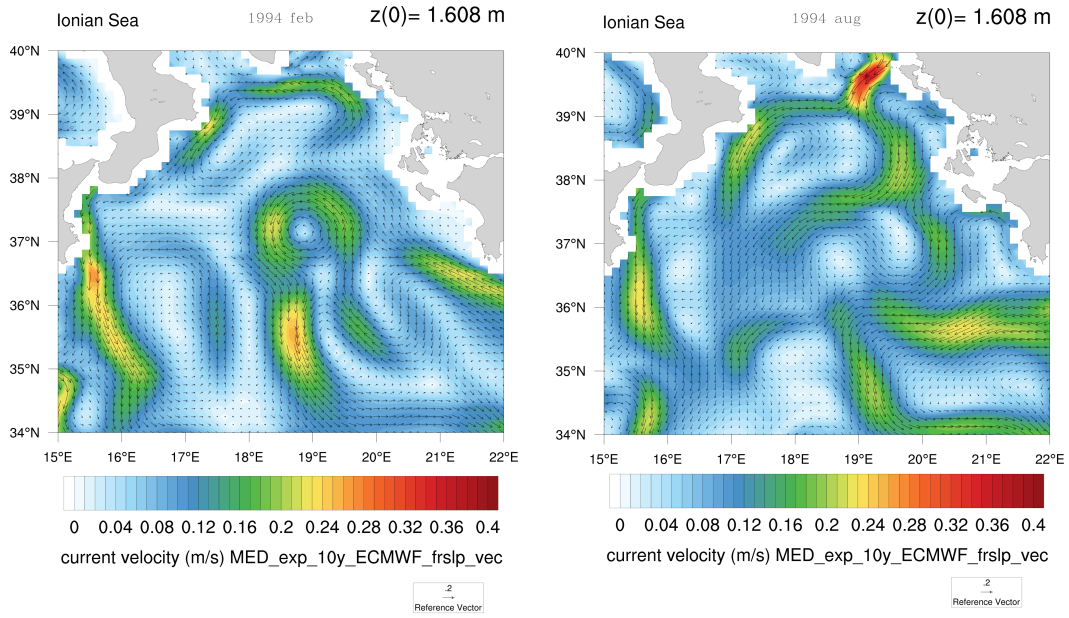

(a) February 1994 (b) August 1994

Figure 3.32: The surface circulation in the Ionian Sea for the control run in the February (left panel) and August (right panel) of the last year of integration.

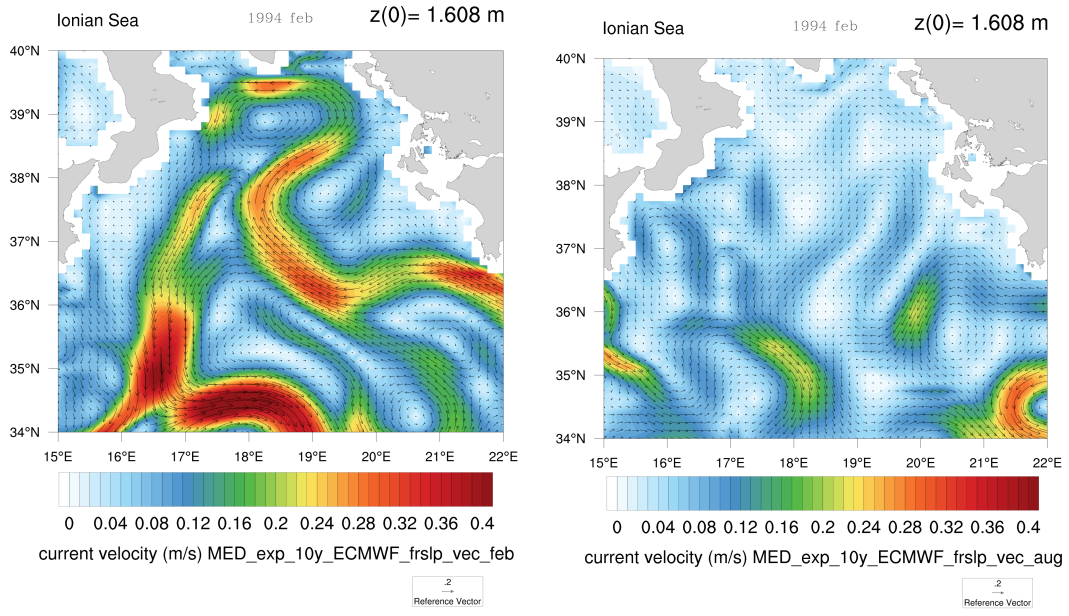

(a) February 1994 (b) February 1994

Figure 3.33: The surface circulation in the Ionian Sea for Winter forcing (left panel) and Summer forcing experiments (right panel) in the February of the last year of integration.

mean Ionian surface circulation of February and August of the last year of integration for the control run. In January the Cretan Sea westward current (CSWC) entries the Ionian sea and branches generating a meander that eventually forms a cyclonic eddy and turn southward. The other branch follow the coast and form a cyclonic circulation that is typical of the northern Ionian Sea, especially during Winter. In Summer the Western Adriatic coastal current (WACC) from the Adriatic Sea entries in the northern Ionian and branches and give rise to many small cyclonic and anti-cyclonic eddies. The circulation is not well defined as in the Winter season.
In 3.33 the same figures are shown for MED_exp_10y_ECMWF_frslp_vec_feb and MED_exp_10y_ECMWF_frslp_vec_aug. The CSWC current in the Winter conditions run reach the middle of the Ionian Sea before to bifurcates, with one branch going southward and the other branch northward. The northward branch give rise to a cyclonic circulation in the northern Ionian and an anti-cyclonic eddy on the south-eastern flank of the current. It is common for this experiment to have such circulation pattern with an overall cyclonic circulation in the Ionian Sea. The Summer conditions run shows an AIS shifted northward. In this more detailed picture the AIS meanders can be seen in the left bottom corner. This meanders occasionally but frequently gives rise to closed anti-cyclonic eddies that spread northward. The CSWC flowing in the Ionian Sea turn initially southward and then northward and eventually again southward joining the AIS. This behaviour frequently gives rise to cyclonic and anti-cyclonic eddies that spread in the Ionian sea.

The EOFs experiments circulation of the Ionian sea is represented in 3.34 and

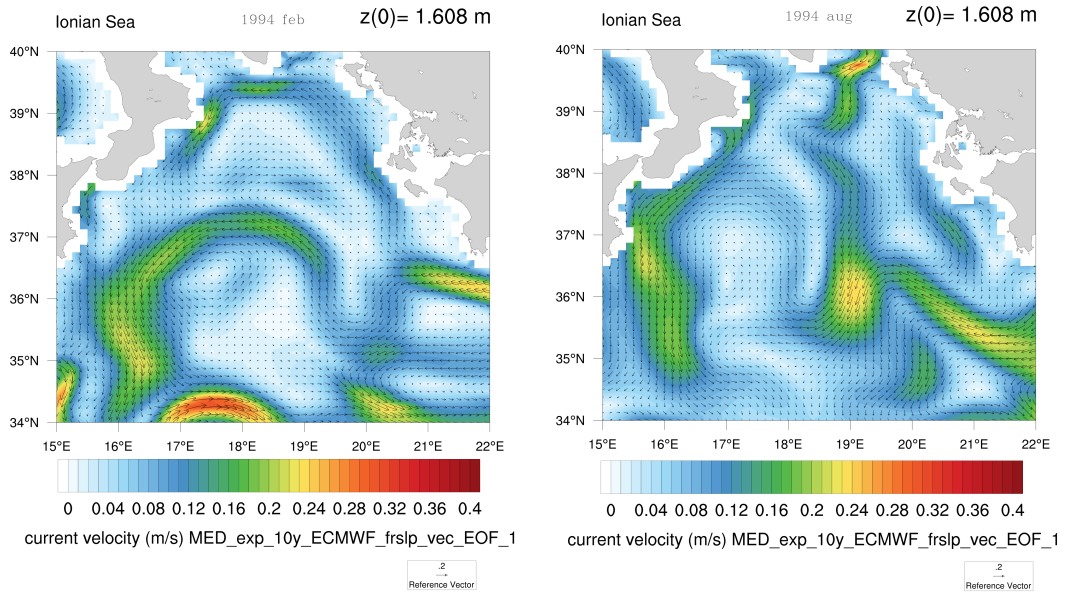

(a) February 1994 (b) August 1994

Figure 3.34: The mean surface circulation in the Ionian Sea for EOF_1 experiment of February (left panel) and August (right panel) of the last year of integration.

3.35 for the same time interval of the control run. The circulation of the EOF_2 experiment is very close to the control run circulation both in Winter and Summer, in fact differences between EOF_2 and the control run are focused in the eastern

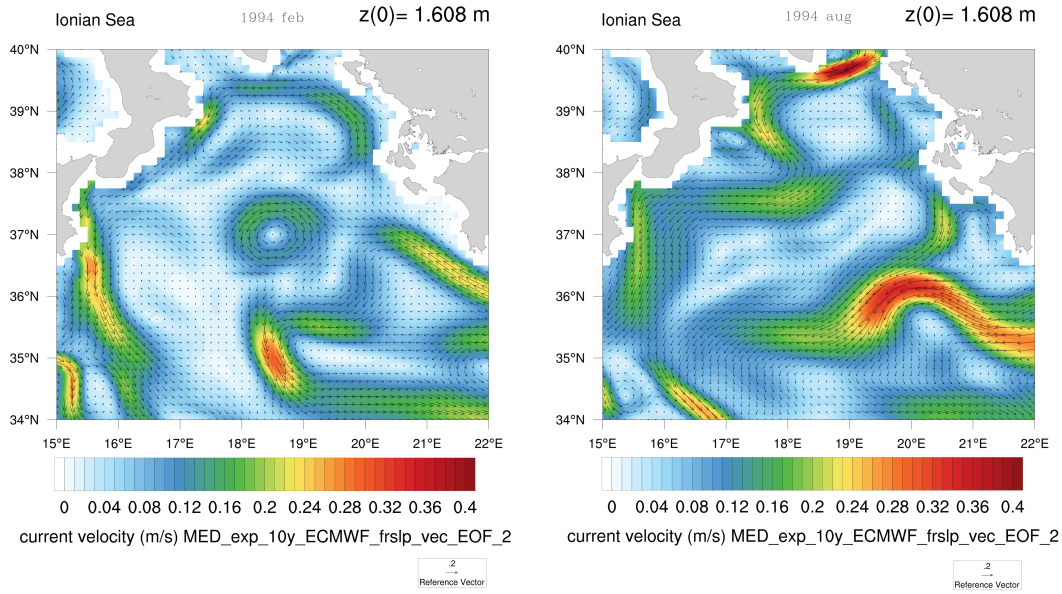

(a) February 1994 (b) February 1994

Figure 3.35: The mean surface circulation in the Ionian Sea for EOF_2 experiment of February (left panel) and August (right panel) of the last year of integration.

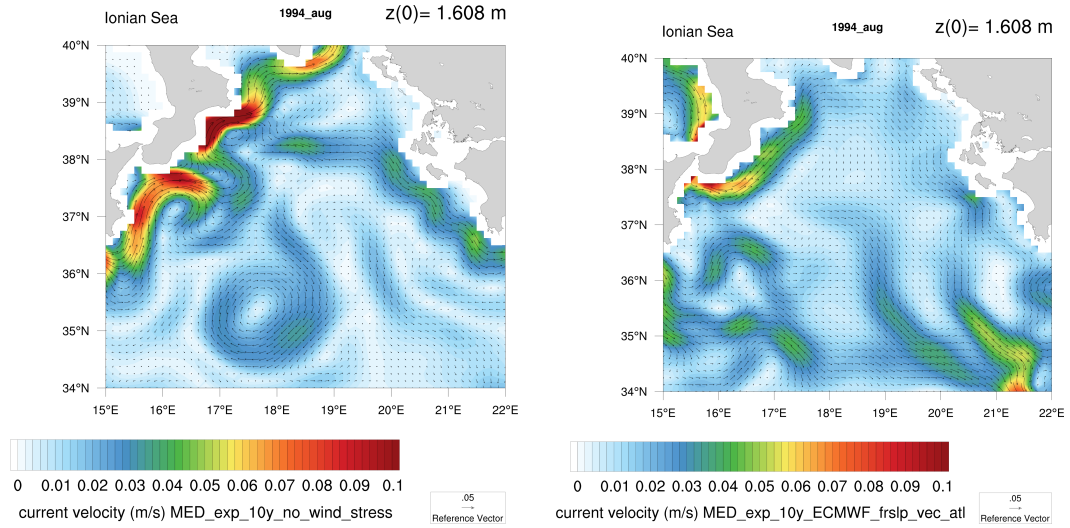

(a) February 1994 (b) August 1994

Figure 3.36: The mean surface circulation in the Ionian Sea for no forcing (left panel) and remote forcing (right panel) experiment for the August of the last year of integration.

part of the EMED. Different is the case of EOF_1. A weaker and more zonal wind stress in the EMED allow a branch of the CSWC to cross the Ionian Sea during winter, then the current turn southward and join the AIS. In the northern Ionian the northward branch of the CSWC feed a cyclonic circulation. In Summer the southward current from the Adriatic Sea join the CSWC in the middle of the Ionian and form a southward boundary current that eventually join the AIS.

The no forced and remote forced case are shown in figure 3.36 but do not add

further information as there are no small size structure to be described in detail and are represented for completeness. Here the scale of the current speed is resized to allow a better distinction of the boundary current, and of the bifurcation position that is clearly more northward in the no forced case.

Chapter 4

Diagnostic studies of the NIR

In Chapter 1 the Northern Ionian Reversal (NIR) phenomenon was introduced and discussed. In this chapter the NIR index is defined and evaluated for different reanalysis datasets and numerical model output.

4.1 Methodology

It is well known that the SSH can be used to establish the prevailing circulation in the region under analysis. If the SSH has closed contours and positive values at the center, the circulation will be anti-cyclonic in the northern hemisphere, the contrary if it is negative. The NIR index is computed on the SSH at two points in the Ionian Sea, at $38°N$ $18°E$ (point A) and $35°N$ $18°E$ (point B; see figure 4.1). This index is useful to describe the circulation pattern of the Northern Ionian Sea,

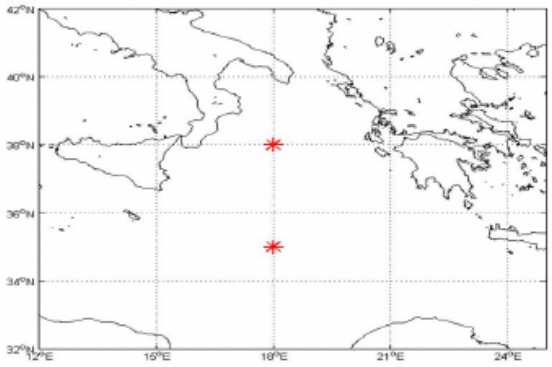

Figure 4.1: Geographical position of the points used for the computation of the NIR index (Ingrosso, 2015).

and it can show the reversal of the circulation from anti-cyclonic to cyclonic and vice-versa. Two definitions are used for the NIR index. The first is:

$$
\begin{aligned}
NIR_A &= \frac{\overline{SSH}_A - \overline{SSH}_{clim_A}}{\sigma_{SSH_A}} \\
NIR_B &= \frac{\overline{SSH}_B - \overline{SSH}_{clim_B}}{\sigma_{SSH_B}} \\
NIR &= NIR_A - NIR_B
\end{aligned}
\tag{4.1}
$$

where the overline indicates a time mean over a period that usually may be a month, and $\overline{SSH}_{clim_*}$ indicates the time mean of the climatological value of the SSH at * point. σ_{SSH_*} represent the standard deviation of the SSH over the mean period in points A and B and act as a normalization parameter. Alternatively the NIR index can be defined as:

$$\begin{aligned} NIR_{ns} &= \overline{SSH}_A - \overline{SSH}_B \\ NIR &= \frac{NIR_{ns} - \overline{NIR_{ns}}}{\sigma_{NIR}} \end{aligned} \tag{4.2}$$

where NIR_{ns} indicates the non-normalized NIR index and σ_{NIR} is the standard deviation of the NIR_{ns} series. Since there is a high correlation between the two definitions of the NIR index (Ingrosso, 2015), the latter one (equation (4.2)) will be used in the following section. The SSH from the different reanalysis datasets described in chapter 2 will be used to compute the NIR index. Datasets have different temporal domain, so first each dataset will be analysed independently and the comparison between datasets will be described in the last section.

4.2 The NIR from reanalysis dataset

Despite the different resolutions and forcing all the reanalysis datasets show a change in the sign of the NIR index around the 1997. Indeed, this is due to the reversal of the current in the northern Ionian Sea. Mean Maps of SSH (figure 4.3 and 4.3) for the reference periods A (1987-1996) and B (1997-2007) confirm the reversal of the circulation pattern. Only the SSH maps of CMEMS reanalysis are shown as all the datasets have similar features in the mean value of SSH. In the following section the results from the reanalysis are shown and discussed.

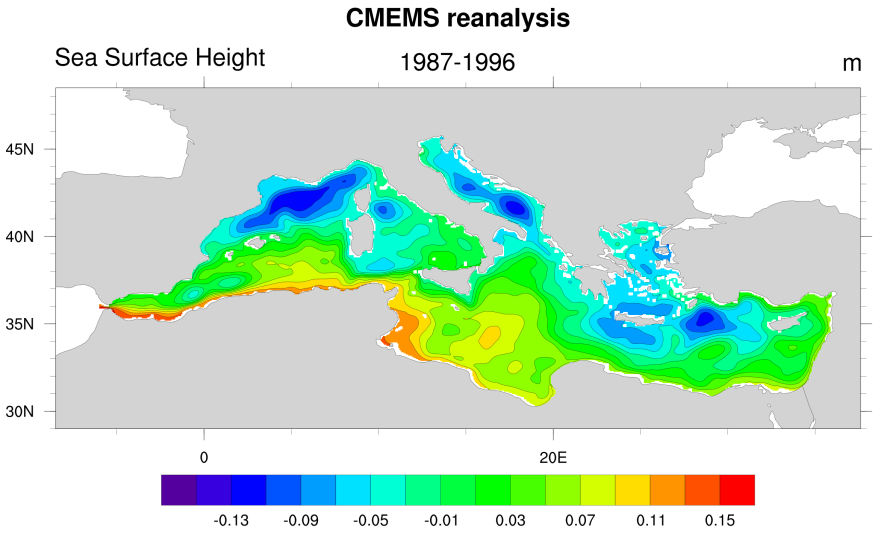

Figure 4.2: Mean SSH fields for CMEMS reanalysis for the period 1987-1996.

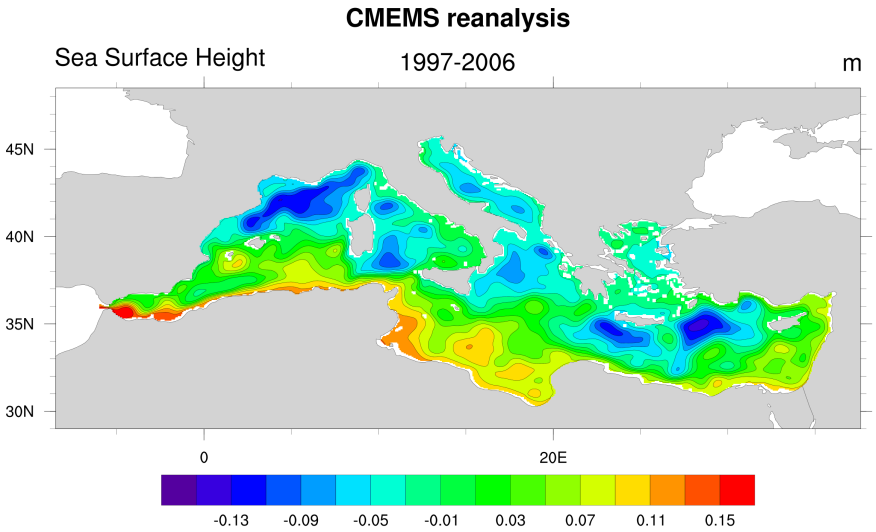

Figure 4.3: Mean SSH fields for CMEMS reanalysis for the period 1997-2006.

4.2.1 NIR index

C-GLORS reanalysis

The results of the calculation of the NIR index from C-GLORS are shown in figure 4.4. Between the 1996 and 1997 the NIR changes sign indicating the reversal of the current. In 2005 a positive trend of the index begins with some positive peaks between 2006 and 2008. From 2012 the index change sign again but the series is

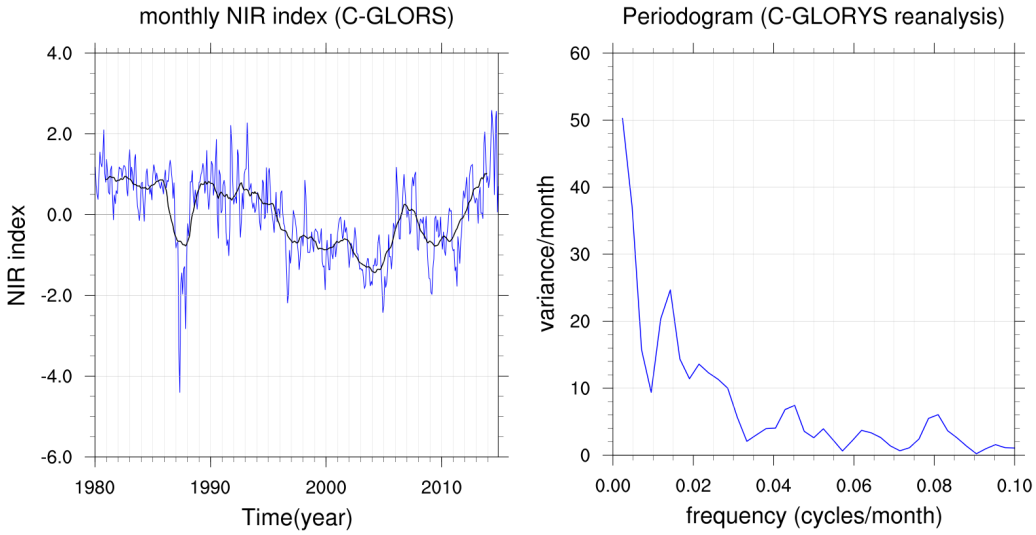

(a) NIR index (b) periodogram

Figure 4.4: NIR index and periodogram computed for the entire periods of C-GLORS reanalysis (1980-2014). The black curve is a running mean value obtained with a 24 month time window.

too short to understand if a real reversal has occurred. The periodogram show the range of frequencies of the NIR index and is normalized so that the area under the curve is equal to the variance of the detrended series. It show a large peak at low

frequencies, sign of the interannual variability of the NIR. At smaller frequencies there is a peak near 0.018 and 0.021 cycle/month corresponding to a signal of about 4.6 and 3.9 years period respectively. The signal at 0.045 cycle/month corresponds to about 1.9 years period and the peak at 0.08 cycle/month is the seasonal cycle of the NIR.

CMEMS reanalysis

The CMEMS reanalysis shows again a reversal of sign in 1997 as for the C-GLORS.

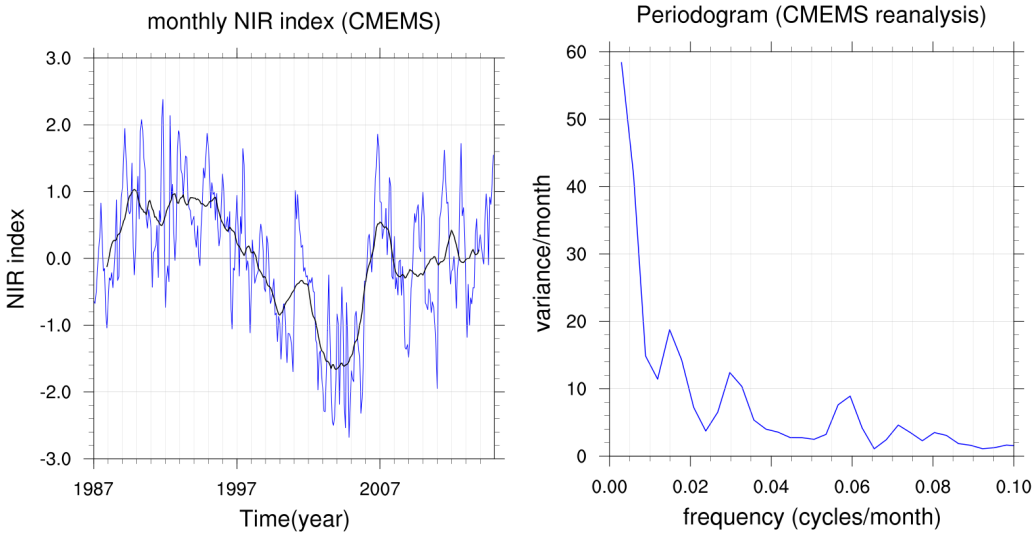

(a) NIR index (b) periodogram

Figure 4.5: NIR index and periodogram computed for the CMEMS reanalysis (1987-2014).

Between 2001 and 2002 there is a positive NIR peak, also present in C-GLORS reanalysis. After 2006 a transition phase starts with alternate years of positive and negative peaks. As in C-GLORS the NIR index changes sign between 1987 and 1988. The Periodogram share a similar pattern with C-GLORS but have a peak slightly shifted at smaller frequency of 0.03 cycle/month.

NextData_RR reanalysis

The NextData_RR reanalysis is the longest dataset analysed (1955-2014). It is evident now that the negative NIR index values between the 1997 and 2007 are the largest in the time series. This may suggest the NIR phenomenon to be a single event occurred around the 1997. Nevertheless, looking at the whole time series some other negative NIR values appear with higher frequency. The periodogram here is more noisy but shows the same characteristics of the other reanalysis with a dominant signal at 0.018 cycle/month and at very low frequencies.

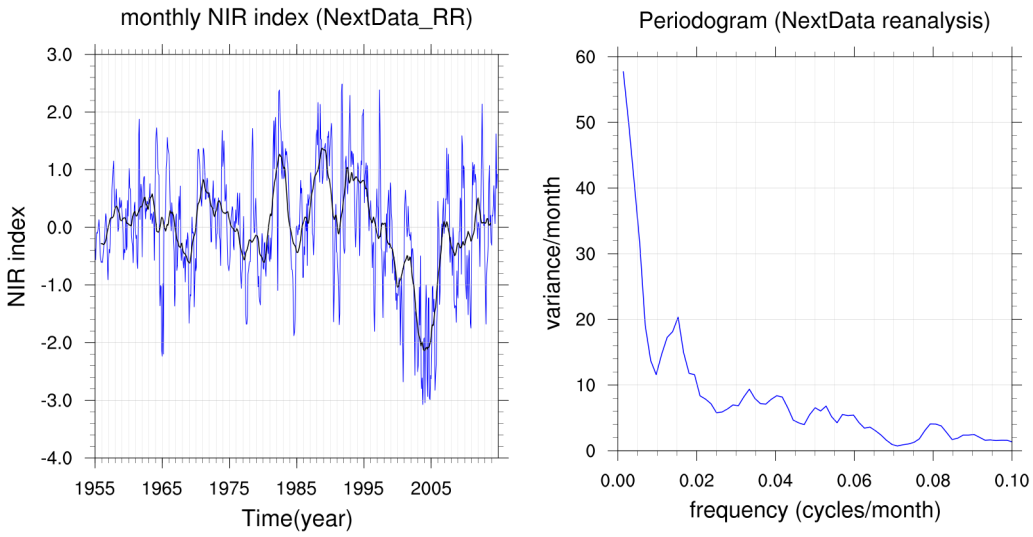

(a) NIR index (b) periodogram

Figure 4.6: NIR index and periodogram computed for the NextData_RR reanalysis (1955-2014).

4.3 The NIR from model output

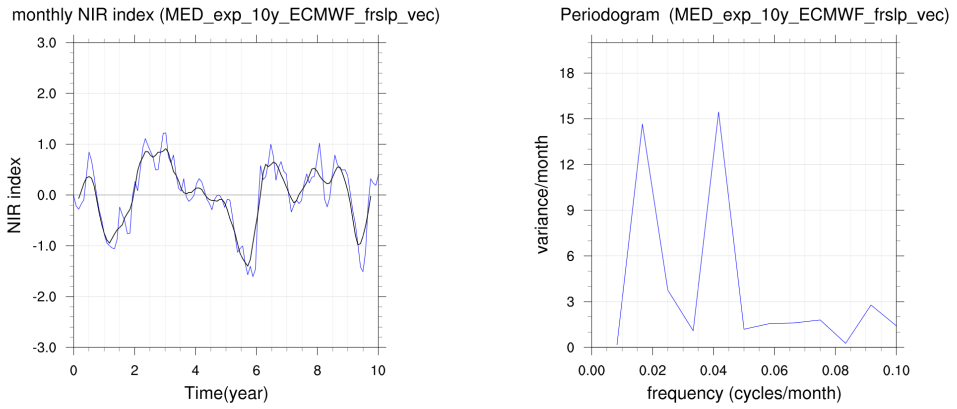

(a) NIR index (b) periodogram

Figure 4.7: NIR index and periodogram computed for the control run. In this and all the following figures of the section the black curve is a running mean over a window of 6 months.

in this section the NIR index is evaluated for the wind sensitivity experiments. All the NIR index time series computed for the model output are detrended before to be displayed here. It is to point out that this analysis may be influenced by transient signals due to relaxation of the model from the initial climatological conditions to a state in equilibrium with the external forcing, so, as for the KE, values

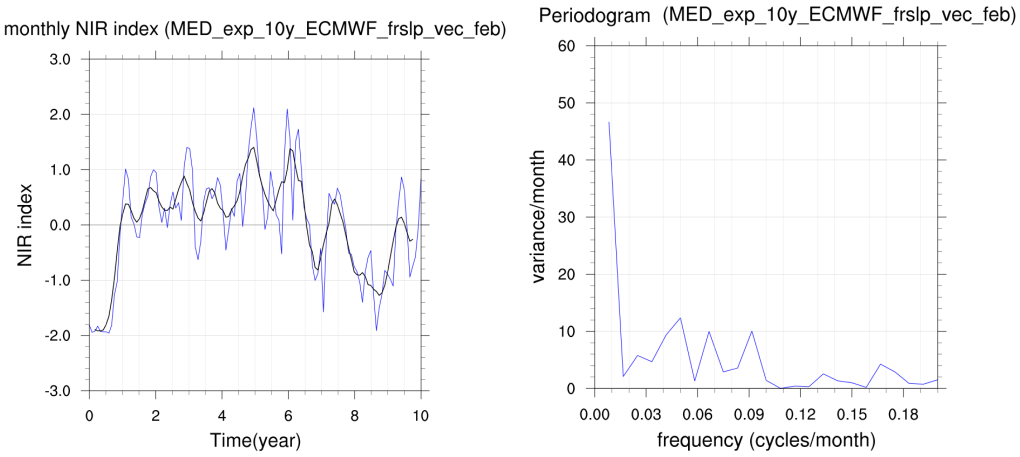

(a) NIR index (b) periodogram

Figure 4.8: NIR index and periodogram computed for the February forcing experiment.

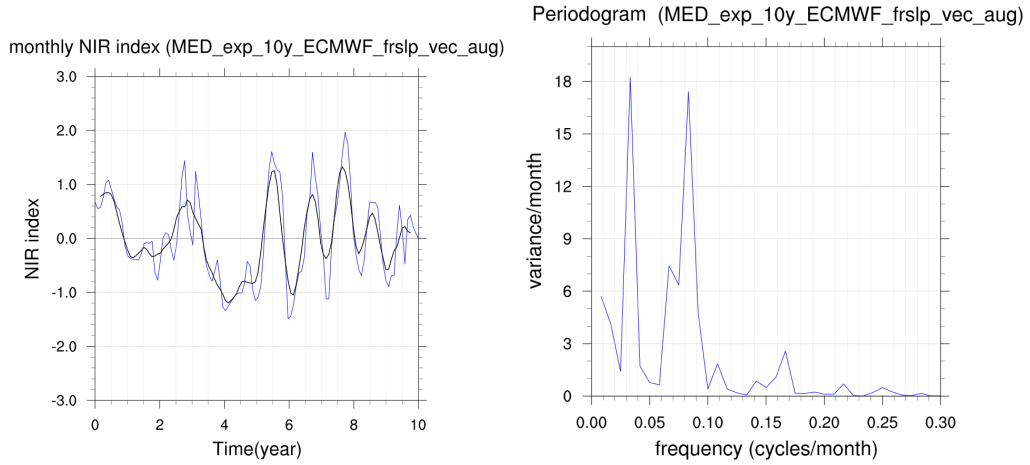

(a) NIR index (b) periodogram

Figure 4.9: NIR index and periodogram computed for the August forcing experiment.

of the NIR index after the 5 years of integration are considered more reliable.
The Figure 4.7 shows the NIR index and the relative periodogram for the simulation MED_exp_10y_ECMWF_frslp_vec.The index oscillates at different frequencies and seems to be regular. Indeed, the periodogram peaks at very precise frequencies corresponding to periods of 5 and 2 years with a smaller annual cycle.
MED_exp_10y_ECMWF_frslp_vec_feb shows a more noisy index, with abrupt changes to positive values at the beginning of integration, and to negative values after 6 years of integration. These abrupt changes are responsible for the low frequency peak in the periodogram. The prevailing negative values in the right section of the time series are considered a signature of the prevailing cyclonic circulation in the northern Ionian sea. The periodogram shows three smaller peaks at frequencies comprises between 0.02 and 0.1 cycles/month corresponding to periods between 4 years to 10 month.
Figure 4.9 shows NIR index for August forcing simulation. The NIR index shows high excursion between negative and positive values, especially in the second half

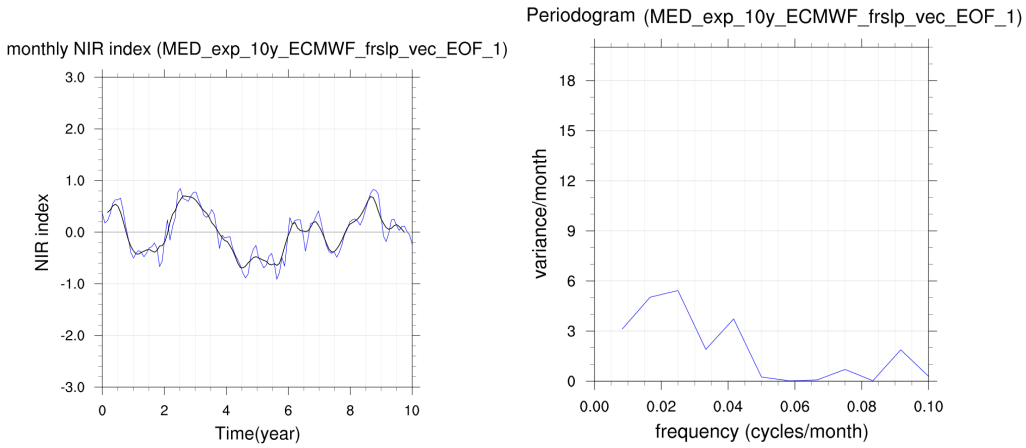

(a) NIR index (b) periodogram

Figure 4.10: NIR index and periodogram computed for the EOF_1 forcing experiment.

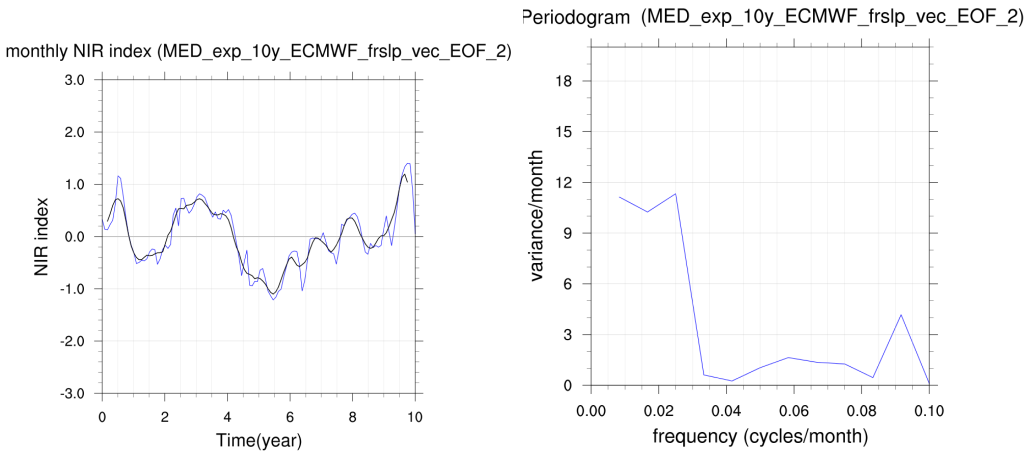

(a) NIR index (b) periodogram

Figure 4.11: NIR index and periodogram computed for the EOF_2 forcing experiment.

of the time series where regardless the oscillations positive values seems to prevail. The periodogram shows two important peaks with annaul period and and 2.3 year period.
The EOF experiments have a NIR index similar to the control run in the first half. the second half shows the biggest differences. The periodogram show similar features to the control run in MED_exp_10y_ECMWF_frslp_vec_EOF_1 while MED_exp_10y_ECMWF_frslp_vec_EOF_2 lack in the component at 0.04 cycles/month. The remote forced simulation MED_exp_10y_ECMWF_frslp_vec_atl and the no forced run MED_exp_10y_no_wind_stress have a similar NIR index and periodogram with a very smooth curve. the periodogram of the NIR of both runs peaks at 0.025 cycles/month corresponding to a period of 3.3 years. It is to verify whether this component of the NIR index depends on the real physics or is an artificial mode due to the relaxation of the system. The remote forced experiment has a smaller peak at 0.04 cycles/month, that is 2 year period component, that may be attributed to the remote wind forcing. It is to verify if the spectral components of the NIR index

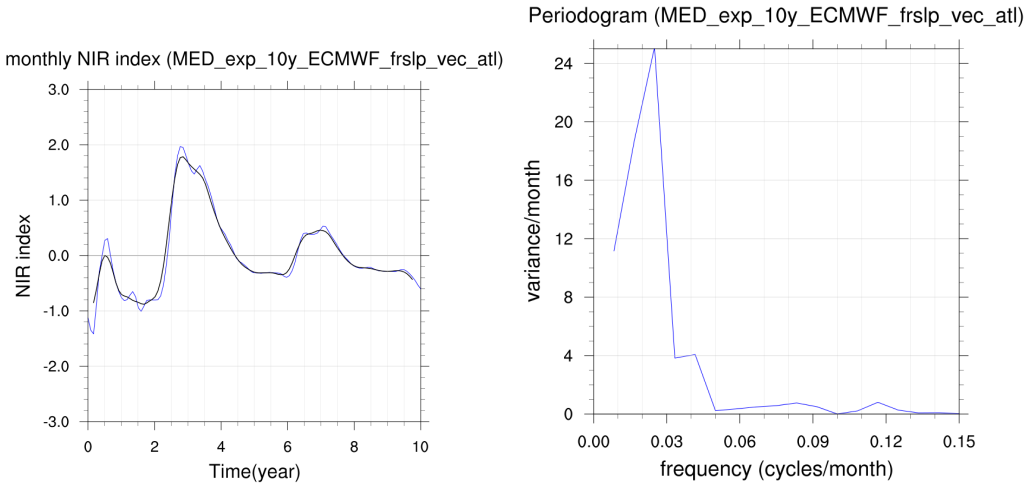

(a) NIR index (b) periodogram

Figure 4.12: NIR index and periodogram computed for the remote forcing experiment.

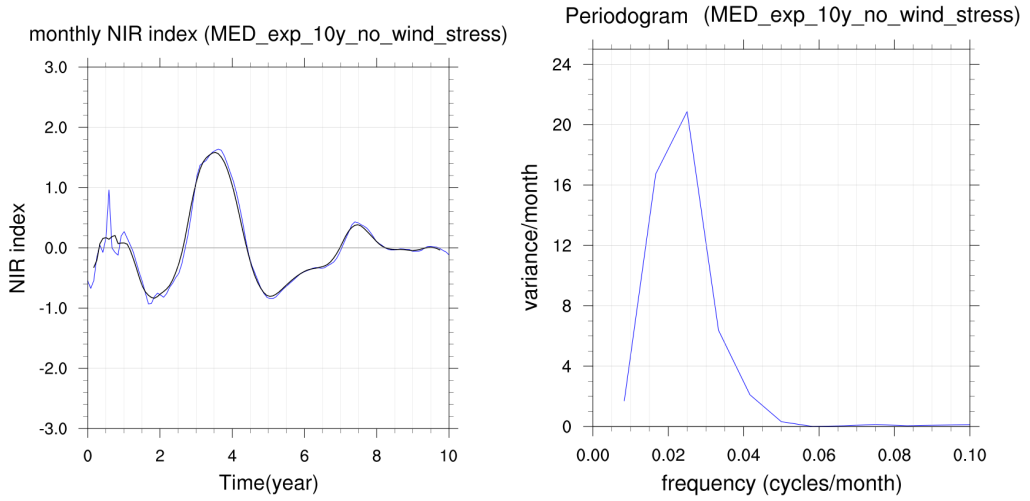

(a) NIR index (b) periodogram

Figure 4.13: NIR index and periodogram computed for the no forcing experiment.

with 2 and 5 years period in the control run may be attributed to the seasonal cycle of the wind stress.

4.4 The NIR from satellite observations

The NIR index will now be analysed using measurements of SLA from satellite altymetry observations. NIR index can be computed from the reconstructed SSH and comparison between satellite data and reanalysis dataset can be done. Satellite measurements are provided by CMEMS. The SLA used here is a level 4 product from SSALTO/DUACS, which integrates data from all altimeter missions: HY-2A, Saral/AltiKa, Cryosat-2, OSTM/Jason-2, Jason-1, Topex/Poseidon, Envisat, GFO, ERS-1&2. The Mean Dynamic Topography (MDT), provided by Aviso+, is added to the SLA to achieve the Absolute Dynamic Topography (ADT), that measure

the SSH in respect to a reference geopotential surface, and is the quantity closer to the SSH provided by model output. Data are provided on a uniform grid with a horizontal resolution of $\frac{1}{8}^\circ \times \frac{1}{8}^\circ$. Mean maps of observed SSH show the same pattern already seen for reanalysis dataset as well as the observed NIR index (figure 4.14 and 4.15). In the next section a comparison between reanalysis and observations is made in order to validate the reanalysis.

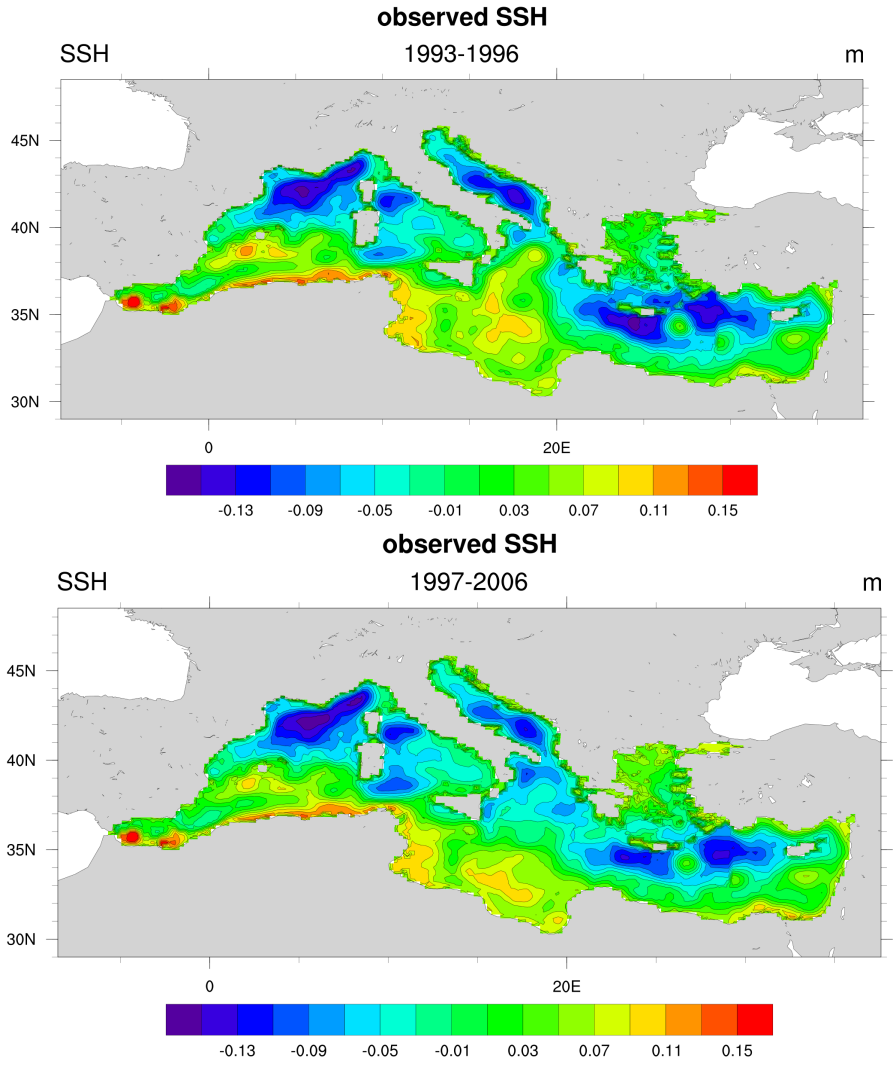

Figure 4.14: Reconstructed SSH field from SLA satellite altymetry measurements. mean SSH maps of the period 1993-1996 (upper panel) and 1997-2006 (lower panel).

4.4.1 Comparison

To evaluate the quality of the reanalysis, RMSE, correlation and BIAS standard deviation (BIAS STD) of the difference between satellite SSH and model are computed and shown (figure 4.16, 4.17 and 4.18) for the three reanalysis.

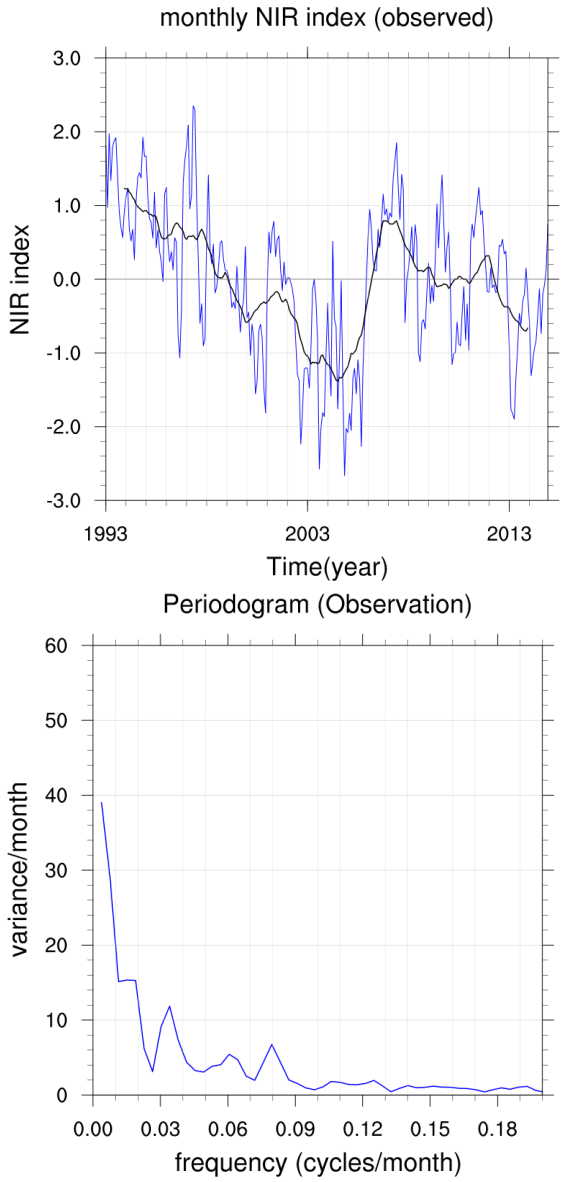

Figure 4.15: NIR index for the SLA satellite data (1993-2014) and relative periodogram.

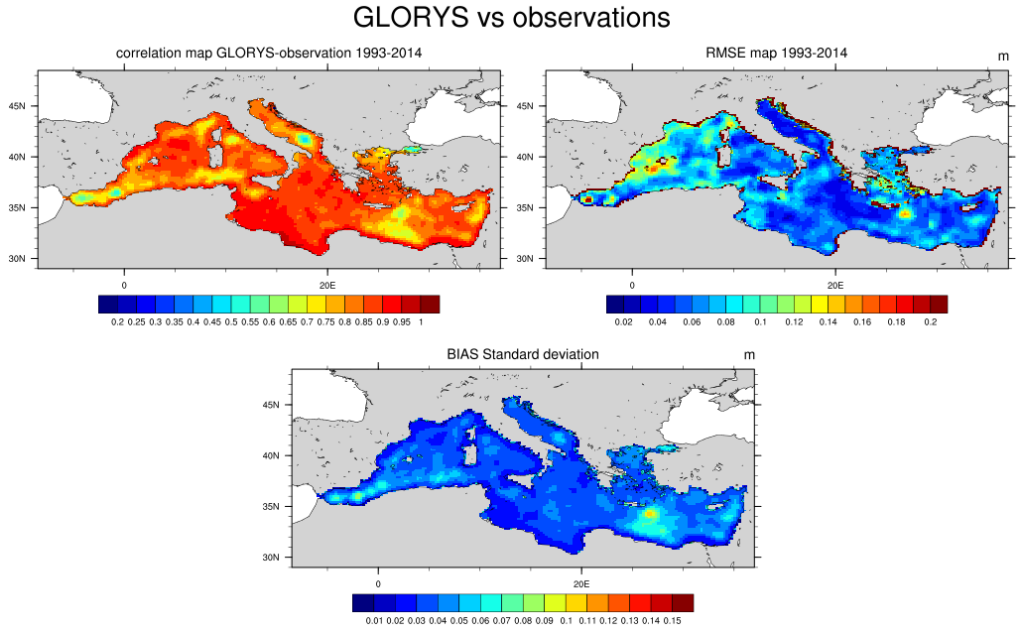

Figure 4.16: Correlation (upper left panel), RMSE (upper right panel) and BIAS STD (lower panel) for the SSH field of the C-GLORS reanalysis.

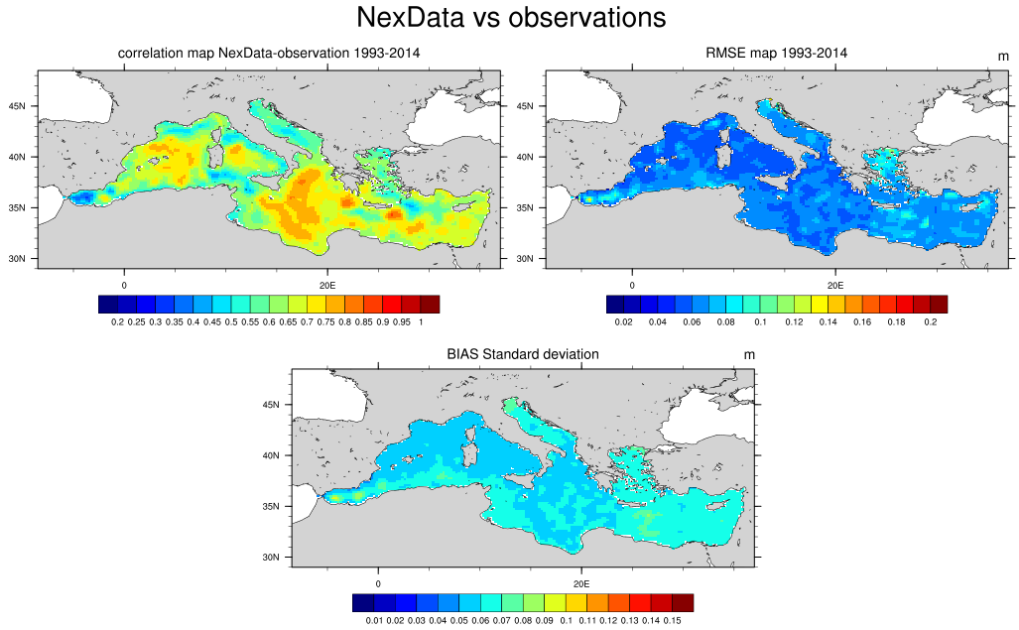

Figure 4.17: Correlation (upper left panel), RMSE (upper right panel) and BIAS STD (lower panel) for the SSH field of the NextData_RR reanalysis.

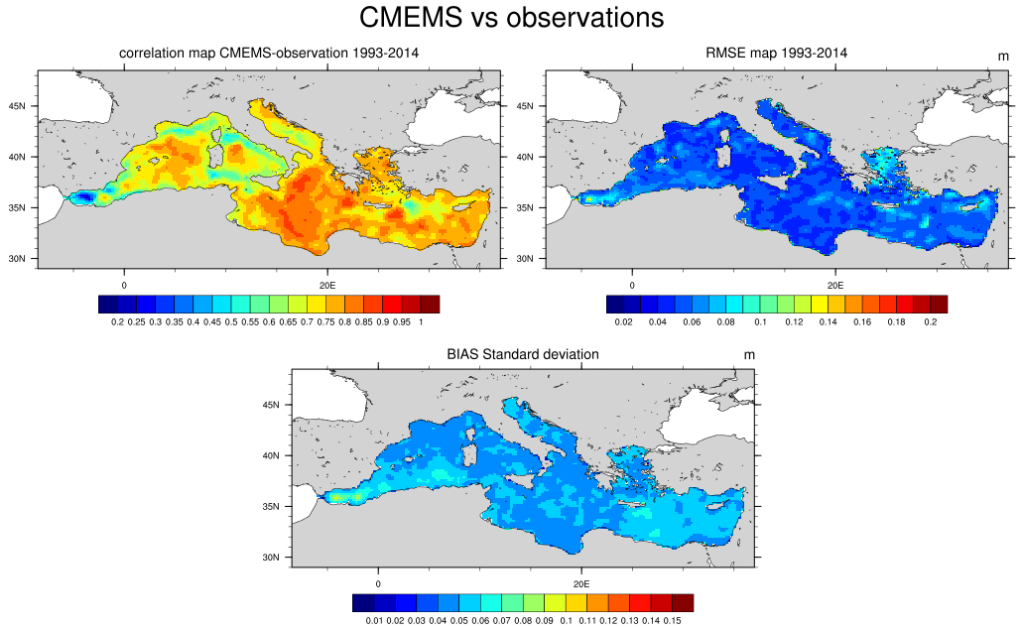

Figure 4.18: Correlation (upper left panel), RMSE (upper right panel) and BIAS STD (lower panel) for the SSH field of the CMEMS reanalysis.

In general, the correlations between observations and C-GLORS reanalysis appear to be the highest with lower values in the Alboran sea, in south Adriatic and south-east of Crete. The lowest correlation is given by the NextData Reanalysis, with very low values in the marginal Adriatic and Aegean Sea and in the Alboran Sea. CMEMS has a better correlation with respect of NextData, but shows a very low value in the Alboran Sea. The lowest RMSE is given by CMEMS reanalysis. Higher Values of RMSE reflects the lower correlation values in the Alboran Sea. C-GLORS shows the highest values of RMSE in the WMED, maybe due to the

low data resolution, and some high peaks in the EMED, in the Aegean Sea and in the Levantine Sea, south-east of Crete. The BIAS STD shows almost the same pattern for the three reanalysis with higher values in the Alboran and Levantine Sea. The problem of correcting satellite altimetry observations near the coasts are well known, and can account for low correlation and high RMSE near the coasts. Another critical point is the Alboran Sea, where a strong mesoscale activity occurs, and some signals may be not correctly catch by the satellite altimeter or not well reproduced by coarser resolution model, inducing higher values of RMSE and low correlation coefficients. After the writing of the thesis it was clear that correlation should have been de-biased and SLA used instead of SSH.

NIR index

The NIR index computed from all the reanalysis data is shown in figure 4.19 for the entire period available for observations, from 1993 to 2014. C-GLORS reanalysis

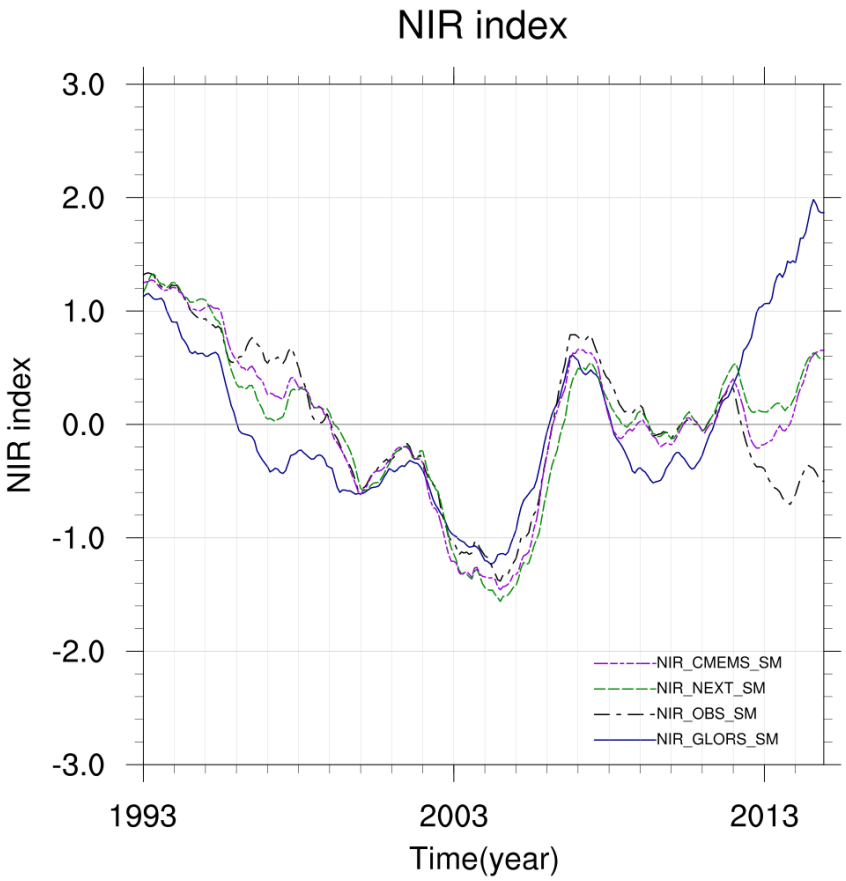

Figure 4.19: Smoothed NIR index from observed altimetric data and with the 3 reanalysis. Data are shown for the period 1993-2014.

anticipate the change of the sign of the NIR index in respect to observations and the other reanalysis, and tends to deviate mostly from the observed values.

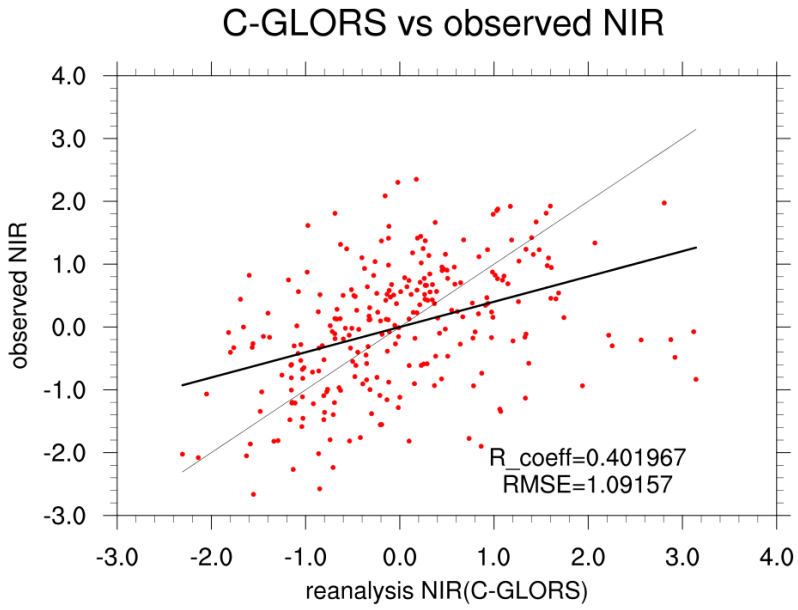

Figure 4.20: NIR index from observed altimetric data and reanalysis. Data are shown for the period 1993-2014.

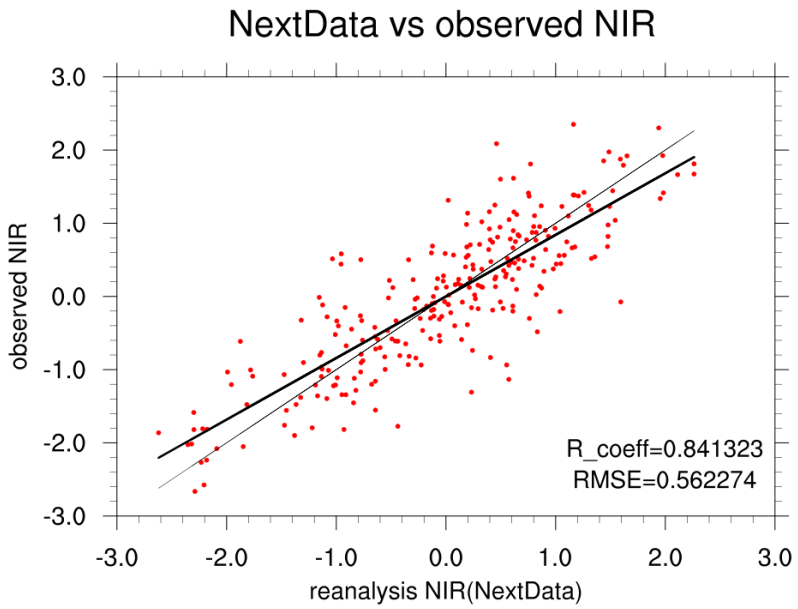

Figure 4.21: NIR index from observed altimetric data and reanalysis. Data are shown for the period 1993-2014.

NextData_RR and CMEMS NIR index agree very well with observations. For a better evaluation, correlation and RMSE between observed and reanalysis NIR indexes are computed (figure 4.20, 4.21 and 4.22). As it was expected, the C-GLORS reanalysis show the lower correlation (0.4) and the higher RMSE (1.09) probably due to the coarse resolution of the model. It is however to point out that excluding data of the last three year, the correlation grows to 0.62 and the RMSE become 0.87 (not shown). The CMEMS reanalysis shows the highest correlation and the lowest RMSE of 0.85 and 0.54 respectively. Similar values are reached by the NextData_RR reanalysis.

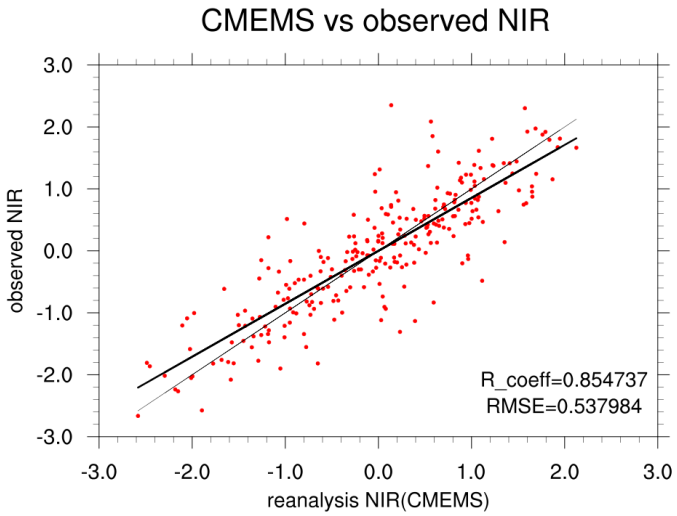

Figure 4.22: NIR index from observed altimetric data and reanalysis. Data are shown for the period 1993-2014.

As a last picture the NIR index computed from the simulations are shown in figure 4.23.

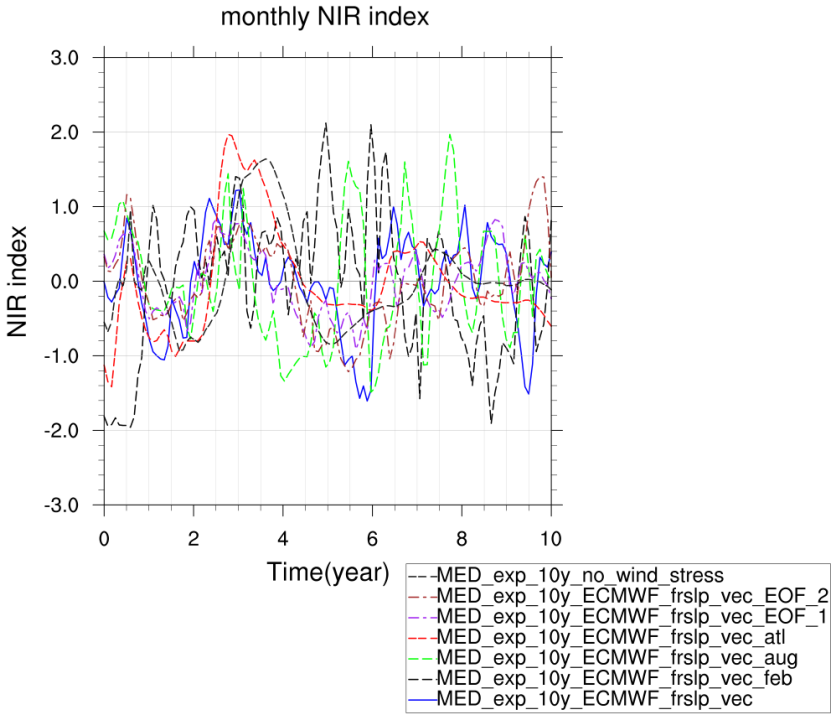

Figure 4.23: NIR index computed from the model simulations.

Chapter 5

Conclusions and outlooks

In this work the role of the wind in governing the Mediterranean circulation is assessed trough perpetual year simulations with the NEMO ocean numerical model implemented in the SURF model platform at an *eddy-permitting* horizontal resolution of $\frac{1}{8}^\circ \times \frac{1}{8}^\circ$ and 72 vertical levels. The NIR phenomenon, the reversal of the Northern Ionian current, is an important contribution to the decadal variability of the Mediterranean circulation and some insights are given on the role that the wind may have on this phenomenon. The wind data used as the surface boundary forcing are the ECMWF analysis and they were chosen through sensitivity simulations with different wind datasets.
Another set of sensitivity experiments investigated the physics and the numerical schemes of the model. The vertical physics and the specification of the closed lateral boundary conditions have an important role in the energetics of the circulation.

The central part of the thesis is dedicated to the study of the circulation response to the wind stress forcing. The wind forced run reproduces well the seasonal cycle and all of the peculiar features of the large-scale surface circulation that can be observed in the Mediterranean Sea. Two simulations were carried out using persisting February and August wind stress conditions. The double gyre structure of the Mediterranean Sea is reproduced by the simulations. The Winter circulation shows the maximum annual values of kinetic energy and is characterized by positive wind stress curl, producing a prevalent cyclonic circulation and gyres (GLG, RG, SETG), with intensified boundary currents both in WMED and EMED. The AIS and the Mid-Mediterranean jet are shifted southward and a cyclonic circulation occurs in the northern Ionian Sea. The Summer is characterized by opposite conditions, with negative wind stress curl that enhances the anti-cyclonic gyres (SG, MMG) and weakens the cyclonic gyres. The AIS is shifted northward, meandering in the Ionian Sea and occasionally generating anti-cyclonic eddies in the northern Ionian Sea. The position of the AIS is fundamental for the NIR phenomenon, and these experiments show the sensibility of the AIS to the wind stress forcing, connecting the NIR to the wind stress variability.
Two simulations are performed using an idealized wind rebuilt from the EOF analysis of the wind stress. These runs confirm the importance of the seasonal cycle in the WMED, while intra-seasonal wind stress variability may have a sensible role in the circulation of the EMED. Indeed, this intra-seasonal variability, when added to the wind stress seems to modify sensibly the CSWC path that enters in the Ionian

Sea, so influencing the circulation in that area.

The NIR index is a good diagnostic parameter that can be used to analyse the NIR phenomenon and the related circulation of the northern Ionian sea. Both Reanalysis models and observations agreed that between 1987 and 2007 the circulation reversed, setting the date of the reversal in 1997. The change of the sign of the NIR index indicates the reversal of the current. The analysis of the NIR index spectrum show the signature of the NIR at low frequency and important components with about 2 and 5 years periodicity. Nextadata_RR, that is the longer reanalysis, shows negative values of the index that are occurred in the past, but at higher frequencies and can not be directly connected to the NIR phenomenon.
The NIR computed for the model output shows high sensitivity to the wind forcing. The principal spectral components of the control run have 2 and 5 years of periodicity. This suggests that these components of the NIR index may be excited by the seasonal cycle of the wind stress, but further analysis are needed. A more focused study of the spectrum of the NIR is required and further studies are necessary to explore the periodicity and the causes of the NIR phenomenon.

Bibliography

[1] Arakawa, A., and Hsu, Y. Energy conserving and potential-enstrophy dissipating schemes for the shallow water equations. *Mon. Wea. Rev., 118 (10), 19601969* (1990).

[2] Artale, V., Astraldi, M., Buffoni, G., and Gasparini, G. Seasonal variability of the gyre-scale circulation in the northern tyrrhenian sea. *J. Gephys. Res., 99 (7), 14127-14137* (1994).

[3] Artegiani, A., Bregant, D., Paschini, E., Pinardi, N., and Raicich, N. The adriatic sea general circulation. part i: airsea interactions and water mass structure. *J. Phys. Oceanogr., 27, 1492-1514* (1997).

[4] Artegiani, A., Bregant, D., Paschini, E., Pinardi, N., and Raicich, N. The adriatic sea general circulation. part ii: baroclinic circulation structure. *J. Phys. Oceanogr., 27, 1515-1532* (1997).

[5] Artegiani, A., Paschini, E., Russo, A., Bregant, D., Raicich, F., and Pinardi, N. The adriatic sea general circulation. part ii: Baroclinic circulation structure. *J. Phys. Oceanogr. 27 (8), 1515-1532* (1993).

[6] Astraldi, M., Bianchi, C., and Morri, C. Climatic fluctuations, current variability and marine species distribution: a case study in the ligurian sea (north-west mediterranean). *Oceanologica Acta, 18 (2)* (1995).

[7] Ayoub, N., Traon, P. L., and Mei, P. D. A description of the mediterranean surface variable circulation from combined ers-1 and topex/poseidon altimetric data. *J. Mar. Sys. 18 (1-3), 3-40* (1998).

[8] Bleck, R., and Chassignet, E. Simulating the oceanic circulation with isopycnic-coordinate models. *The Oceans: Physical-Chemical Dynamics and Human Impact. 17-39* (1994).

[9] Bleck, R., Rooth, C., Hu, D., and Smith, L. T. Salinity-driven thermocline transients in a wind- and thermohaline-forced isopycnic coordinate model of the north atlantic. *J. Phys. Oceanogr., 22, 1486-1505* (1992).

[10] Blumberg, A., and Mellor, G. A description of a three-dimensional coastal ocean circulation model. *Three-Dimensional Coastal Ocean Models, Coastal Estuarine Science, N.S. Heaps, Ed., Amer. Geophys. Union, 1-16* (1987).

[11] Borzelli, G. L. E., Gacic, M., and Cardin, V. Eastern mediterranean transient and reversal of the ionian sea circulation. *Geophysical research letters 36 (15), L15 108* (2009).

[12] Bougeault, P., and Lacarrere, P. Parameterization of orographyinduced turbulence in a mesobeta-scale model. *Mon. Wea. Rev., 117, 18721890* (1989).

[13] Bryan, K. A numerical investigation of a non-linear model of wind driven ocean. *J. Atmos. Sci., 20, 594-606* (1963).

[14] Bryan, K. A numerical method for the study of the circulation of the world ocean. *J. Comput. Phys., 3, 347-376* (1969).

[15] Bryan, K., and Cox, M. A nonlinear model of an ocean driven by wind and differential heating: Parts i and ii. *Atmos. Sci., 25, 945-978* (1968).

[16] Bryan, K., and Cox, M. The circulation of the world ocean: A numerical study. part i, a homogeneous model. *J. Phys. Ocean., 2, 319-335* (1972).

[17] Carrier, G., and Robinson, A. On the theory of the wind driven ocean circulation. *J. fluid Mech., 12, 49-80* (1962).

[18] Castellari, S., Pinardi, N., and Leaman, K. Simulation of water mass formation process in the mediterranean sea: influence of the time frequency of the atmospheric forcing. *J. Gephys. Res., 18(1-3), 89-114* (1999).

[19] Cerchi, A., and Navarra, A. Sensitivity of the asian summer monsoon to the horizontal resolution: Differences between amip-type and coupled model experiments. *Clim. Dynam.* (2006).

[20] Charney, J. The gulf stream as an inertial boundary layer. *Proc. Nat. Acad. Sci., Wash., D. C., 41, 731-740* (1955).

[21] Cox, M. A primitive equation, 3-dimensional model of the ocean. *GFDL Ocean Group Tech. Rep. No. 1, 143 pp* (1984).

[22] Davies, H. A lateral boundary formulation for multi-level prediction models. *Quart. J. Roy. Meteor. Soc., 102, 405418* (1976).

[23] Dee, D., Uppala, S., Simmons, A., Berrisford, P., Poli, P., Andrae, S. K. U., Balmaseda, M., Bauer, G. B. P., Bechtold, P., Beljaars, A., van de Berg, L., Bidlot, J., Bormann, N., Delsol, C., Fuentes, R. D. M., Geer, A., Haimberger, L., Healy, S., Hersbach, H., Holm, E., Isaksen, L., Kallberg, P., Kohler, M., Matricardi, M., McNally, A., Monge-Sanz, B., Morcrette, J., Park, B.-K., Peubey, C., de Rosnay, P., Tavolato, C., Thepaut, J.-N., and Vitart, F. The era-interim reanalysis: configuration and performance of the data assimilation system. *Q.J.R. Meteorol. Soc., 137: 553597* (2011). doi:10.1002/qj.828.

[24] Demirov, E., and Pinardi, N. Simulation of the mediterranean sea circulation from 1979 to 1993: part i. the interannual variability. *J. Mar. Sys. 33-34 (0) 23-50* (2002).

[25] Engerdahl, H. Use of the flow relaxation scheme in a three-dimensional baroclinic ocean model with realistic topography. *Tellus, 47A, 365382* (1995).

[26] Flather, R. A storm surge prediction model for the northern bay of bengal with application to the cyclone disaster in april 1991. *J. Phys. Oceanogr., 24, 172190.* (1994).

[27] Fratianni, C., Simoncelli, S., Pinardi, N., Cherchi, A., Grandi, A., and Dobricic, S. Mediterranean rr 1955-2015 (version 1) [data set]. copernicus monitoring environment marine, 2016. Copernicus Monitoring Environment Marine Service (CMEMS). doi:http://dx.doi.org/10.25423/MEDSEA_REANALYSIS_PHY_006_009.

[28] Gacic, M. On the relationship between the decadal oscillations of the northern ionian sea and the salinity distributions in the eastern mediterranean. *J. Gephys. Res., 116 (c12)* (1993).

[29] Gleizon, P., DHie'res, G. C., and Renouard, D. Experimental study of the alboran sea gyres. *J. Oceanol. Acta, 19, 499511* (1996).

[30] Golnaraghi, M. Dynamical studies of the mersa-matruh gyre:intense meander and ring formation events. *Deep Sea Research, 40 (6), 12471268* (1993).

[31] Hecht, A. Abrupt changes in the characteristics of atlantic and levantine intermediate waters in the southeastern levantine basin. *Oceanol. Acta 15 (1), pp. 25-42* (1992).

[32] Hecht, A., Pinardi, N., and Robinson, A. Currents, water masses, eddies and jets in the mediterranean levantine basin. *J. Phys. Oceanogr., 8:1320-1353* (1992).

[33] Hellerman, S., and Rosenstein, M. Normal monthly wind stress over the world ocean with error estimates. *J. Phys. Oceanogr. 23, 1009-1039* (1992).

[34] Ingrosso, R. Analysis of climate indices in the mediterranean area: Ncpis and nir, 2015. Oceanografia Operativa e Tecnologie Informatiche per la sicurezza Marittima.

[35] Korres, G., Pinardi, N., and Lascaratos, A. The ocean response to low-frequency interannual atmospheric variability in the mediterranean sea. part i: Sensitivity experiments and energy analysis. *J. of climate 13 (4), 705-731* (2000).

[36] Large, W., and Yeager, G. Diurnal to decadal global forcing for ocean and sea-ice models: The data sets and flux climatologies. Tech. rep., NCAR, 2004.

[37] Larnicol, G., Ayoub, N., and Traon, P. L. Major changes in mediterranean sea level variability from 7 years of topex/poseidon and ers-1/2 data. *J. Mar. Sys. 33-34, 63-89* (2002).

[38] Lascaratos, A., and Nittis, K. A high-resolution three-dimensional numerical study of intermediate water formation in the levantine sea. *J. Geophys. Res., 103, 18497-18511* (1998).

[39] Lascaratos, A., Williams, R., and Tragou, E. A mixed-layer study of the formation of levantine intermediate water. *J. Geophys. Res., 98 (C8), 14739-14749* (1993).

[40] Leaman, K., and Shott, F. Hydrographic structure of the convection regime in the gulf of lions: winter 1987. *J. Phys. Oceanogr., 21, 575-598* (1991).

[41] Madec, G., and the NEMO team. *NEMO ocean engine.* 2012.

[42] Malanotte-Rizzoli, P., and Bergamasco, A. The circulation of the eastern mediterranean. part i. *Oceanologica acta, 12 (4)* (1989).

[43] Malanotte-Rizzoli, P., and Bergamasco, A. The wind and thermally driven circulation of the eastern mediterranean sea. part ii: the baroclinic case. *Dyn. Atm. Oceans 15, 179214* (1991).

[44] Mellor, G., and Yamada, T. Development of a turbulent closure model for geophysical fluid problems. *Rev. Geophys., 20, 851-875* (1982).

[45] Mesinger, F., and Arakawa, A. Numerical methods used in atmospheric models. *GARP Publication Series No 17* (1976).

[46] Millot, C. Mesoscale and seasonal variabilities of the circulation in the western mediterranean. *Dyn. Atm. Ocean, 15, 179214* (1991).

[47] Millot, C. Circulation in the western mediterranean sea. *J. Mar. Systems, 20, 423-442* (1999).

[48] Molcard, A. *Simulations de la circulation generale de la mer Mediterranee forcee par le vent, a l'aide d'un modele aux elements spectraux.* Ph.d. thesis, Universite de Poitiers, France, 1998.

[49] Molcard, A., Pinardi, N., Iskandarani, M., and Haidvogel, D. Wind driven general circulation of the mediterranean sea simulated with a spectral element ocean model. *Dyn. Atmos. Oceans 35 (2), 97-130* (2002).

[50] Morgan, G. On the the wind driven ocean circulation. *Tellus, 8, 301-320* (1956).

[51] Nittis, K., and Lascaratos, A. Diagnostic and prognostic numerical studies of liw formation. *J. Mar. Sys., 18, 179-195* (1998).

[52] Nittis, K., Pinardi, N., and Lascaratos, A. Characteristics of the summer 1987 flow field in the ionian sea. *J. Gephys. Res., 98 (6), 10171-10184* (1993).

[53] Ovchinikov, I., and Fedoseyev, A. The horizontal circulation of the water of the mediterranean sea during the summer and the winter seasons. *185-201* (1965).

[54] Pacanowski, R., and Philander, S. Parameterization of vertical mixing in numerical models of tropical oceans. *J. Phys. Oceanogr., 11 (11), 14431451* (1981).

[55] Paschini, E., Artegiani, A., and Pinardi, N. The mesoscale eddy field of the middle adriatic sea. *Deep Sea Research I, 40 (7), 1365-1377* (1993).

[56] Patera, A. A spectral element method for fluid dynamics - laminar flow in a channel expansion. *J. omput. Phys., 54, 468-488* (1984).

[57] Pickard, G. L., and Emery, W. J. *Descriptive Physical Oceanography.* 1982.

[58] Pinardi, N., Korres, G., Roussenov, V., and Stanev, E. Numerical simulation of the interannual variability of the mediteranean sea upper ocean circulation. *J. Geophys. Res., 24, 425-428* (1997).

[59] Pinardi, N., and Masetti, E. Variability of the large scale general circulation of the mediterranean sea from observations and modelling: a review. *Palaeogeography, Palaeoclimatology, Palaeoecology 158 (2000) 153173* (2000).

[60] Pinardi, N., and Navarra, A. Baroclinic wind adjustment processes in the mediterranean sea. *Deep Sea Res., Part II, 40, 1299-1326* (1993).

[61] Pinardi, N., Zavatarelli, M., Adani, M., Coppini, G., Fratianni, C., Oddo, P., Simoncelli, S., Tonani, M., Lyubartsev, V., Dobricic, S., and Bonaduce, A. Mediterranean sea large-scale low frequency ocean variability and water mass formation reates from 1987 to 2007: A retrospective analysis. *Progress in Oceanography* (2015).

[62] Poulain, P.-M., Menna, M., and Marri, E. Surface geostrophic circulation of the mediterranean sea derived from drifter and satellite altimeter data. *J. Phys. Oceanogr., 42, 973-989* (2012).

[63] Rhines, P. Geostrophic turbulence. *Annual Review of Fluid Mechanics, 11 (1), 401-441* (1979).

[64] Robinson, A. General circulation of the eastern mediterranean. *Earth-Science Reviews., 32 (4), 285-309* (1992).

[65] Robinson, A., Hecht, A., Pinardi, N., Bishop, Y., Leslie, W., Rosentroub, Z., Mariano, A., and Brenner, S. Small synoptic/mesoscale eddies: the energetic variability of the eastern levantine basin. *Nature, 327 (6118), 131-134* (1992).

[66] Roether, W., Manca, B., Klein, B., Bregant, D., Georgolpoulos, D., Beitzel, V., Kovacevic, V., and Lucchetta, A. Recent changes in eastern mediterranean deep waters. *Science, 271, 333-335* (1996).

[67] Roullet, G., and Madec, G. Salt conservation, free-surface and varying levels: a new formaltion for an ocean gcm. *J. Geophys. Res, 105(C10), 2392723942* (2000).

[68] Roussenov, V., Stanev, E., Artale, V., and Pinardi, N. A seasonal model of mediterranean sea general circulation. *J. Geophys. Res., 100, 13515-13538* (1995).

[69] Sarkysian, A. C. The calculation of stationary wind currents in an ocean. *Izv. Akad. Nauk SSSR, Ser. Geofiz., 1, 123-176* (1956).

[70] Simoncelli, S., Fratianni, C., Grandi, A., Drudi, M., Oddo, P., and Dobricic, S. Mediterranean sea physical reanalysis (medrea 1987-2015) (version 1), 2014. Copernicus Monitoring Environment Marine Service (CMEMS). doi:https://doi.org/10.25423/medsea_reanalysis_phys_006_004.

[71] Speich, S., Madec, G., and Crepon, M. A strait ouflow circulation process study: The case of the alboran sea. *J. Phys. Oceanogr., 26, 320340* (1996).

[72] Stommel, H. The westward intensification of wind-driven ocean currents. *Trans. Amer. geophys. Union, 29, 202-206* (1948).

[73] Stommel, H. Deep wintertime convection in the western mediterranean sea. *Studies in Phys. Oceanogr., 2, 207-218* (1972).

[74] Storto, A., and Masina, S. C-glorsv5: an improved multipurpose global ocean eddy-permitting physical reanalysis. *Earth Syst. Sci. Data, 8, 679-696* (2016). doi:10.5194/essd-8-679-2016.

[75] Tonani, M. *Studio della predicibilit della circolazione del Mar Mediterraneo.* Ph.d. thesis, Universita di Bologna, Italy, 2003.

[76] Trotta, F., Fenu, E., Pinardi, N., Bruciaferri, D., Giacomelli, L., Federcio, I., and Coppini, G. A structured and unstructured grid relocatable ocean platform for forecasting (surf). *Deep Sea Res. II, 133, 54-75* (2016).

[77] Tziperman, A., and Malanotte-Rizzoli, A. The climatological seasonal circulation of the mediterranean sea. *J. Mar. Res., 49, 411434* (1991).

[78] Veronis, G. Wind-driven ocean circulation-part 2. numerical solutions of the nonlinear problem. *Deep-Sea Research, 13, 31-55* (1966).

[79] Zavatarelli, M., and Mellor, G. A numerical study of the mediterranean sea circulation. *J. Phys. Oceanogr., in press* (1995).

Acknowledgements

When I asked Prof. Nadia Pinardi for the possibility to start an oceanographic thesis, she immediately filled my spirit with her passion and enthusiasm. Her knowledge and experience allowed me to give my best in this work.
A special thanks goes to Francesco Trotta, that helped me doing my first steps in the world of the numerical ocean modelling, and Simona Masina that supported me in the time spent at CMCC.
Recalling all the time spent in the SINCEM laboratory, in Ravenna, a lot of people come to my mind. I would like to thank Luca, Simona, Claudia, Augusto, Sara and all the people I met in the lab. They helped me in different situations and I am glad to have met people like them in my path.
I would like to thank all the PHD students met at INGV and CMCC. Without them the time spent at CMCC would not be the same thing.
A big thank goes to my best friends, Cecca, Giro and Zazza. In their way they have always supported me. Thank you.
Finally, a great thanks goes to my girlfriend, Elisa, that sustained me through all the difficulties and to my family, my mum Monica, my sister Alice and my grandparents Aride and Giuliana that are the best supporters I ever had.